EX LIBRIS
UNIVERSITATIS
ALBERTENSIS

The Bruce Peel
Special Collections
Library

Digitized by the Internet Archive
in 2025 with funding from
University of Alberta Library

https://archive.org/details/0162017993195

University of Alberta

Library Release Form

Name of Author: Zhengke Chen

Title of Thesis: The Influence of Welding Processes on Pitting Corrosion and Stress Corrosion Cracking in 304 Austenitic Stainless Steel

Degree: Master of Science

Year this Degree Granted: 2003

Permission is hereby granted to the University of Alberta Library to reproduce single copies of this thesis and to lend or sell such copies for private, scholarly or scientific research purposes only.

The author reserves all other publication and other rights in association with the copyright in the thesis, and except as herein before provided, neither the thesis nor any substantial portion thereof may be printed or otherwise reproduced in any material form whatever without the author's prior written permission.

University of Alberta

The Influence of Welding Processes on Pitting Corrosion and Stress Corrosion Cracking in 304 Austenitic Stainless Steel

by

Zhengke Chen

A thesis submitted to the Faculty of Graduate Studies and Research in partial fulfillment of the requirements for the degree of Master of Science

in

Materials Engineering

Department of Chemical and Materials Engineering

Edmonton, Alberta
Fall 2003

University of Alberta

Faculty of Graduate Studies and Research

The undersigned certify that they have read, and recommended to the Faculty of Graduate Studies and Research for acceptance, a thesis entitled The Influence of Welding Processes on Pitting Corrosion and Stress Corrosion Cracking in 304 Austenitic Stainless Steel submitted by Zhengke Chen in partial fulfillment of the requirement for the degree of Master of Science in Materials Engineering.

Abstract

The effect of two welding processes, laser welding (LW) and gas tungsten arc welding (GTAW), on the corrosion behavior of 304 stainless steel is investigated. Various electrochemical methods such as Scanning reference electrode technique (SRET), potentiodynamic scans and capacitance measurements were used to determine the localized corrosion susceptibility, initiation and propagation of pitting and SCC in the weld zones. The experimental results reveal that SCC and pitting susceptibility depend on the microstructure of the stainless steel material. The weld metal (WM) of LW has better corrosion resistance than that of GTAW. The behavior of SCC and pitting corrosion directly correlated to the stability of the altered passive film by the welding processes.

Acknowledgements

I wish to express my deep gratitude to Dr. J.L. Luo , Dr. B.M. Patchett and Dr. Z.H. Xu , for their generous support, encouragement, discussion and suggestions.

I am grateful to my research group members, Dr. Lu, Dr. J.G.Yu and Mr. Y.M.Zeng for their discussion and suggestions.

Table of Content

Chapter 1 Introduction 1

Chapter 2 Literature review 5

2.1 Metallurgy for welding 5

2.1.1 Classification of zones during the welding 7

2.1.2 Residual stresses and stress concentrations..... 8

2.2 Effect of welding metallurgy for austenitic stainless steels on corrosion behavior 11

2.2.1 Sensitization in HAZ 12

2.2.2 Knifeline attack 13

2.2.3 Susceptible microstructure in weld metal..... 13

2.3 Electronic properties of passive films of stainless steel..... 13

2.4 Stress corrosion cracking (SCC)..... 15

2.4.1 Metallurgical effects..... 16

2.4.2 Electrochemical effects..... 16

2.4.3 Mechanisms of stress corrosion cracking..... 18

2.5 SCC in austenitic stainless steel 22

2.5.1 Effect of composition..... 23

2.5.2 Effect of stress..... 23

2.5.3 Effect of surface finish..... 23

2.5.4 Effect of microstructure..... 24

2.5.5 Effect of sensitization..... 24

2.5.6 Effect of temperature..... 24

2.5.7 Effect of the presence of oxygen..... 24

2.5.8 Effect of pH 25

2.5.9 Effect of potential..... 25

2.6 Electrochemical methods to study the initiation and propagation of pitting and SCC 26

2.6.1 Scanning reference electrode technique..... 26
2.6.2 Measurements of polarization curves..... 28
2.6.3 Mott-Shottky method..... 28
2.7 Methods for studying SCC 29
2.7.1 Constant deformation tests..... 29
2.7.2 Sustained load tests..... 30
2.7.3 Slow strain-rate testing..... 30
2.8 Unsolved problems..... 30

Chapter 3 Experimental Procedure..... 36
3.1 Material and specimen preparation 36
3.2 SRET 37
3.3 Potentiodynamic polarization test 37
3.4 Capacitance measurement and Mott–Schottky analysis 38
3.5 Specimens used for SCC tests..... 39
3.6 SCC Tests 40
3.7 Crack size measurements..... 41

Chapter 4 Effect of welding processes on initiation and propagation of pitting and SCC..... 43
4.1 In-Situ observation of pitting initiation and propagation with SRET 43
4.2 Pitting potential..... 47
4.3 SCC initiation and propagation 49
4.4 SCC initiation kinetics..... 54
4.5 SCC propagation kinetics..... 71
4.6 Discussion 79
4.7 Summary..... 81

Chapter 5 Mechanism analysis..... 82

5.1 Microstructure analysis..... 82
5.2 The Effect of the welding process on the conductivity of passive films..... 86
5.3 Effect of tensile stress on stability of the passive film..... 89
5.4 Relationship between properties of passive film and resistance to SCC and pitting corrosion 93
5.5 Summary..... 94

Chapter 6 Summaries and Recommendations..... 96
6.1 Main conclusions..... 96
6.2 Recommendations for future work 97

List of Tables

Table 4-1 Constants in equation 4-2.....70
Table 4-2 Crack growth rates in different zones..... 78
Table 4-3 Aspect crack growth rate in different zones.....78

List of Figures

Figure 2-1 Thermal cycles in weld ones 5

Figure2-2 (a)Metallurgical designations in heat affected zones; (b)Different microstructural zones across a low alloy steel weldment..... 6

Figure 2-3 Relationships between temperature, stress σ and strainεduring welding..... 9

Figure 2-4 Distribution of stress across a butt weld..... 10

Figure 2-5 Schematic potentiokinetic polarization curve showing zones of susceptibility to stress corrosion cracking..... 17

Figure 2-6 schematic drawing of a local corrosion cell showing (a) Current paths in the electrolyte flowing from the anode to the cathode, and (b) Equipotential lines in the electrolyte..... 27

Figure 3-1 Shape of tensile specimens used in static loading tests: dimension in mm..... 38

Figure 3-2 Tapered LW specimens with longitudinal weld: dimension in mm..... 39

Figure 3-3 Tapered GTAW specimens with longitudinal weld : dimension in mm..... 40

Figure 3-4 Setup for the electrochemical measurements of stressed specimens... 41

Figure 4-1 (a) SRET two-dimensional images for LW 304 stainless steel in $5x10^{-4}$ M $FeCl_3$+$1x10^{-4}$ M $NaNO_3$ solution (b) No pits were observed on base metal for laser welded 304 stainless steel (c) SRET two-dimensional images for GTAW 304 stainless steel in $5x10^{-4}$ M $FeCl_3$+$1x10^{-4}$ M $NaNO_3$ solution (pit initiation time: 1 hr, scanning area: 5 x 9 mm^2) (d) pits observed on weld metal for laser welded 304 stainless steel after 3 hrs (Applied potential: 0.38 V (vs. SCE))..... 45

Figure 4-2 (a) SRET three-dimensional images for LW 304 stainless steel in $5x10^{-4}$ M $FeCl_3$ + $1x10^{-4}$ M $NaNO_3$ solution(pit initiation time: 2 hr, scanning area: $5x9mm^2$) (b)Four pits observed in base metal for laser welded 304 stainless steel after 3 hrs (c) SRET three-dimensional images for GTAW 304 stainless steel in $5x10^{-4}$ M $FeCl_3$ + $1x10^{-4}$ M $NaNO_3$ solution((pit initiation time: 0 hr, scanning area:$5x9mm^2$) (d)Pits observed in weld metal for laser welded 304 stainless steel after 3 hrs (Applied potential: 0.9 V (vs. SCE))..... 46

Figure 4-3 (a) Pits observed in the WM after GTAW (b) Pits observed in the BM after LW..... 47

Figure 4-4: Potentiodynamic polarization curves for weld metal, base metal and HAZ of GTA welded 304 stainless steel in 5×10^{-4} M $FeCl_3$ + 1×10^{-4} M $NaNO_3$ solution..... 48

Figure 4-5 Dependence of crack densities on the stress level and test duration (a-b) LW (c-d) GTAW (e) BM..... 53

Figure 4-6 Dependence of average surface crack length on the stress level and test duration (a-b) LW (c-d) GTAW (e) BM..... 57

Figure 4-7 Crack morphology in various zones 59

Figure 4-8 Factography of SCC (a-b) HAZ of LW (c-d) HAZ of GTAW..... 61

Figure 4-9 Fractography of SCC (a-b) in the WM of LW (c-d) in the WM for GTAW..... 63

Figure 4-10 Fractography of SCC in the BM..... 64

Figure 4-11 Correlation between crack densities and test duration (a-b) LW (c-d) GTAW (e) BM..... 68

Figure 4-12 Dependence of crack initiating rates on applied stress level (a) GTAW (b) LW..... 69

Figure 4-13 Crack initiation lifetime curves 70

Figure 4-14 Correlation between the maximum surface crack length and test duration (a-b) LW (c-d) GTAW (e) BM 75

Figure 4-15 Correlation between the crack depth and test duration (a) Maximum crack depth a_{max} in BM and WM after LW (b) Maximum crack depth a_{max} in BM and WM after GTAW..... 76
Figure 5-1 (a) The morphology and distribution of delta-ferrite in the WM after LW (b) The morphology and distribution of delta-ferrite in the WM after GTAW 83
Figure 5-2 WRC-1992 Constitution diagram for stainless steel weld metal 85
Figure 5-3 Potentiodynamic scan in cathodic direction with a rate of 50 mV s^{-1} after pre-passivated for 2 hours at 0.5 V (vs. SCE) in the borate solution of pH 9.2 87
Figure 5-4 Depth composition profiles obtained by AES for the passive films formed on 304 stainless steel at 0.8 V vs. SCE 87
Figure 5-5 (a) The Mott–Schottky type plots in a borate solution of pH 9.2 (b) Comparison of doping densities in different zones 88
Figure 5-6 (a) The Mott–Schottky type plots of WM of GTAW specimens in a borate solution of pH 9.2 (b) Comparison of doping densities (Various stress levels in the WM) 91
Fig 5-7 (a) The Mott–Schottky type plots of the BM in the borate solution of pH 9.2 (b) Comparison of doping densities (Various stress levels in the BM)..... 92

List of Symbols

Symbol	Meaning
ε_r	strain
A	experimental constant
a_{max}	maximum crack depth
C	capacitance
C_m	average crack length
C_{max}	maximum crack length
d_{SC}	thickness of the space charge layer
Dc	crack density
E	potential
E_f	fermi level
E_{FB}	flatband potential
Epp	pitting potential
i	current density
K	solution conductivity
k	Boltzmann constant
n	experimental constant
N_A	concentrations of acceptor
N_D	concentrations of donor
q	elementary charge
T	absolute temperature
t	time
Z''	imaginary resistance
δ	delta
ε	dielectric constant
ε_0	vacuum permittivity
σ	stress
φ	phase angle

ω	angle frequency
α	experimental constant
β	experimental constant

List of Abbreviation

BM	base metal
GTAW	gas tungsten arc welding
HAZ	heat affected zone
HIC	hydrogen induced cracking
LW	laser welding
SCC	stress corrosion cracking
SCE	saturated calomel electrode
SRET	scanning reference electrode technique
WM	weld metal

Chapter 1 Introduction

Welded structures of austenitic stainless steels such as pressure vessels and line pipes are common in many industries including petroleum, chemical and nuclear plants. These steels have excellent resistance to uniform corrosion, ease of fabrication, weldability, and an optimum combination of strength and toughness producing high flaw tolerance. However, they can suffer from susceptibility to localized corrosive attacks such as pitting corrosion, intergranular corrosion and stress corrosion cracking (SCC).[1,2] Especially in chloride ion-containing solutions, austenitic stainless steels are sensitive to local attack and passive film breakdown. Welding usually aggravates this situation because of the metallurgical alteration and residual stresses introduced during the welding process [3]. Although the microstructure of welded areas is rather complicated, in line with the microstructural features, a welded area is roughly divided into three distinct zones, WM (weld metal), HAZ (heat-affected zone) and BM (base metal). Normally, the WM of austenitic stainless steel has a cast structure with the presence of 2-10% δ-ferrite in the austenite matrix. A small amount of δ-ferrite is necessary to avoid the problem of hot cracking during weld solidification[4]. Some studies[5] show that selective dissolution occurs in δ-ferrite when the steel contacts certain corrosive environments, leading to corrosion-related failure. The exact role of δ-ferrite, especially how much of it affects corrosion behavior is not completely understood.

Besides the corrosion-sensitive microstructure, residual stresses produced in welding processes will affect localized corrosion behavior. The influence of tensile stress on the susceptibility of corrosion has already been shown by numerous studies[6,7,8]. It has been reported that when the applied tensile stress exceeds the yield strength of the material, both the physical and electrochemical behavior of stainless steels may change significantly, and results in remarkable increase in corrosion susceptibility. The residual

stresses are inevitable during the welding process. However, the mechanism for stress-promoted corrosion is not well understood and is worthy of study. Furthermore, the sensitized microstructures in the WM and HAZ[9,10] , and residual tensile stresses induced by welding,[11,12] make the steel susceptible to SCC[1,13]. Although the mechanistic aspects as well as contributing factors in the SCC have been extensively reported, the process of SCC, especially SCC initiation, is still not well understood [14,15,16,17,18] and failures of welded austenitic stainless steel components are still very common.[1] Up to now, experimental investigations on the SCC of welded austenitic steels are usually carried out in the transverse direction.[15,16,17,18,19,20] Few work has been done on the effect of welding orientation on the SCC behavior[21]. However, in butt-welded pipelines the maximum tensile stress (the hoop stress) acts in the longitudinal direction. Information about the SCC behavior of welded stainless steels in the longitudinal orientation is of practical importance in the SCC prediction for butt-welded pipelines.

The objective of this work is to investigate the effects of metallurgical changes introduced by different welding processes, as well as stress, on the localized corrosion of 304 stainless steel. Particularly an effort was made to understand the effect of δ-ferrite on the resistance to localized corrosion. In addition, the SCC initiation and propagation behavior of a welded 304 stainless steel were investigated for the specimens with a weld in the longitudinal orientation.

In order to present this work clearly and systematically, this dissertation is divided into six chapters. Chapter 2 is a comprehensive review of the welding metallurgy in 304 stainless steel, corrosion related problems concerning the welding procedure and electrochemical methods to study the corrosion behavior.

The preparation of electrode, solution, the establishment of experiments and the main approach methods employed in this work are introduced in Chapter 3.

Chapter 4 presents the pitting corrosion and SCC behavior observed in the weldment after two different welding processes. The results contain the dependence of the pitting susceptibility on the welding processes, the reliance of SCC initiation and propagation rates on the welding processes.

The mechanism of the distinct corrosion behavior after two welding processes is illustrated in Chapter 5, where the relationship among the welding processes, microstructure and stability of passive films is clarified.

In the final chapter, the main conclusions are summarized as well as some general recommendation for future work.

References

1 K. Nishimoto, and K. Ogawa: Weld. Intern., Vol. 13(11), 1999, p845

2 T. G. Gooch: Weld. J., Vol.75(5), 1996, p135

3 D.A. Jones, Principles and prevention of corrosion, Ed. Prentice Hall, 1992, p308

4 CASTI publishing Inc. and American Welding Society (AWS), The metals blue book. Filler metals, 1998, p88

5 M.G. Pujar, R.k. Dayal, T.p.S.Gill, S.N. Malhotra, Role of delta-ferrite in the dissolution of passive films on the austenitic stainless steel weld metals. Journal of Materials Science Letters, Vol. 18, 1999, p823

6 Y. Sano, N. Mukai and K. Okasaki Nucl. Instrum. Meth. Phys. Res. B, Vol. 121, 1997, p432

7 P. Peyre, X. Scherpereel and L. Berthe Mater. Sci. Eng. A, Vol.280, 2000, p294

8 A. Chambreuil-Paret and T. Magnin Metall. Mater. Trans. A, Vol. 30, 1999, p1327

9 Z. Fang, Y. Wu and R. Zhu: Corrosion, Vol.50(3), 1994, p171

10 T. Angeliu, M. Andresen, P. L. Hall, E. Sutliff, J. A. and S. Sitzman: Corrosion' 2000, 2000, p186

11 K. Komai: Intern. J. Fatigue, Vol.20(2), 1998, p145

12 M. J. Diehl and R. W. Jr. Messler: Weld. J., Vol.74(4), 1995, p109

13 Z. Fang, Y. Wu and R. Zhu: Corrosion, Vol.50(3), 1994, p171

14 G. Sui and E. A. Charles: Corr. Sci., Vol.38(5), 1996, p687

15 T. Kobayashi, D. A. Shockey and R. L. Jones: Corrosion, Vol. 47(7), 1991, p528

16 T. Haruna, R. Toyota and T. Shibata: Corr. Sci., Vol.39(10-11), 1997, p1873

17 T. Haruna and T. Shibata: Corrosion, Vol.50(10), 1994, p785

18 A. Miyasaka and T. Kanamaru: Corrosion, Vol.52(8), 1996, p592

19 W. Yang, J. Congleton, O. Kohneh-Chari and P. Sajdl: Corr. Sci., Vol.33(5), 1992, p735

20 Y. Watanabe and T. Kondo: Corrosion, Vol.56(12), 2000, p1250

21 I. Krecek and S. Chomutov: Zvaranie, Vol.49(11-12), 2000, p99

Chapter 2 Literature Review

2.1 Metallurgy for welding

A characteristic weld contains several beads and has a weld width that increases towards the outer surface of the component. The microstructure developed during welding will vary across the weldment as well as within the beads. During welding, very rapid heating cycles, high peak temperature and relatively rapid cooling rates to ambient temperature are all involved. The rapid heat input and high energy density causes very different thermal effects from conventional heat treatments. A typical thermal cycle for an arc welding process is shown in Figure 2-1[1].

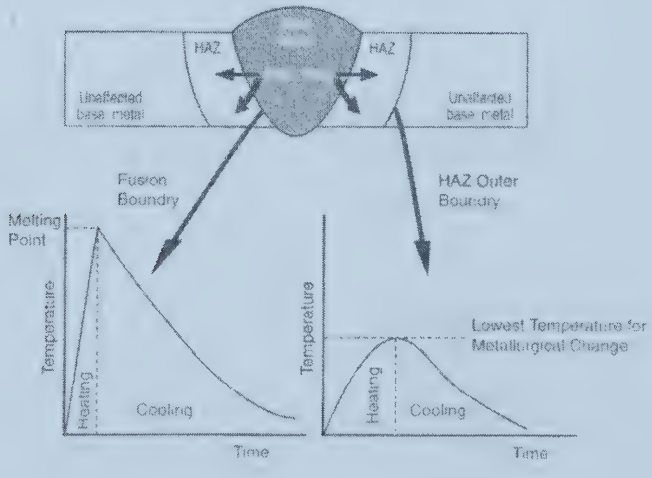

Figure 2-1 – Thermal cycles in weld zones[1]

The type of microstructure developed is essentially controlled by the heat cycle and the characteristics of the material, i.e. chemical composition, microstructure before welding (base material), etc. A subsequent post weld heat treatment reduces residual

stresses introduced during welding as well as influences the mechanical properties of the weldment constituents. Depending on the type of microstructure, the weldment can be divided into a number of different zones. For a low alloy steel weldment, starting from the centre of the weld, the following zones can be distinguished across the weldment: weld metal(WM), partially melted zone and melted unmixed zone, coarse grained heat affected zone(HAZ), fine grained HAZ, intercritical HAZ and base metal(BM) (see Figure 2-2).

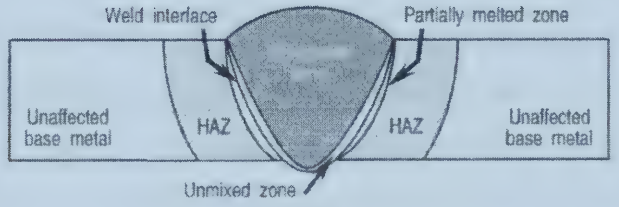

(a)

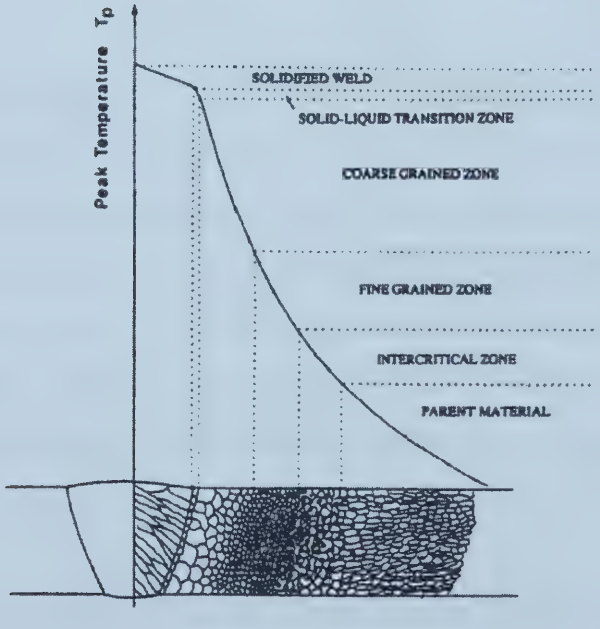

(b)

Figure 2-2 (a) - Metallurgical designations in heat affected zones; (b) Different microstructural zones across a low alloy steel weldment[2]

2.1.1 Classification of zones during the welding[1]:

a. Weld metal (WM)

It is also called composite zone due to the chemistry of the filler metal differing from the base metal and the WM contains some melted base metal.

b. Partially melted zone and melted unmixed zone

Partially melted zone is formed due to the heating rates. Because of short time available, segregation of alloy elements or impurities in the base metal will not be even out by diffusion. This can lead to local region in the base metal right next to the fusion line where localized melting can occur. Melted unmixed zone is a very thin region of melted base in the weld metal right next to the fusion line which, although 100% molten, is not stirred into the bulk of the molten pool during welding, due to viscous effects during mixing.

c. Heat affected zone(HAZ)

Within HAZ a couple of zones were formed due to the combination of heating rate, peak temperature and cooling rate. When the peak temperature is below a critical temperature for the metal being welded, the subcritical HAZ occur. This could be the recrystallization temperature in a work-hardened metal, the solvus temperature for a precipitation-hardened alloy or the allotropic phase change temperature for a transformation hardening alloy. Above the critical temperature, the grain size increases as the temperature increases.

HAZ consist of fine grained HAZ, coarse grained HAZ and intercritical HAZ. Fine grained HAZ exists when an allotropic phase change decreases the average grain size in comparison with the grain size in the subcritical region. Coarse grained HAZ

occurs at high temperatures when all phase changes are completed. Grain size tends to increase up to the fusion temperature. Intercritical HAZ occurs where the temperature is between the temperature where austenite starts to form and where all ferrite and carbide is gone and only fine grain austenite remains.

2.1.2 Residual stresses and stress concentrations

Tensile residual stresses in weldments may cause SCC and hydrogen-induced cracking(HIC)[3]. Dring heat up, melting, freezing, and cool-down stress can be expressed as functions of temperature and strain as shown in the weld Figure 2-3[2]. In parts that are physically constrained in their required positions near one another, initial heating induces thermal expansion and compressive stresses beginning at 1. As temperature rises at 2, the metal will release compressive stresses back to zero during softening and creeping. Temperature increases and thermal expansion continue through 3 and 4 in the softened and melted metal, respectively. After melting, temperature falls and the weld metal freezes at 5. Freezing causes a large volume contraction from molten to solid weld metal and additional thermal shrinkage during subsequent cooling. In constrained base metal parts, these contractions cause large, ambient-temperature, residual, tensile stress, σ_r, and strain, ε_r, at 6. Distortions may result from shrinkage in weldments that are not rigidly constrained.

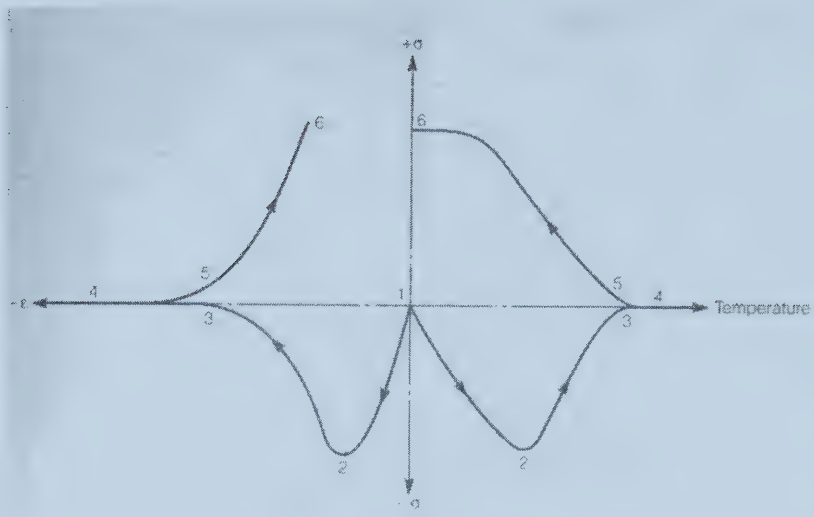

Figure 2-3- Relationships between temperature, stress σ and strainεduring welding[2].

The distribution of stress across a completed butt weld is shown in Fig. 2-4. Within the weld metal, high tensile stresses, σ_x, σ_y, are apparent, while significant compressive stresses in the surrounding base metal. Plastic deformation in the base metal near the molten zone can be observed when thermal expansion and softening during heating is sufficient. Subsequent freezing and thermal contraction generate tensile stresses up to yield in and near the frozen weld metal. Compressive stresses in the surrounding base metal are necessary to resolve the total stress state to zero. Other weld geometries result in still more complex stress fields around the welds. It is important to appreciate that welding produces residual tensile stresses, which can cause SCC and HIC in planes transverse and longitudinal to the weldment.

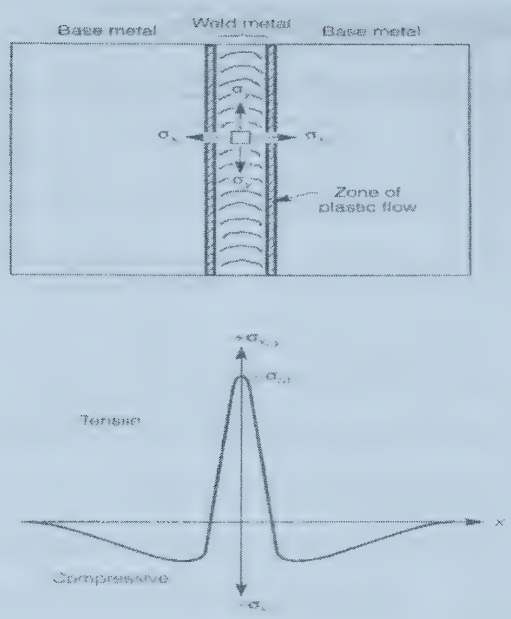

Figure 2-4 – Distribution of stress across a butt weld [2]

Welding produces a geometric discontinuity in the cross section, which concentrates any applied or residual stress. As a result, corrosion fatigue cracking (CFC), as well as SCC and HIC failures, often originate at the toe of a weld. Furthermore, Welding quality is very much dependent on the skill of the welder and quality of the materials and equipment in use. As a result, defects occur rather frequently. Such defects further aggravate stress concentrations, which lead to mechanical and environmentally induced cracking.

High residual stresses and stress concentrations make weldments the weak point for all forms of environmentally induced cracking. Thus, any combination of stress, alloy and environment that would cause cracking in the base metal will often cause cracking preferentially at welds.

2.2 Effect of welding metallurgy for austenitic stainless steels on corrosion behavior

Gas tungsten arc welding (GTAW) and Laser welding (LW) process are widely used welding techniques for stainless steels. These two welding techniques usually cause fundamental microstructure alteration around weldments. Few studies have been carried out on the effect of the two welding processes on the corrosion behavior.

GTAW is used extensively for welding stainless steel, aluminum, magnesium, copper and reactive materials. The melting temperature necessary to weld materials in the GTAW is obtained by maintaining an arc between a tungsten alloy electrode and the work piece. An inert gas sustains the arc and protects the molten metal from atmosphere contamination. The inert gas is normally argon, helium, or a mixture of helium and argon. GTAW offers some advantages. It produces high-quality, low-distortion welds, free of the spatter associated with other methods. It can be used with or without filler metal and with a range of power supplies. Additionally, it can weld almost all metals, including dissimilar ones and gives precision control of welding heat. The application of LW on stainless steel was investigated because of its importance in the power plant and chemical industry. A moving high-density coherent optional energy source called a laser is used as the source of heat. It can be focused to a small spot, leading to high energy densities due to the coherent nature of the laser beam. The availability of high-power continuous-wave carbon dioxide (CO_2) and neodymium-doped yttrium aluminum garnet (Nd:YAG) lasers overcomes the limitation of current welding. Numerous experiments have shown that the laser permits precision weld joints. It offers many advantages over conventional arc welding. Focused laser light provide high energy densities. It can be used at room atmosphere. Difficult-to-weld materials (Ti, Quartz) can be joined. No electrode or filler metal is required. Narrow welds can be obtained. Welds with little or no contamination can be produced. HAZ adjacent to the WM is very narrow. [4]

Austenitic stainless steels are austenite at ambient temperatures because their carbon, Ni content (at least 8%) and Mn content are sufficient to stabilize austenite at ambient temperature without a transformation to martensite in normal circumstances. They contain 16-25%Cr and 7-20%Ni. Carbon content is important in the control of sensitization as discussed below. High carbon content in stainless steel promotes the formation of chromium carbides on grain boundaries, which reduces corrosion resistance of grain boundaries. Therefore, stabilized Ti and Nb can be added to modify the properties of resistance to sensitization.[5] Mo is usually added to improve pitting corrosion resistance. The factors that can influence the type and degree of preferential attack depend on[6]

1) Composition and structure of base and weld metal
2) Metallurgical changes in the parent metal due to welding
3) Welding process and procedure
4) Size of material welded
5) Type of the environment

The following corrosion problems are often found on welded Austenitic stainless steels.

2.2.1 Sensitization in HAZ [7]

The heat-affected zone adjacent to the weld may be preferentially attacked as a result of metallurgical changes caused by the heating cycles[7]. Sensitization by the precipitation of chromium carbide in HAZ is a major concern in welding austenitic grades. It is also known as weld decay. If corrosion resistance at ambient temperature is the only criterion, use low carbon grades. If extreme conditions are not involved, most grades specifying 0.08%C maximum have <0.06% in practice, which is low enough to avoid carbide precipitation in welding procedures using a reasonable heat input. If high temperatures are involved in service, even low carbon grades are inadequate, and stabilized grades must be used, for example, Types 321 and 347.

2.2.2. Knifeline attack (KLA) [8]

It is a specific intergranular corrosion phenomenon of stabilized austenitic stainless steels. The attacked areas have been found to contain precipitated chromium carbides; the stabilizing elements niobium (columbium) or titanium fail to tie up the carbon in the alloy. KLA is similar to weld decay in that they both result from intergranular corrosion and both are associated with welding. The two major differences are:

1. KLA occurs in presumably stabilized steels;
2. KLA occurs in a very narrow band in the parent metal immediately adjacent to the weld, whereas weld decay develops at a greater distance from the weld.

2.2.3 Susceptible microstructure in the WM

Weld metal may corrode more or less than the parent metal owing to differences in composition or metallurgical condition. The main problem has always been solidification cracking, primarily from sulphur segregation due to its low solubility in austenite. The solution to the problem is to ensure a few percentage of ferrite in the ambient temperature weld metal to prevent solidification cracking. Reasons proposed for this effect are that the solidification occurs as primary ferrite with FA-type, forming very irregular grain-boundaries structure with a lower energy, which is not readily wetted by the low-melting liquids such as sulfides/phosphides. Consequently, it is very resistant to the nucleation and propagation of cracks. [9] However, some studies indicate that δ ferrite is likely to dissolve preferentially.[10,11,12]

2.3 Electronic properties of passive films of stainless steel

It is well known that localized corrosion arises from the breakdown of passive films. Study of the passive film after welding is critical to understand the corrosion

behavior. Passive films on iron and steels are semiconductors. Because dissolution, film formation, and breakdown all involve the movement of electrons and ions from the metal surface through the passive film or from the solution into the film, electronic properties are a significant aspect of the nature of the passive film. Moreover, electron transfer reactions that occur on surfaces with passive films depend strongly on the electronic properties of such films. Therefore the semiconducting character of the passive films formed on stainless steel was recognized to have great influence on the initiation of localized corrosion.

Pioneer research has dealt with the films formed on iron. The work of Wagner involves the analysis of the stoichiometric character of these films[13]. Stimming established[14] that the electronic structure of an anodically grown film (in pH 8.4 borate buffer solution) on iron could be described in terms of a duplex film with a Fe_3O_4 inner layer and a highly doped n-type Fe_2O_3 outer layer. Gerischer elaborated on this model by giving the band structure of a graded material[15], going from $Fe_{2.67}O_4$ (i.e. Fe_2O_3) at the surface to Fe_3O_4 at the metal contact. Stimming also published work on the influence of localized states in photoelectrochemical measurements[16] and that of deep donor levels on capacity measurements[17]. Bohni and Schmuki[18] examined the photoelectrochemical response of stainless steel in sulfate solutions and concluded that the anodic films were highly defective and that they possessed a high number of localized states. The non-stoichiometric compositions or the local structural inhomogeneities were cited as the possible causes of these states. A correlation between the distribution of the localized states and the nucleation sites for pitting was discussed.

In the case of stainless steels, analytical studies reveal a duplex structure for the films which consists of an inner region composed of a few atomic layers of chromium oxide (p-type semiconductor) in contact with the metallic substrate, and an outer region

of iron oxides and hydroxides (n-type semiconductor) at the film electrolyte interface [19,20,21,22]. However, the exact electronic structure of these films formed on the weld metal has not been fully established as well as the correlation between this structure and their stability. The study of the properties of the very thin passive films formed on welded stainless steels is still of fundamental and practical importance in corrosion science.

Furthermore, numerous studies[23,24,25] have shown that, above the apparent yield strength, a mechanical stress induces major changes in the physical and electrochemical behavior of stainless steels (SS), which may increase the corrosion susceptibility of these materials. Among these studies, it has been demonstrated, by using Auger electron spectroscopy, that the composition of passive films formed on type 302 and 316 steels [26,27] depends on the nature (compression or tension) and level of stresses. Regarding SCC, it has been shown [28] that the mechanical modifications induced in surface by a preliminary cold working decreases the time for cracks initiation and the time to failure of a type 304 SS immersed in a solution of $MgCl_2$ boiling at 154 °C. Therefore, it appears that a very low level of stress may lead, in certain electromechanical conditions, to a decrease of the ability of passive films to protect the substrate against localized corrosion.

2.4 Stress corrosion cracking (SCC)

SCC is the brittle failure caused by constant tensile stress of an alloy exposed to a corrosive environment. SCC depends on three conditions present at the same time:

1) A critical environment

2) A susceptible alloy

3) Tensile stress

Although the three factors are not usually present simultaneously, time and service conditions may combine together and result in unexpected failures. Boiling and evaporation can concentrate the critical solutes in very dilute and otherwise nonaggresive

solutions. Residual tensile stresses can result from uneven thermal expansion and contraction after welding. Tensile stresses even below yielding strength are sufficient to cause SCC and may result from bolting and fastening parts that fit together imperfectly.

2.4.1 Metallurgical effects

SCC may be either transgranular or intergranular. Transgranular failures are less common than the intergranular ones, but both may exist in the same system or even in the same failed part, depending on conditions. The crack usually follows general macroscopic path that is always normal to the tensile component of stress. In transgranular failures, the cracks propagate across the grains usually in specific crystal planes, usually having low indices such as {100}, {110} [29]. The cracks follow grain boundaries in the intergranular mode. The intergranular failure mode suggests some inhomogeneity at the grain boundaries. For example, segregation of sulfur and phosphorous at grain boundaries is the probable cause of intergranular SCC of low alloy steels [30]. And in fact, intergranular stress corrosion cracking may be the result of stress-assisted intergranular corrosion since most alloys showing such failures also show at least weak evidence of intergranular corrosion without stress.[31]

Because halves of failed specimens often exactly match one another, whether intergranular or transgranular, it indicates that cracking is primarily by brittle fracture, with little electrochemical dissolution or corrosion during the fracture process. However, anodic dissolution does play a significant role.

2.4.2 Electrochemical effects

Electrochemical potential has an essential influence on stress corrosion cracking. The potentiodynamic anodic polarization curve for a typical active-passive corrosion-resistant alloy is shown in fig. 2-5. Zone 1 and 2 are those in which

transgranular SCC growth is most likely to occur. For classical SCC, the passive film is a prerequisite for SCC, but the two zones of susceptibility appear at the potential ranges where the passive film is less stable. In zone 1, SCC and pitting are situated in overlapping potential ranges. The common example of zone-1 SCC is austenitic stainless steel in hot $MgCl_2$ solutions. SCC occurs in a narrow potential range, with pitting present at slightly noble potentials and passivity. Although stress corrosion cracks may initiate at pits due to stress intensification, they are not necessarily a prerequisite for SCC, even in zone 1. However, in some instances, potent solutions or oxides that are unstable on the exposed surface can accumulate within pits and initiate cracks.

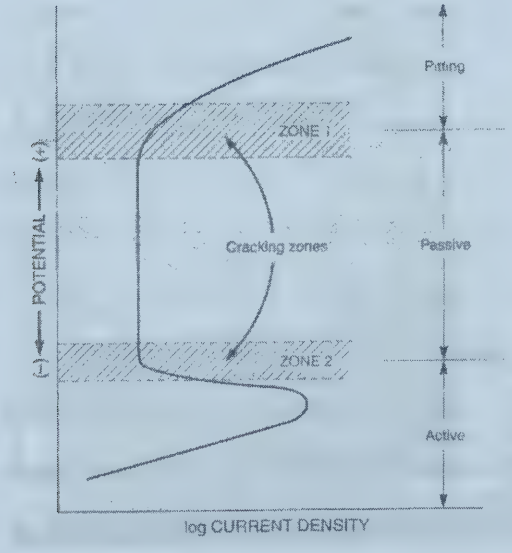

Figure 2-5 – Schematic potentiokinetic polarization curve showing zones of susceptibility to stress corrosion cracking [32]

In Fig. 2-5 zone 2, the material is in transition from active corrosion to passive film formation such that the simultaneous conditions for film formation on the crack walls and corrosion at the crack tip are met. SCC occurs where the passive film is

relatively weak at active potentials barely adequate to form the film. The example is carbon steel in hot carbonate/bicarbonate solutions. SCC has also been observed in the active region for carbon steel in strong caustic solutions. Film formation and growth is possible even in active potential ranges because anodic currents decrease with time. Also because the potential of the active-peak current tends to become more active with time, a potential in the active potential range during short –term potentiodynamic polarization may actually be in zone 2 during longer-term SCC exposures.[33]

2.4.3 Mechanisms of stress corrosion cracking

Tremendous experimental investigation and theoretical analysis have been devoted to SCC. Numerous mechanisms have been proposed, and the main ones that have received attention are presented in this section.

a. Active path dissolution [34]

This process involves accelerated corrosion along a path of higher than normal corrosion susceptibility, with the bulk of the material typically being passive. The most common active path is the grain boundary, where segregation of impurity elements can make it marginally more difficult for passivation to occur. For example, when an austenitic stainless steel has been sensitized by precipitation of chromium carbide along the grain boundary, the local chromium concentration at the grain boundary will be reduced, and this region will be slightly less easily passivated. Consequently, a form of crevice corrosion can occur, whereby the grain boundary corrodes, with the specimen surface and the crack walls remaining passive. This process can occur in the absence of stress, giving rise to intergranular corrosion that is uniformly distributed over the specimen. The effect of the applied stress is probably mainly to open up the cracks, thereby allowing easier diffusion of corrosion products away from the crack tip and allowing the crack tip to corrode faster. Active path corrosion processes are inherently

limited by the rate of corrosion of the metal at the crack tip.

b. Film rupture [35]

Film rupture or slip-step dissolution was one of the first proposed stress corrosion cracking mechanisms and still receives considerable support. It is assumed that the stress acts to open the crack and rupture the protective film at an emerging slip band. Cracks grow by anodic dissolution of the unfilmed surface at the rupture site. Most investigators now agree that film rupture is essential to initiate cracking, but considerable controversy persists as to how a stress expected to grow on the active slip plane, where deformation would cause continual film rupture, contrary to the experimental fact that cracks grow on planes of the type {100}{110}.

Parkins [36] has convincingly demonstrated correlation between crack growth velocity and anodic current density on straining electrode surfaces. A crack growing by electrochemical dissolution at an unfilmed crack tip should leave a relatively smooth, featureless surface. As a result, film rupture and dissolution are accepted as viable mechanisms of intergranualr SCC in some systems, contrary to the crystallographic cleavage (transgranular SCC) features typically present on the fracture surfaces such as topographic features on opposing brittle fracture surfaces often match exactly, indicating further that the surfaces were formed by brittle mechanical cleavage-like processes with very little surface dissolution.

c. Hydrogen embrittlement [37]

Hydrogen dissolves in all metals to a moderate extent. It is a very small atom, and fits in between the metal atoms in the crystals of the metal. Consequently it can diffuse much more rapidly than larger atoms. For example, the diffusion coefficient for hydrogen in ferritic steel at room temperature is similar to the diffusion coefficient for salt in water. Hydrogen tends to be attracted to regions of high triaxial tensile stress

where the metal structure is dilated. Thus, it is drawn to the regions ahead of cracks or notches that are under stress. The dissolved hydrogen then assists in the fracture of the metal, possibly by making cleavage easier or possibly by assisting in the development of intense local plastic deformation. These effects lead to embrittlement of the metal; cracking may be either inter- or transgranular. The brittle nature of stress corrosion cracking can only be accounted for hydrogen induced cracking, which has brittle cleavage-like features very similar to those of SCC. The result is singular crack with little branching. In some instances, many cathodic formation of hydrogen and subsequent measured entry into the metal lattice has stopped growing stress corrosion cracks.

The bcc (body-centred cubic) crystal structure of ferritic iron has relatively small holes between the metal atoms, but the channels between these holes are relatively wide. Consequently, hydrogen has a relatively low solubility in ferritic iron, but a relatively high diffusion coefficient. In contrast the holes in the fcc (face-centred cubic) austenite lattice are larger, but the channels between them are smaller, so materials such as austenitic stainless steel have a higher hydrogen solubility and a lower diffusion coefficient. Consequently, it usually takes very much longer (years rather than days) for austenitic materials to become embrittled by hydrogen diffusing in from the surface than it does for ferritic materials, and austenitic alloys are often regarded as immune from the effects of hydrogen.

d. Adsorption induced cleavage

It is based on the hypothesis that metal bonds at the cracks tip are weakened by adsorption of critical anions from solution. Uhlig [38] originally proposed that specific aggressive dissolved species adsorb at "mobile defect sites" weakening the cohesive bonds between adjacent atoms at the crack tip. This model is frequently referred to stress absorption cracking. It is similar to the effect postulated for hydrogen during hydrogen

induced cracking and for liquid metal atoms during liquid metal embrittlement. Also, the environmental cracking of polymers by specific organic solvents has been thought to occur by such an adsorption mechanism.

e. Atomic surface mobility

The mechanism predicts that stress corrosion cracking should be prevalent at temperatures below 0.5 times the melting point of the metal, T_m, and in the presence of low melting surface compounds, when surface mobility is maximized in preference to bulk diffusion in the metal crystal. It is observed that many forms of environmentally induced cracking grow by the capture of surface vacancies at the crack tip and counter–current surface diffusion of atoms away from the crack tip[39,40]. The effect of critical environments to cause stress corrosion cracking is explained by low melting compounds which enhance surface mobility. However, it is then debatable as to whether a driving force is available for surface vacancy formation and diffusion. Parkins[41] points out that although carbon steel cracks in nitrates which form low melting compounds with iron, it also cracks in the presence of high melting point Fe_3O_4. Oriani[42] shows that the flow of surface atoms should be toward the crack tip rather than away from tip in the presence of a stress field. Galvele[43] argues that surface atoms exist in the absence of a stress field.

f. Film-induced cleavage [44]

FIC postulates the dealloying or vacancy injection induce brittle fracture. A crack growing in the film may propagate further into the underlying metal if it reaches sufficient velocity at the film/metal interface. The film-induced cleavage mechanism has been proposed to explain discontinuous transgranular crack growth and high transgranular crack growth rates. Anodic dissolution and corrosion are not necessary to propagate cracks but only to form the required brittle surface film. Thus, a relatively low

anodic dissolution rate forms a brittle surface film, and fast-growing crack in the film may penetrate for some distance into the ductile substrate metal before its growth is arrested. The surface film must reform at the crack tip surface before a new burst of brittle crack growth is possible. Thus, a low anodic current at a strained surface can foster rapid, discontinuous, brittle cracking, according to the FIC mechanism.

g. Corrosion tunnel model [45]

It is assumed that a fine array of small corrosion tunnels forms at emerging slip steps. These tunnels grow in diameter and length until the stress in the remaining ligaments causes ductile deformation and fracture. The crack thus propagates by alternating tunnel growth and ductile fracture. Cracks propagating by this mechanism should result in grooved fracture surfaces with evidence of microvoid coalescence on the peaks.

2.5 SCC in austenitic stainless steel

SCC of austenitic stainless steel in hot chlorides is perhaps the most widely known and intensely studied example of SCC. AS a result, failures occur frequently in apparently benign environments containing only a few ppm chlorides or less. Susceptibility increases with aggressive conditions lead to intergranular cracking in service conditions. Truman[46] has defined the boundaries of temperature and chloride content causing SCC of austenitic stainless steel; some of his results appear by pitting and crevice corrosion. Other halides will also produce SCC in conditions similar to those for chloride. SCC in austenitic stainless steels is sometimes transgranular. The scanning electron fractograph indicates a generally cleavage-like character illustrating the brittle nature of SCC in this system, in which the crack path clearly crosses grain boundaries and passes through the grains. SCC is concerned with the nucleation and propagation of cracks in stressed metals induced by the environment. In order to understand the

mechanism of cracking in any particular metal-environment system, it is necessary to determine the electrochemical reactions that take place at the crack tip.

2.5.1 Effect of composition

Many alloying additions appear to be detrimental to chloride SCC, but there are also those that can be categorized as beneficial. Nickel, cadmium, zinc, silicon, beryllium, and copper are supposed to be beneficial. The beneficial effect of nickel relates only to austenitic stainless steel. However, Boron, aluminum[47,48,49,50,51,52], and cobalt appear to be detrimental in small quantities but beneficial in larger amounts; tin and manganese have no effect in certain range and beneficial or detrimental effects in other ranges[30,35]; carbon appears to increase corrosion susceptibility with small carbon additions in the range of 0.01 to 0.06, and above 0.1% the susceptibility decreases.[53] For chromium in the range of 5-12%, it tends to inhibit corrosion, and accelerates corrosion between 12 and 25%, then inhibit above this value. [53]

2.5.2 Effect of stress

Generally speaking, decreasing the applied stress increases time to failure. The only sure way to control stresses is by stress-relief annealing the fully assembled structure. This is often an option for small components. For larger ones, partial stress-relief by heating to 400 to 600 °C is useful. These benefits should be weighted against potential sensitization. The introduction of compressive surface stresses such as, shot peening has been shown to increase resistance to SCC[54].

2.5.3 Effect of surface finish

Surface finish may induce stress variation due to local work hardening, martensitic transformation, residual stresses, and embedded material from abrasives and machining equipment, or provide stress raisers such as deep grooves or notches. To

compare the performance of SCC resistance, surface finishes should be nominally identical.[32]

2.5.4 Effect of microstructure

The presence of delta ferrite usually increases the resistance of hot cracking during welding. The exact effect of delta ferrite on corrosion resistance has not been agreed. Some studies show that delta ferrite in austenitic stainless steel improves the resistance to chloride SCC[55]. It is considered that the presence of delta ferrite interfere with the propagation of cracks across the austenite matrix. Other studies suggested that delta-ferrite becomes selectively corroded in certain corrosive environments[56,57].

2.5.5 Effect of sensitization

Intergranular SCC of sensitized austenitic stainless steel has been a recurring and extensive problem in the controlling-water piping of boiling-water nuclear power plants[58], whereas nonsensitized materials usually exhibit predominantly transgranular cracking in environment such as boiling magnesium chloride.

2.5.6 Effect of temperature

Generally, chloride SCC does not occur in nonsensitized austenitic stainless steel at temperature below about 60 °C in near-neutral chloride solutions[59]. But in severe conditions, the minimum temperature could be lowered to 50 °C.

2.5.7 Effect of the presence of oxygen

The presence of oxygen is not necessary to cause SCC in concentrated chloride solutions boiling at atmospheric pressure as their oxygen contents should approach zero. However, the introduction of oxygen into the solutions at room temperature always accelerates SCC [60].

2.5.8 Effect of pH

It has been determined that the pH of the solution at the crack tip in type 304 undergoing SCC in magnesium chloride is between 1.2 and 2.0 [61]. This suggests acidity may be occurring by the hydrolysis of metal ions. There is evidence that the solution within the microvolume of the crack becomes acidified, probably by hydrolysis reactions similar to those that occur in pits[62]. During free corrosion with no imposed polarizing potentials, there must be cathodic reduction to compensate for the anodic dissolution reactions within the crack. For austenitic stainless steel exposed to hot $MgCl_2$ solutions, where hydrolysis and acidification are known to be strong, evolution of hydrogen from cracks indicates cathodic reduction of H on the crack was the presence of hydrogen in the crack and the brittle cleavage characteristics of transgranular cracks suggest that hydrogen causes SCC. Increase in the pH of bulk solution could improve the situation[63].

2.5.9 Effect of potential

The electrode potential has a major effect on susceptibility to chloride SCC. Detailed studies exhibit that increasing the potential in the noble direction facilitates cracking, whereas decreasing the potential in the active direction reduces susceptibility until a cathodic protection potential is attained[64].

Temperature and solution composition (including pH and dissolved oxidizers, aggressive ions, and inhibitors or passivators) can modify the anodic polarization behavior to permit SCC, as well as control corrosion potential in a critical region. Hence, one cannot predict susceptibility to SCC solely form the anodic polarization curve[65].

Generally, crack growth is proportional to anodic dissolution currents at straining electrode surfaces. However, some systems, particularly those with fast transgranular cracking, have crack growth rates higher than can be accounted for by simple electrochemical dissolution. Thus, electrochemical anodic dissolution probably

initiates mechanical fracture processes, accounting for both anodic current proportionality and brittle crack topography[66].

2.6 Electrochemical methods to study the initiation and propagation of pitting and SCC

2.6.1 Scanning reference electrode technique (SRET)

SRET is an in situ technique used to locate the anodic and cathodic sites and study the electrochemical processes during localized corrosion without altering the processes taking place, changing the local environment over the corrosion site, or influencing the rate of corrosion. Evans and Agar[67] calculated the current from the measured equipotential lines associated with the flow of current during the corrosion of zinc. SRET was used to measure the potential variation in the solution. Jaenicke and Bonhoeffer[68,69], Copson[70], and Rozenfeld[71] have measured the potential distribution around galvanic couples and calculated the corrosion rates and the surface current density distributions. Measurements of potential distribution during corrosion of bismuth-cadmium and zinc-aluminum alloys were also studied[72]. More recent measurements of couples of iron and copper have been conducted by Hildebrand and Schwenk[73].

During localized corrosion, the anodic oxidation of the metal and cathodic reduction of species from the solution usually takes place at well-separated areas. The flow of electrons within the metallic phase does not involve significant ohmic potential differences because of the high conductivity of the metal. The flow of current within the aqueous phase, carried by ions, is associated with small potential changes between the anodic and cathodic areas.

Fig. 2-6 shows a schematic of the flow of current in the electrolyte from a localized anodic to the surrounding cathodic areas and equipotentials set up around the localized electrode. By scanning a "passive" reference probe with a fine capillary tip parallel and in close proximity to the metal surface, the potential distribution in the liquid can be measured. The potential changes are most rapid over the localized electrode; a potential maximum or minimum is observed over its center.

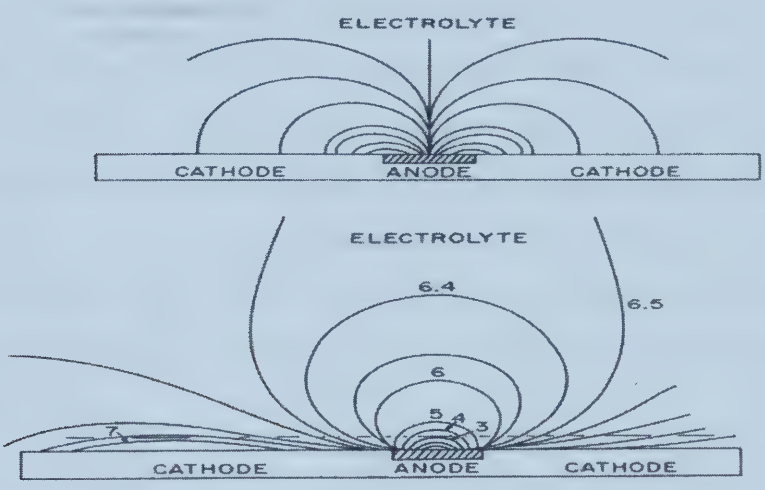

Figure 2-6 schematic drawing of a local corrosion cell showing (a) Current paths in the electrolyte flowing from the anode to the cathode, and (b) Equipotential lines in the electrolyte

The distribution of potential and current can be theoretically determined from Laplace equation

$$\nabla^2 E=0 \tag{2-1}$$

and Ohm's law

$$i = -K\nabla E \tag{2-2}$$

Where E, i, and K are the potential, current density and solution conductivity. It should be emphasized here that the SRET does not directly measure the potential variations of the metal surface, but responds to current variations in solution. These currents are more dependent on the polarization characteristics of the metal surface than the surface

potential.

2.6.2 Measurements of polarization curves

Potentiodynamic anodic polarization has been used to supply information on the susceptibility of the materials to different types of corrosion. Those curves allow us to identify the range of critical potentials, where cracking usually develops- active passive transient- which quantatively indicates the SCC growing risk. Polarization curves can be measured using controlled current methods and controlled potential methods. Because current is a single function of potential, the controlled potential procedures are preferred. Among the controlled potential procedures, the potentiodynamic method of changing the potential continuously at a constant rate is the most commonly used method. Generally speaking, the anodic current increases rapidly after the potential reaches the critical pitting potential E_{pp} (also called breakdown potential), above which the current will quickly increase.

2.6.3 Mott-Shottky method

The most commonly used method to study the electronic properties is Mott-Schottky analysis. The Mott-Schottky relation describes the potential dependence of the space charge capacity of a semiconductor electrode under depletion condition. Assuming that the solid state properties of the passive film determine its capacitance behavior and the Mott-Schottky relation is applicable, information on the conductivity type (n or p type) and on the donor or acceptor concentration and distribution can be obtained. According to the Mott-Schottky theory [74, 75], the space charge-charge capacitance of a semiconductor(C) is given by the following equations:

$$C^{-2} = \frac{2}{q\varepsilon\varepsilon_0 N_A}(E - E_{FB} - \frac{kT}{q}) \quad \text{for n-type semiconductor} \qquad (2\text{-}3)$$

$$C^{-2} = \frac{-2}{q\varepsilon\varepsilon_0 N_A}(E - E_{FB} - \frac{kT}{q}) \quad \text{for p-type semiconductor} \qquad (2\text{-}4)$$

where ε_0 is the vacuum permittivity, ε the dielectric constant of the specimen, q the elementary charge , k the Boltzmann constant , T the absolute temperature, N_A and N_D are the concentrations of acceptor and donor, respectively, E_{FB} the flatband potential. kT/q can be negligible as it is only about 25 mV at room temperature. The quantity E_{FB} is related to Fermi level of the semiconductor by the relationship: [76]

$$E_f = - |e| E_{FB} \qquad (2\text{-}5)$$

In a plot of $1/C^2$ vs. E, n-type semiconductors have straight line section with a positive slope while a p-type semiconductor has a negative slope. The intersection at $1/C^2=0$ gives the flatband potential E_{FB}. The thickness of the space charge layer is given approximately by the Debye length in the semiconducting film:

$$d_{SC} = \left[\frac{\varepsilon\varepsilon_0 kT}{q^2 N_D}\right]^{1/2} \qquad (2\text{-}6)$$

for a n-type material.

2.7 Methods for studying SCC

2.7.1 Constant deformation tests

Much information can be derived from time-to-failure of various constant deformation specimens.

1) U-bend specimen: It is quite convenient experimentally and forms one of the most severe smooth specimen tests for SCC.

   Disadvantage: The stress distribution within the specimen is not well known, and the stress conditions are difficult to duplicate from specimen to specimen.

Advantage: Frequently used to evaluate qualitatively the resistance of various alloys to various solution conditions.

2) C-ring specimen: Variable stresses both above and below yield strength may be controlled by the amount of applied deformation.

3) Bent Beam: When stressed below the yield strength, the bent-beam specimen permits precise calculation of the maximum stress in the outer fibers of the bent beam.

4) Constant-deformation specimen: It gives the greatest control of applied stress and permits easy stress measurement and analysis.

2.7.2 Sustained load tests

By adding a spring to C-ring specimen, a constant load is applied to the specimen during the test. Upon initiation of a crack, the net cross-sectional area decreases and the stress increases under sustained load as the crack grows, driving an ordinary smooth tensile specimen to total failure, eliminating the growth portion of cracking from the measured time to failure.

2.7.3 Slow strain-rate testing

It has the particular advantage of speed, while retaining correlation with long-term constant-displacement tests. But some experiments are necessary to determine the critical strain rate for SCC testing. At a critical strain rate, a minimum ductility is observed characteristic of SCC. When above or below the critical strain rate, ordinary cup-and-cone ductile rupture forms. The slow strain-rate test is more severe than constant-displacement or constant-load tests. Hence, an alloy showing SCC in this test would not necessarily fail in service.

2.8 Unsolved problems

Localized corrosion such as SCC and pitting corrosion have received a

significant amount of investigation, but little work has been done on how different welding processes affect the microstructure, and thereafter the electronic properties of passive films over welds and their correlation with localized corrosion. Therefore, these issues are main focus of this thesis.

References

1 Barry M. Patchett, John E. Bringas, The Metal Blue Book, American Welding Society, 1998, p17

2 Storesund, J. and Tu, S.-T., Geometrical effects on creep in cross-weld specimens, Int. J. Pres. Ves. & Piping, Vol. 62, 1995, p179

3 K.Easterling, Introduction to the Physical Metallurgy of Welding, Butterworths, London, 1983, p35

4 Welding, Brazing and Soldering, ASM Handbook,Vol.6, 1990, p190

5 Erich Folkhard, Welding Metallurgy of Stainless Steels, 1984

6 Brautigam, F.C. Corrosion, Vol.31, 1975, p101

7 Cowan, J.R. and Tedmon, Jr., C.S., Advances in Corrosion Science and Technology, Vol.3, 1973, p293

8 D.A. Jones, Principles and Prevention of Corrosion, 1992, p294

9 Welding , brazing, and soldering, ASM Handbook, Vol. 6, 1990, p464

10 Shaikh, H., Khatak, H. S., Seshadri, S. K, Gnanamoorthy, J. B., and Rodriguez, P., Effect of Ferrite Transformation on the Tensile and Stress Corrosion Properties of Type 316 L Stainless Steel Weld Metal Thermally Aged at 873 K, Metallurgical and Materials Transactions A, 26A(7), 1995, p1859

11 Krishnan, K. N. and Rao, K. P., Effect of Microstructure on Stress Corrosion Cracking Behaviour of Austenitic Stainless Steel Weld Metals, Materials Science and Engineering, A, Vol.142(1), 1991, p79

12 Raghunatha, R. B., Prasad, R., K. and Iyer, K. J. L., Effect of Chemical Composition and Ferrite Content on Room Temperature SCC Behavior of Austenitic Weld Metals, Corrosion, Vol.49(3), 1993, p248

13 C. Wagner, Ber. Bunsen-Ges. Phys. Chem., Vol. 77, 1973, p1090

14 U. Stimming, J.W. Schultze, Ber. Bunsen-Ges. Phys. Chem., Vol.8, 1976 , p129

15 H. Gerischer, Corros. Sci., Vol. 26, 1986, p191

16 U. Stimming, Langmuir, Vol. 3, 1987, p423

17 U. Stimming, M.H. Dean, J. Electroanal. Chem., Vol.228, 1987, p135

18 H. Bo¨ hni, P. Schmuki, J. Electrochem. Soc., Vol. 139, 1992., p1908

19 G. Lorang, M. Da Cunha Belo, A.M.P. Simo˜ es, M.G.S, Ferreira, J. Electrochem. Soc., Vol.141, 1994, p3347

20 N.E. Hakiki, S. Boudin, B. Rondot, M. Da Cunha Belo, Corros. Sci., Vol.37 1995, p1809

21 N.E. Hakiki, M. Da Cunha Belo, J. Electrochem. Soc., Vol. 143, 1996 , p3088

22 N.E. Hakiki, M. Da Cunha Belo, A.M.P. Simo˜ es, M.G.S. Ferreira, J. Electrochem. Soc., Vol.145, 1998, p3821

23 Y. Sano, N. Mukai and K. Okasaki Nucl. Instrum. Meth. Phys. Res. B, Vol. 121, 1997, p432

24 P. Peyre, X. Scherpereel and L. Berthe Mater. Sci. Eng. A, Vol. 280, 2000, p294

25 A. Chambreuil-Paret and T. Magnin Metall. Mater. Trans. A, Vol.30, 1999, p1327

26 F. Navaï J. Mater. Sci., Vol.30,1995, p1166

27 F. Navaï and O. Debbouz J. Mater. Sci., Vol.34, 1999, p1073

28 P. Muraleedharan, H. Khatak, J. Gnanamoorthy and P. Rodriguez Metall. Trans. A, Vol.16, 1985, p285

29 R.Liu, N.Narita, C. Alstetter, H. Birnbaum, and E.N. Pugh, Metall. Trans. A, Vol. 11A, 1984, p1563

30 M.J. Danielson, C.Oster and R.H.Jones, Corros. Sci., Vol.32(1), 1991, p1

31 R.N.Parkins, Environmental induced Cracking of Metals, R.P.Gangloff and M.B.Ives, eds., NACE, Houston, 1990, p1

32 R.W. Staehle, Stress corrosion cracking and hydrogen embrittlement of iron base alloys, NACE-5, NACE, Houston, 1977, p193

33 R.H.Jones, Stress corrosion cracking, ASM, 1992, p14

34 R.H.Jones, Stress corrosion cracking, ASM, 1992, p32

35 Champion, F.A., Symp. Internal Stresses in Metals and Alloys, Institute of Metals, 1948, p468

36 R.N. Parkins . Br. Corrosion J., Vol. 14, 1979, p5

37 B.D.Criag, Metals Handbook, , Corrosion, 9th ed., ASM International, Metals Park, Vol.13, 1987, p164

38 H.H. Uhlig, Physical Metallurgy of Stress Corrosion Fracture, T.N.Rhodin,Ed., Interscience, 1959, p1

39 J.R. Galvele, Corrosion Science, Vol.27, 1987, p1

40 G.S. Duffo and J.R. Galvele, Environment-Induced Cracking of Metals, R.P. Gangloff and M.B. Ives, eds., NACE, Houston, 1990, p261

41 R.N. Parkins, Environment-Induced Cracking of Metals, R.P. Gangloff and M.B. Ives, eds., NACE, Houston, 1990, p1

42 R.A. Oriani, Environment-Induced Cracking of Metals, R.P.Gangloff and M.B. Ives, eds., NACE, Houston, 1990, p263

43 R.A. Oriani, Environment-Induced Cracking of Metals, R.P.Gangloff and M.B. Ives, eds., NACE, Houston, 1990, p264

44 K.Sieradzki and R.C. Newman, Philos. Mag. A, Vol.51(1), 1985, p95

45 F.F.Azhogin, Stress Corrosion Cracking of High Strength Steels, in 3rd Int. Conf. Metallic Corrosion, Moscow, MIR, Vol.2, 1966

46 J.E. Truman, Corro. Sci., Vol.17, 1977, p737

47 R.M. Latanision and R.W. Staehe, Stress corrosion cracking and hydrogen embrittlement of Iron Base Alloys, National Association of Corrosion of Engineers, 1977, p845

48 R.W.Staehle, J.J.Royuela, T.L.Raredon, E.Serrate, C.R.Morin, and R.W.Farrar, Corrosion, Vol.26, 1970, p451

49 H.H.Uhlig, and R.A. White, Trans. ASM, Vol.52, 1960, p830

50 F.S.Lang, Corrosion , Vol.18, 1962, p378t

51 D.G. Tufanov, Metalloved. Term. Obrabotka Met., 15 April 1964

52 D.vanRooyen, in Proc. 1st Int. Conf. Stress Corrosion Cracking, Butterworths, 1961

53 Fundametal aspects of stress corrosion cracking, NACE, 1969,p241

54 K.Fassler in Korrosionum, H.Grafen, F.Kahl, and A.Rahmel, Ed., Vol 1, Verlag Chemie, 1974, p136

55 M.G.Fontana, F.H.Beck, and J.W.Flowers, Met. Prog., Vol.80(6), 1961, p99

56 Gooch, T.C., Honeycombe, J., and Walker, P., British Corrosion Journal, Vol.6, 1971, p148

57 Cihal, V. and Prazak, M.J., Iron and Steel Institute, Vol. 93, 1959, p360

58 K.L.Money and W.W. Kirk, Mater. Perform., Vol 17(7), July 1978, p28

59 E.C. Hoxie, Some corrosion considerations in the Selection of Stainless steel for pressure Vessels and Piping, in Pressure Vessels and piping: A decade of Progress, American Society of Mechanical Engineers, Vol.3, 1977

60 H.Grafen, Corros.Sci., vol.7, 1967, p177

61 H.R.Baker, M.C. Bloom, R.N. Bolser, and C.R.Singleberry, Corrosion, Vol.26, 1970, p420

62 C.P.Dillon, Mater. Perform., Vol. 29(12), 1990, p60

63 Z. Szklarska-Simialowska, Corrosion, vol. 27, 1971, p223

64 E.Brauns and H.Ternes, Werkst. Korros. , Vol. 19, 1968, p1

65 J.W.Oldfield and B.Todd, Mater.Perform., Vol. 29(12), 1990, p57

66 Environmental-Induced Cracking of Metals, R.P.Gangloff and M.B. Ives, Ed., National Association of Corrosion Engineers, 1990

67 Evans, U.R. and Agar, J.N., The Corrosion and Oxidation of Metals, Edward Arnold, 1960, p.862; Evans, U.R., Journal of the Iron and Steel Institute, Vol. 141, 1940, p.219

68 Jaenicke, W., Zeitshrift furPhysikalische Chemie, Vol. A191, 1943, p350

69 Jaenicke,W. and Bonhoeffer, K.F., Zeitschrift fur Physikalishce Chemie, Vol. 193, 1944, p301

70 Copson, H.R., Journal of the Electrochemical Society, Vol.84, 1943, p71

71 Hildebrand, H. and Schwenk, W., Werkstoffe und Korrosion, Vol. 23, 1972, p364

72 Sato, N., Nakagawa, T. , Kudo, K., and Sakashita, M.S. in Localized Corrosion, National Association of Corrosion Engineers , Houston, 1974, p447

73 Galvele, J.R. in Passivity of Metals, R.P. Frankenthal and J. Kruger, Eds., The Electrochemical Society, 1978, p285

74 S.R. Morriosn, Electrochemistry at Semiconductor and Oxidized Metal Electrodes, Plenum Press, New York , 1980

75 W.Schottky, Z.Phys., Vol. 113, 1939, p367

76 S.Piazza, C.Sunseri and F.Di Quarto, AIChE Journal, Vol. 38, 1992, p219

Chapter 3 Experiment Method

3.1 Material and specimen preparation

The corrosion test material used in the experiments was a sheet of 304 austenitic stainless steel with the composition of 18.81% Cr, 1.28% Mn, 8.40% Ni, 0.56% Si, 0.014% Nb, <0.099% Mo, 0.10% V, 0.038% C, 0.11%Ti, 0.13%Co, >0.059W, <0.02Al, 0.12%Cu, 1.28%Mg, and balance Fe.

Before welding, the samples were subjected to solid-solution treatment to obtain a full austenitic structure [1] .The solid-solution treatment process was 1050˚C/1hr./water-quench in flowing argon.

The LW and GTAW processes were used to weld samples. The single pass welds were formed using welding processes without filler metal. Single pass welding minimizes the heat treatment effect of subsequent passes, which may obscure fundamental effects. Fusion runs provide weld metal of identical chemistry to the BM, while changing the microstructure (cast vs. wrought) and imposing a residual stress pattern in the WM and HAZ. For GTAW the input current is 80A, the voltage 8V and the welding speed 200mm/min. The estimated heat input is about 0.19KJ/mm. And for the laser beam welding, the heat input is 0.05KJ/mm.

The working electrodes were plate shaped and mounted on an acrylic resin. The surface was abraded and was finally polished with alumina (2um). Samples for electrochemical tests were embedded in epoxy resin. After embedding, the test surface was grounded by wet SiC paper of decreasing grit size (400, 600, 1200) and was polished

to a 0.5mm diamond paste. Finally, the specimens were rinsed in distilled water, ultrasonically cleaned and dried in air.

3.2 SRET

SRET is a microscopic technique used to identify and quantify regions of localized electrochemical activity on the test surface while immersed in an electrolyte solution. In the present experiments, SRET (EG&G PARC SRET model SP 100) was used to study pitting activity in different welding zones. The probe was leveled and positioned above the sample. The tip was slowly lowered and positioned as close as possible to the specimen surface under the visual control with a telescope. The test solution employed for corrosion measurements was 5×10^{-4}M $FeCl_3$ + 1×10^{-4}M $NaNO_3$. When utilizing the SP100 instrumentation and associated software, anodic currents correspond to negative SRET potentials, while cathodic currents correspond to positive SRET potentials. In order to finish the tests in a reasonable time a DC potential was applied to promote pit initiation.

3.3 Potentiodynamic polarization test

The experiments were conducted in $5x10^{-4}$ M $FeCl_3$ + $1x10^{-4}$ M aqueous solution at ambient temperature and open to the air. Potentiodynamic polarization tests were conducted using Princeton Applied Research Corp. potentiostat/galvanostat control with the Soltran corrosion analysis software CorrWare. A classical cell with three electrodes was utilized, in which the testing specimen is used as the working electrode, the platinum wire counter-electrode had an area of 1 cm^2 and a saturated calomel electrode (SCE) equipped with a Luggin capillary was used as the reference electrode.

3.4 Capacitance measurement and Mott–Schottky analysis

The capacitance measurements were carried out in a buffer solution of composition H_3BO_3 (0.05 M)+$Na_2B_4O_7 \cdot 10H_2O$ (0.075 M) at pH 9.2 deaerated with high-purity nitrogen at room temperature. In order to investigate the effect of applied stress on the nature of passive film, longitudinal welded tensile specimens, as shown in Fig.3-1 were designed to apply tensile stress during the electrochemical measurements.

Before the test the specimens were pre-passivated at 0.5V (vs. SCE) for 2 hours. The potentiodynamic test was started from 0.5V (vs. SCE) and then the potential moved to cathodic direction with a scanning rate of 50mV s^{-1}. The capacitance measurements were performed within the passive range where no redox current was observed during the negative going scan in the voltammetry plots. The polarization was applied by successive displacements of 50 mV in the cathodic direction superimposing a sinusoidal perturbing amplitude 10 mV with the frequency 1000 Hz. The principle is to apply simultaneously a perturbing signal ΔE (10 mV rms) to the cell via the potentiostat and to the reference chain. The response is compared to ΔE dephased by $\Delta\varphi$ and $\Delta\varphi+\Pi/2$. The measured capacitance values were derived from the imaginary component of ac impedance (C=-1/ω Z'').

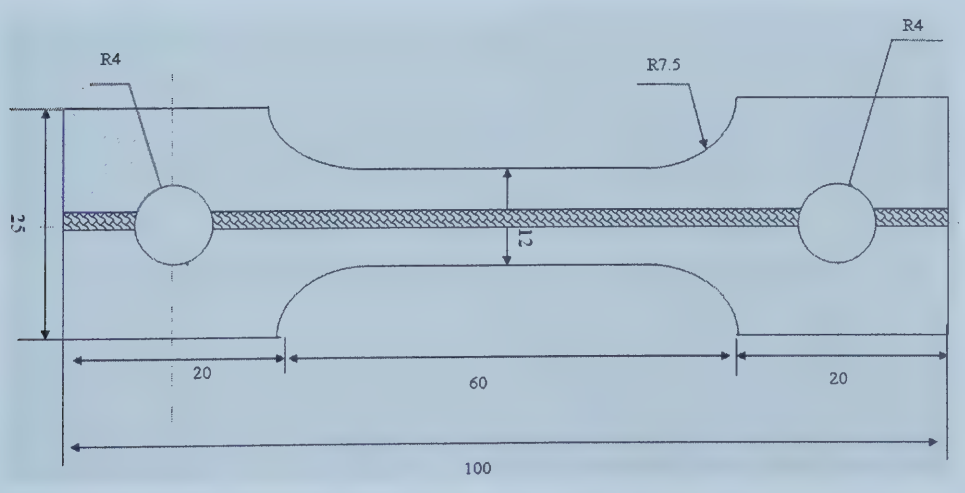

Figure 3-1 Shape of tensile specimens used in static loading tests: dimension in mm

According to the Mott–Schottky theory [2], the relation between the space charge capacitance, C, of an n-type or p-type semiconductor and the electrode potential, E, can be written as equation 2-3 and 2-4. It was assumed that the measured capacitance corresponds to the space charge capacitance, and that additional series capacitances, such as the Helmholtz capacitance and the surface state capacitance, can be negligible. Accordingly, a C^{-2} versus E plot should be a straight line with a slope that is inversely proportional to the doping concentration and with an intercept on the potential axis that yields the flatband potential. In calculation of N_A, and N_D, a value of dielectric constant ε=15.6, was used for the passive films on stainless steel[3].

3.5 Specimens used for SCC tests

Tapered gauge length tensile test specimens with welds in the axial orientation were used in the tests. The specimen configuration is shown in Fig.3-2 and Fig.3-3. Before SCC testing, the specimen surfaces were ground with silicon carbide (SiC) papers of 240, 400 and 600 grit, successively, and then rinsed with deionized water and acetone.

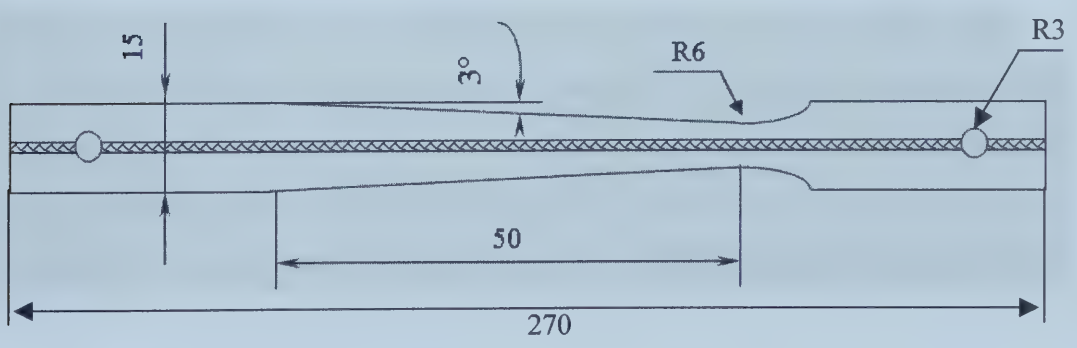

Figure 3-2 Tapered LW specimens with longitudinal weld: dimension in mm

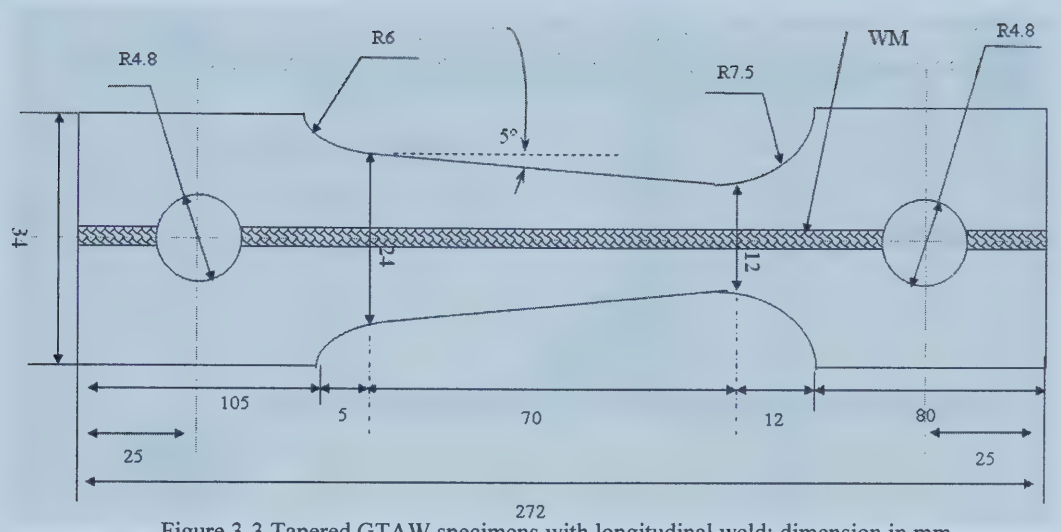

Figure 3-3 Tapered GTAW specimens with longitudinal weld: dimension in mm

3.6 SCC tests

The constant load SCC tests were conducted in a custom-built testing machine as shown in Fig 3-4. The corrosion solution of a 1 M NaCl + 0.5 M HCl was prepared from analytical grade regent and distilled water. During testing, only the testing section of the specimen was immersed in a corrosion cell and a constant stress, which was approximately equal to the yield strength of material, was held on the minimum transversal cross section of the tapered specimens. After the test, the fracture surface was analyzed with the scanning electronic microscope.

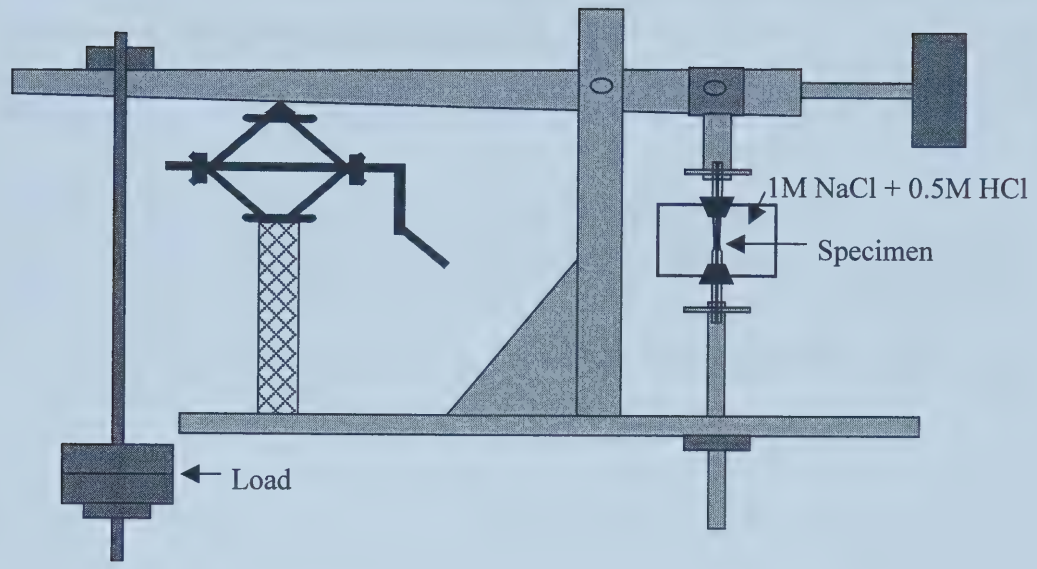

Figure 3-4 Setup for the electrochemical measurements of stressed specimens

3.7 Crack size measurements

To monitor the cracks, the tests were interrupted at different intervals and the number and sizes of the cracks on the specimen surface were measured. In order to investigate the effect of microstructure of welded specimens on the SCC behavior, specimens were divided into three zones, the WM, the HAZ adjacent to the fusion zone with 2mm width and the edge zone of specimen, the BM. An optical microscope equipped with the Image-Pro Plus software was used to measure crack sizes.

When the test is finished, the crack depth was measured on the longitudinal cross section surfaces. To identify the relationships between the crack depth and applied stress, the side surfaces of specimens were ground to 600-grit finish, then polished to 0.5μm Al_2O_3 paste surface finish. Finally they were washed with water, dried with methanol for observation under optical microscopy to reveal the distribution of cracks on the

cross-section area. To examine the WM region, the specimens were cut in the middle of the fusion zone along the longitudinal direction.

References

1 Erich Folkhard, Welding metallurgy of stainless steel, 1988, p199

2 S.R. Morrison, Electrochemistry at Semiconductor and Oxidized Metal Electrodes, Plenum Press, New York , 1980, pp. 49–64, 72–78, 126–128, 154–155, 163

3 A.M.P. Simoes, M.G.S. Ferreira, B. Rondot and M.da Cunha Belo, J.Electrochem. Soc., Vol.137, 1990, p82

Chapter 4 Effect of Welding Processes on Initiation and Propagation of Pitting and SCC

4.1 *In-Situ* observation of pitting initiation and propagation with SRET

As a region of localized electrochemical activity is encountered, the ionic current flow produces a potential gradient in the solution above this region. The potentials measured at the high and low points of the tip reflect various localized sites over the sample surface, as illustrated in Fig. 4-1 and 4-2. At 0.38V (vs. SCE), Figure 4-1(c) shows an anodic activity on a GTAW specimen surface, indicating that one pit initiated and propagated in the WM. Since the sign of the potential difference indicates whether the local current is cathodic or anodic, the positive potential peak corresponds to the anodic zone while the negative peak to the cathodic zone. After 3 hours one pit was observed visually (Figure 4-1(d)). But for LW specimens, no anodic activity was observed during the same period of tests with SRET (Figure 4-1(a)). This suggests that no pitting event occurred under this condition and it is confirmed by the photography shown in Figure 4-1(b). After activated for 2 hours at 0.9V (vs. SCE), four peaks corresponding to anodic areas were detected on LW specimen with SRET, as shown in Figure 4-2(a). The four anodic regions developed and eventually became pits as observed visually in the BM after 3 hours (Figure 4-2(b)). As shown in Figure 4-2(c) for GTAW specimens, two anodic zones were detected by SRET immediately after the same anodic potential is applied. The two anodic areas then propagated until pits were visually

observed on the WM after 3 hours, as shown in Figure 4-2(d). It is evident that WM of LW specimen is less susceptible to pitting than that of GTAW one at the same polarization potential.

To illustrate the correlation between anodic activity and microstructure, Figure 4-4(b) shows a pit formed on the base metal (with a fully austenitic structure) in the LW specimen, corresponding to the zone where high anodic activity was observed in the *in-situ* SRET test. Figure 4-3(a) shows a pit on the WM of GTAW sample with a small amount of ferrites embedded in the austenite matrix. This finding suggests that in GTAW the weld zone has higher anodic activity than the base metal. Based on the results shown above, it seems that under the same potential, WM formed in the LW process is cathodic to the BM, which makes the BM preferable for localized corrosion. However, the WM formed in the GTAW process seems anodic to the BM, which makes the WM a preferable site for localized corrosion.

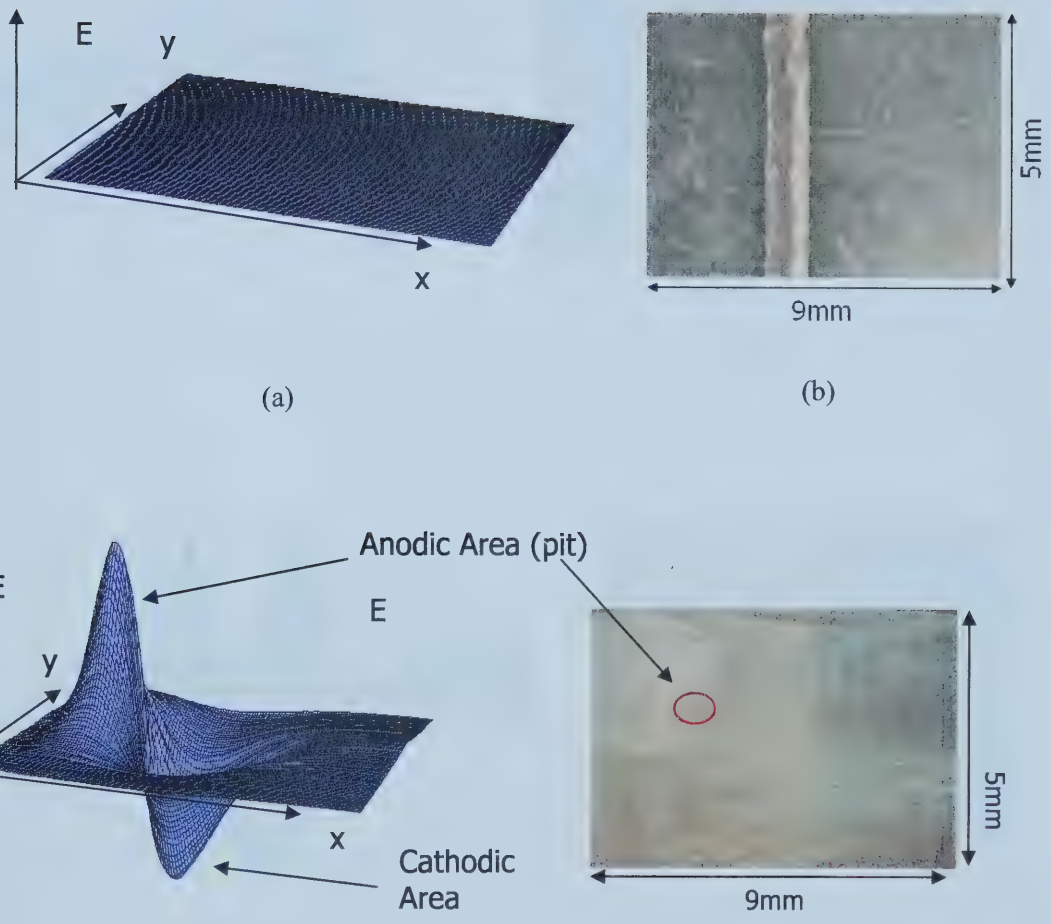

Figure 4-1 (a) SRET two-dimensional images for LW 304 stainless steel in $5x10^{-4}$ M $FeCl_3$+$1x10^{-4}$ M $NaNO_3$ solution (b) No pits were observed on base metal for laser welded 304 stainless steel (c) SRET two-dimensional images for GTAW 304 stainless steel in $5x10^{-4}$ M $FeCl_3$+$1x10^{-4}$ M $NaNO_3$ solution (pit initiation time: 1 hr, scanning area: 5 x 9 mm^2) (d) pits observed on weld metal for laser welded 304 stainless steel after 3 hrs (Applied potential: 0.38 V (vs. SCE))

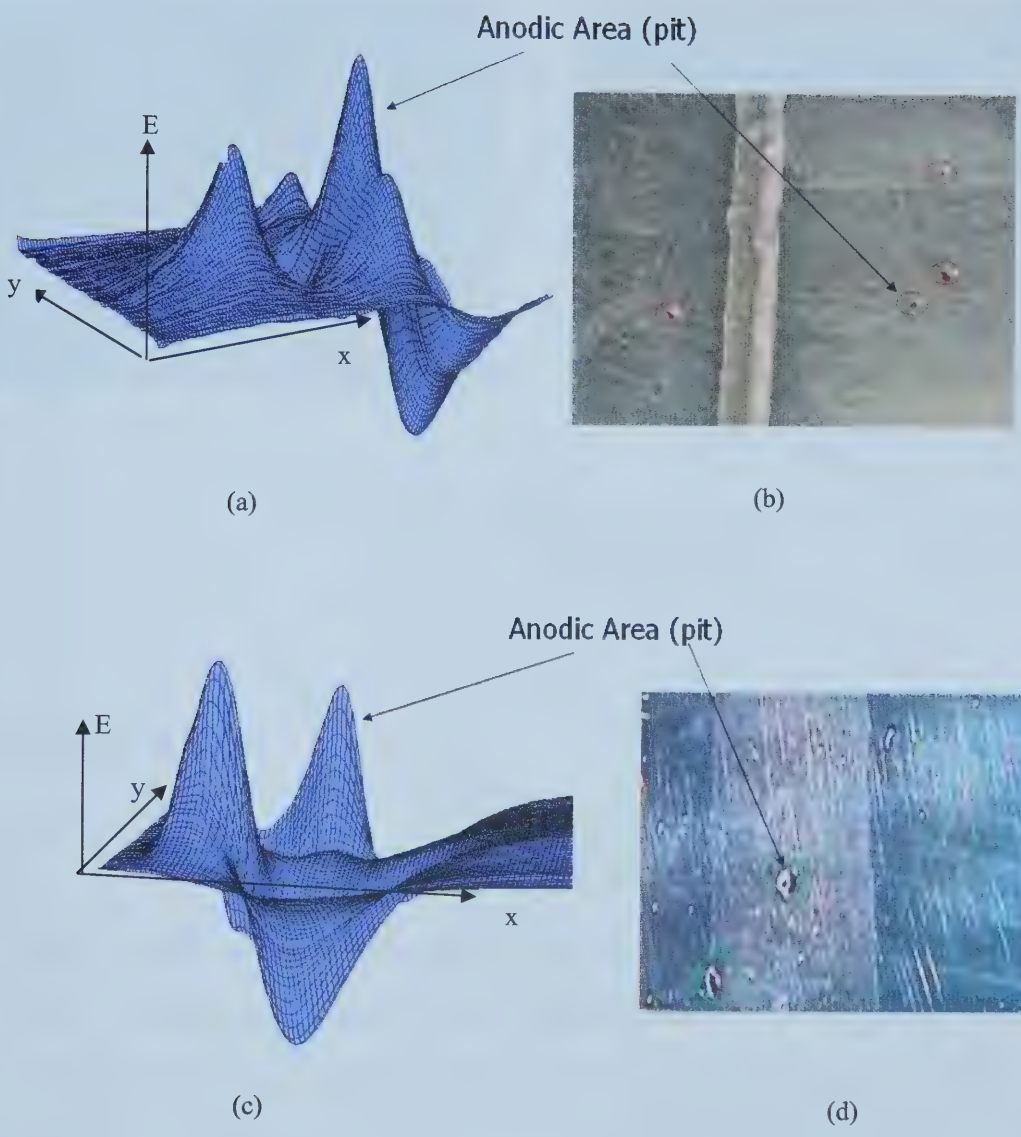

Figure 4-2 (a) SRET three-dimensional images for LW 304 stainless steel in $5x10^{-4}$ M $FeCl_3$ + $1x10^{-4}$ M $NaNO_3$ solution(pit initiation time: 2 hr, scanning area: $5x9mm^2$) (b)Four pits observed in base metal for laser welded 304 stainless steel after 3 hrs (c) SRET three-dimensional images for GTAW 304 stainless steel in $5x10^{-4}$ M $FeCl_3$ + $1x10^{-4}$ M $NaNO_3$ solution((pit initiation time: 0 hr, scanning area:$5x9mm^2$) (d)Pits observed in weld metal for laser welded 304 stainless steel after 3 hrs (Applied potential: 0.9 V (vs. SCE))

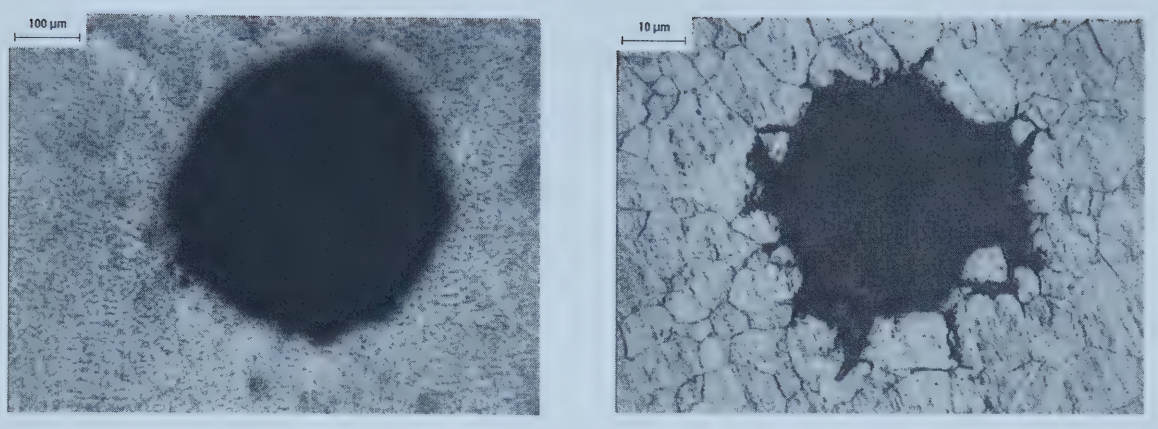

(a) (b)

Figure 4-3 (a) Pits observed in the WM after GTAW
(b) Pits observed in the BM after LW

4.2 Pitting potential

The pitting potential E_{pp} is defined as the electrode potential over which pits will intiate and grow and it is often used to show the pitting resistance of material under certain environments. A higher pitting potential indicates higher pitting corrosion resistance. The pitting potential of a material is experimentally determined from the potential dynamic curves. As shown in Figure 4-4, $E^{WM}_{pp\ (GTAW)} < E^{HAZ}_{pp\ (GTAW)} < E^{BM}_{pp} < E^{WM}_{pp\ (LW)}$ suggests that the pitting potentials depend on the metallurgical features of the materials. For the LW specimen, the breakdown of the passive film does not occur in the WM of the LW specimens before the evolution potential for dissolved oxygen is reached. This is due to a relatively higher potential scanning rate used in the polarization measurement. Under a stable (potential static)

condition, the pitting potential will be lower than that measured by the potentiodynamic test. The data in Figure 4-4 suggest that the pitting potential in the WM of the LW specimen should be higher than that of the GTAW and BM. The results agree well with those obtained from the SRET experiments.

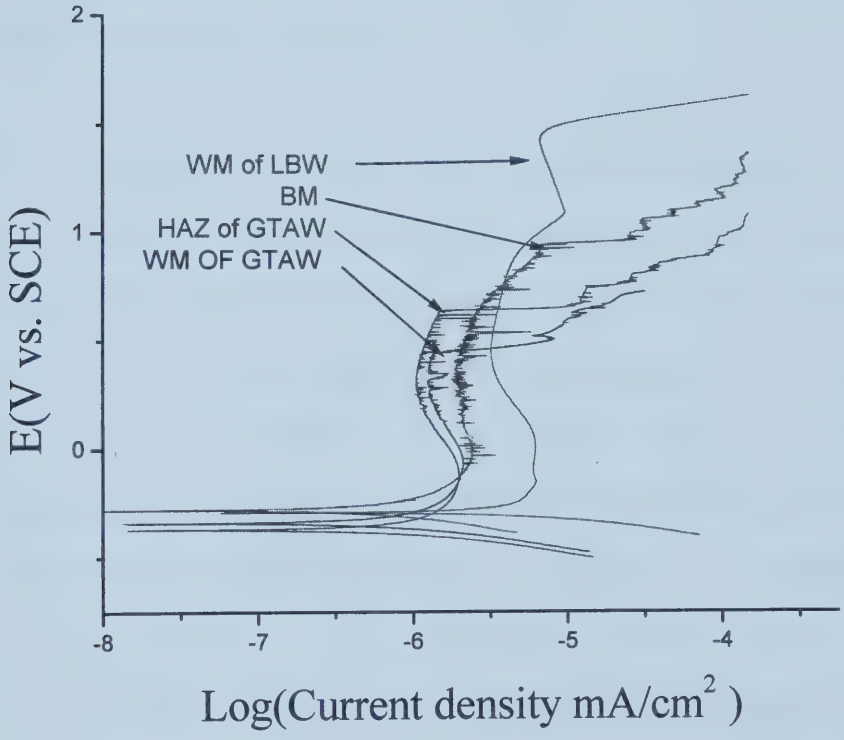

Figure 4-4 Potentiodynamic polarization curves for weld metal, base metal and HAZ of GTA welded 304 stainless steel in 5×10^{-4} M $FeCl_3$ + 1×10^{-4} M $NaNO_3$ solution

4.3 SCC Initiation and propagation

Crack initiation could not be detected with the aid of an optical microscope until the specimen was loaded in the corrosive environment more than 4 hours. Then, both densities and sizes of cracks observed increased with increasing test duration and applied stress level, as shown in Fig.4-5 and 4-6.

For LW, the surface cracks in HAZ and BM initiated and propagated in the planes perpendicular to the tensile stress, as expected, and many branches were found on single crack, as shown in Fig.4-7b. The SEM observation on the fracture surface indicates that the cracks initiate and propagate initially in a transgranular manner (Fig 4-8(a)) but the crack growth mechanism transforms to an intergranular mode when the crack size reaches a critical value (Fig.4-8(b)). The mechanism for the crack growth mode transition is not yet understood. It is speculated that there is no active path in LW specimen for the crack to proceed preferentially, because no sensitization zone exists in the HAZ. After the cracks initiate, they tend to change their direction along the grain boundary. However, for GTAW the surface cracks in HAZ mainly initiate and propagate in the transgranular manner or mixed mode(Fig. 4-8(c) and 4-8(d)). The mixed mode could arise from the slight sensitization of HAZ, which is likely to promote intergranular cracking.

Figure 4-7(a) shows that the cracks in the WM after LW are likely to initiate and propagate in inclined planes with an angle of about 30° to the direction of the maximum principle tensile stress. This could be ascribed to the direction of crystal growth

determined by the direction of greatest dissipation of heat. As the welding gun move during the welding process, the direction of crystallization will assume an angle to the moving direction of welding gun. The fractography in Fig.4-9 indicates that the cracking is along the dendrite boundary, where δ ferrite exists (the dark phase in Fig 4-7(a)), which suggests that it may affect the crack propagation. Some studies indicate that δ ferrite is likely to dissolve preferentially[1,2,3]. For GTAW, the cracks also propagate in inclined planes with an angle of about 30° to the direction of the maximum principle tensile stress as shown in fig. 4-7(c).

As shown in Fig. 4-10, the crack propagation mode in BM is the mixed transgranular cracking and ductile dimple. When the crack size reaches a certain size, the final rupture region is approached and plastic deformation is appreciable. At the fracture surface, only ductile dimples could be found. It indicates that fracture is mainly non-environmental. Usually it is a form of ductile overload failure.

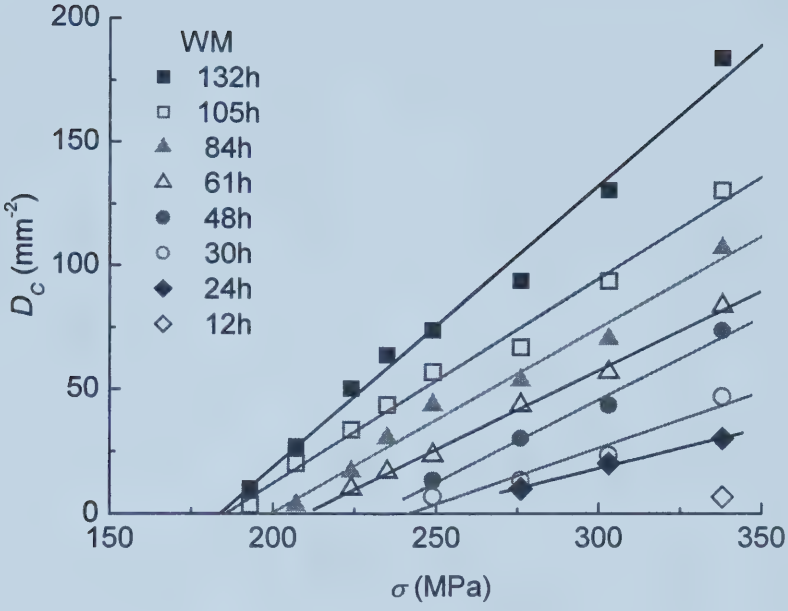
WM
132h
105h
84h
61h
48h
30h
24h
12h
D_C (mm^{-2})
σ (MPa)
0
50
100
150
200
150
200
250
300
350

(a)

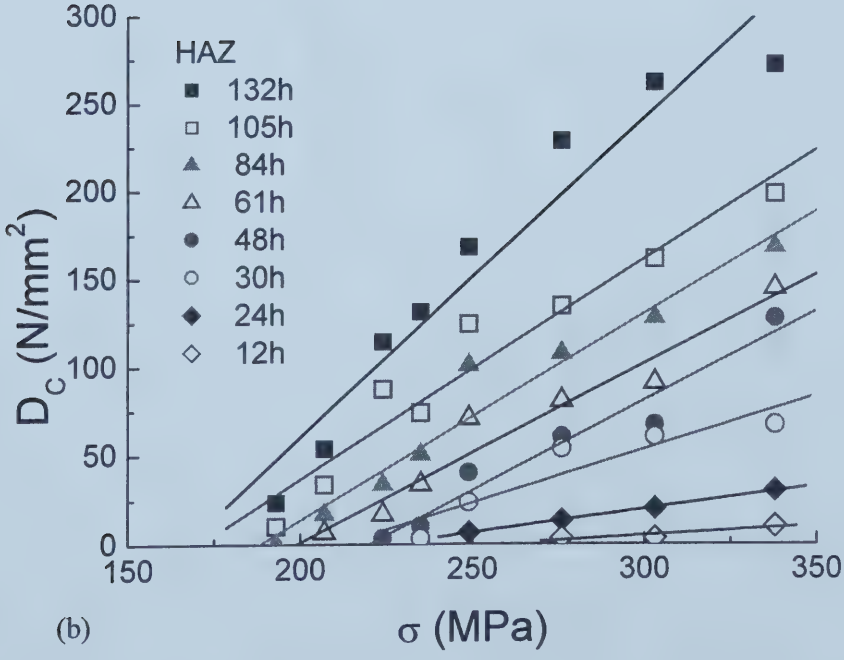
HAZ
132h
105h
84h
61h
48h
30h
24h
12h
D_C (N/mm^2)
σ (MPa)
0
50
100
150
200
250
300
150
200
250
300
350

(b)

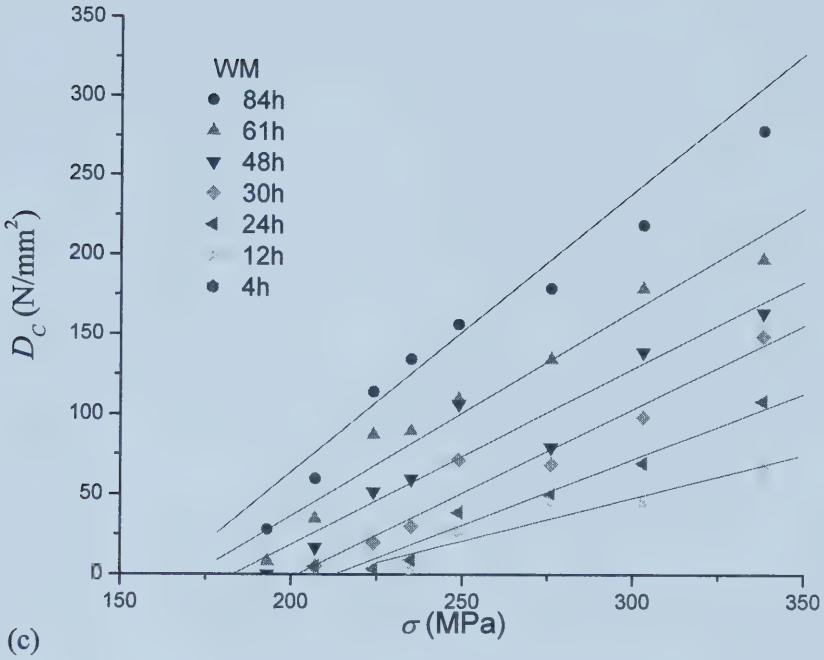
WM
84h
61h
48h
30h
24h
12h
4h
D_C (N/mm^2)
σ (MPa)
0
50
100
150
200
250
300
350

(c)

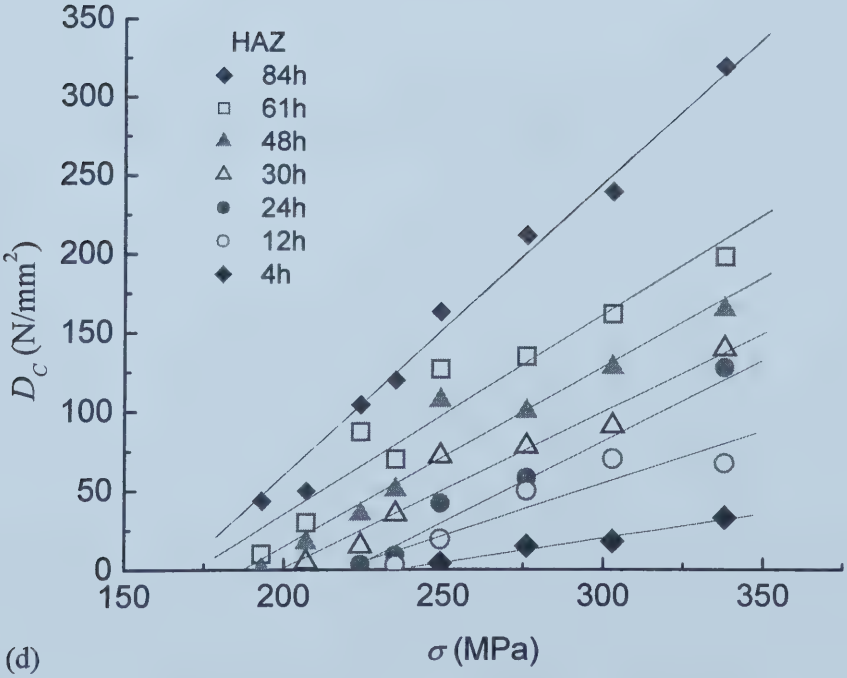
HAZ
84h
61h
48h
30h
24h
12h
4h
D_C (N/mm^2)
σ (MPa)
0
50
100
150
200
250
300
350

(d)

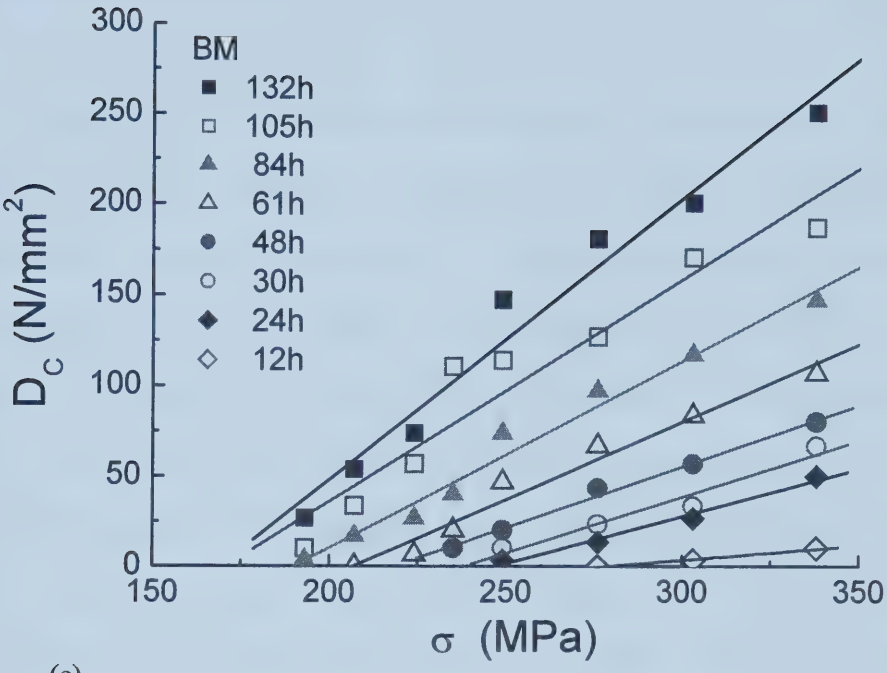

(e)

Figure 4-5 Dependence of crack densities on the stress level and test duration (a-b) LW (c-d) GTAW (e) BM

4.4 SCC initiation kinetics

There were two factors that affect the measured crack density, D_C, small crack initiation and crack coalescence. The measured D_C values would be reduced by the crack coalescence. In order to illustrate the SCC initiation kinetics of material, the crack densities were expressed as a function of test duration, t, as indicated in Fig.4-11, and the slope of curves D_C vs. t was defined as the crack initiating rate, dD_C/dt^4. The results in Fig.4-11 show that dD_C/dt is approximately independent of the duration but depends on the applied stress. For LW, it is found in Fig.4-12(b) that the crack initiating rates in the BM and HAZ are almost the same but higher than those in the WM. This means that the crack densities in the WM are lower than those in the BM and HAZ. Conversely, the crack initiating rates in the WM and HAZ after GTAW are higher than those in the BM, as shown in Fig.4-12(a). The results in Fig.4-12 indicate that the correlation between the crack initiating rates and applied stress in the different zones of welded specimens can be empirically formulated as follows:

$$\frac{dD_C}{dt} = \alpha \sigma^{\beta} \tag{4-1}$$

where α and β are the constants determined by experiments. The values of α and β experimentally determined are listed in Fig.12.

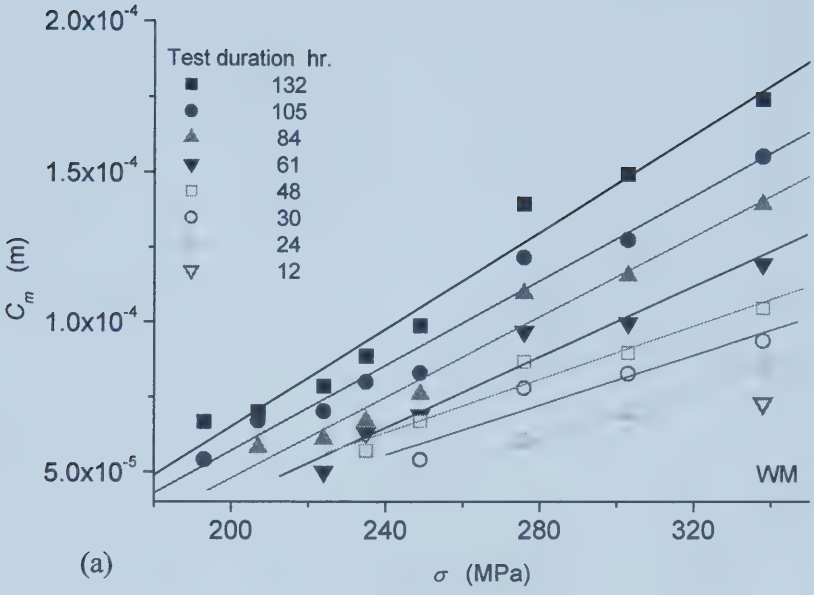
2.0x10-4
1.5x10-4
1.0x10-4
5.0x10-5
Cm (m)
Test duration hr.
132
105
84
61
48
30
24
12
WM
200
240
280
320
σ (MPa)

(a)

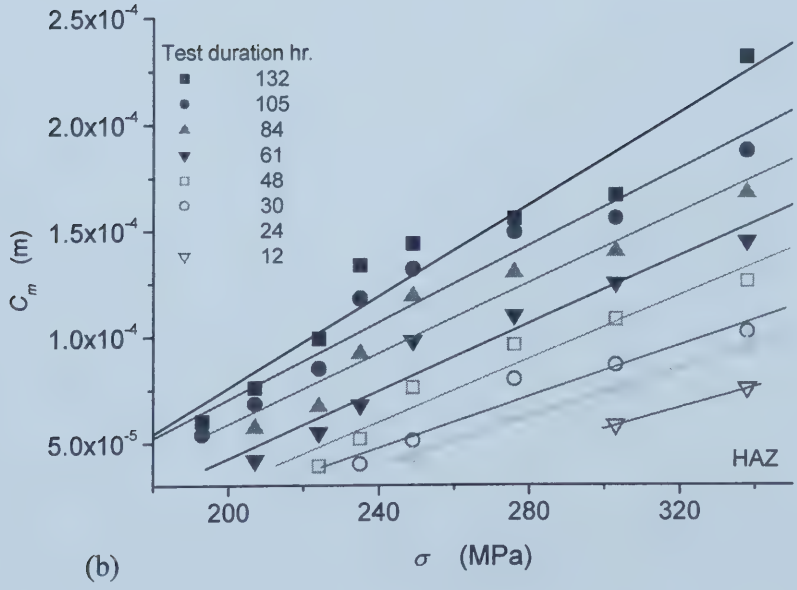
2.5x10-4
2.0x10-4
1.5x10-4
1.0x10-4
5.0x10-5
Cm (m)
Test duration hr.
132
105
84
61
48
30
24
12
HAZ
200
240
280
320
σ (MPa)

(b)

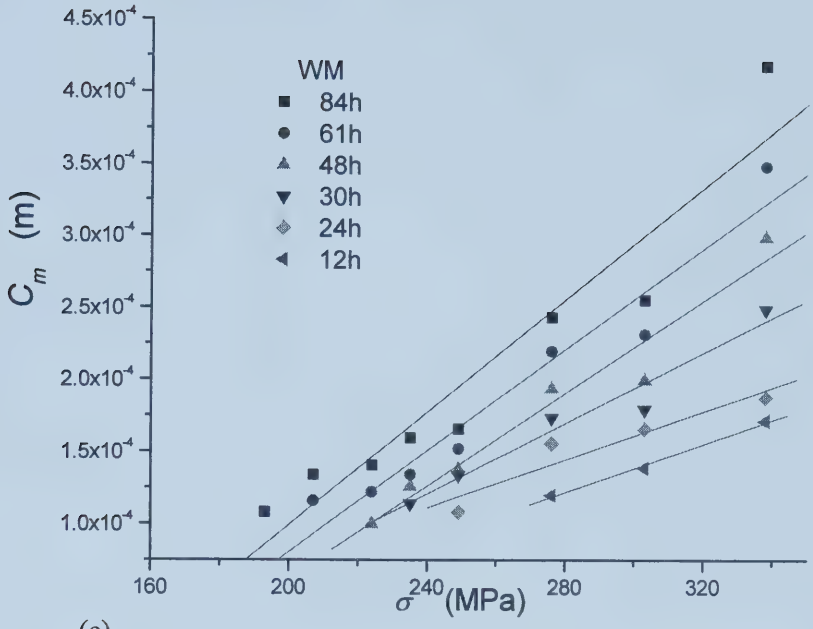
WM
84h
61h
48h
30h
24h
12h
C_m (m)
σ^{240}(MPa)
4.5x10^{-4}
4.0x10^{-4}
3.5x10^{-4}
3.0x10^{-4}
2.5x10^{-4}
2.0x10^{-4}
1.5x10^{-4}
1.0x10^{-4}
160
200
280
320

(c)

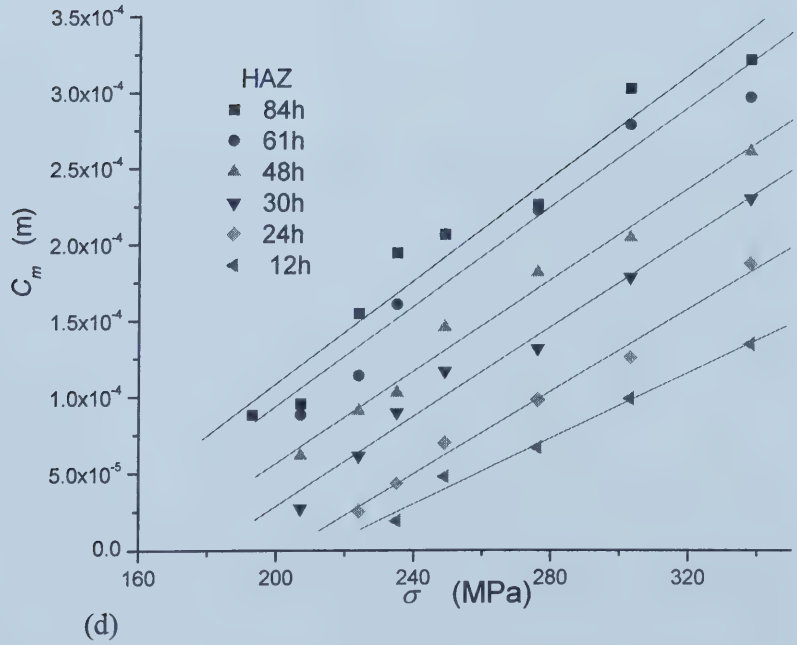
HAZ
84h
61h
48h
30h
24h
12h
C_m (m)
σ (MPa)
3.5x10^{-4}
3.0x10^{-4}
2.5x10^{-4}
2.0x10^{-4}
1.5x10^{-4}
1.0x10^{-4}
5.0x10^{-5}
0.0
160
200
240
280
320

(d)

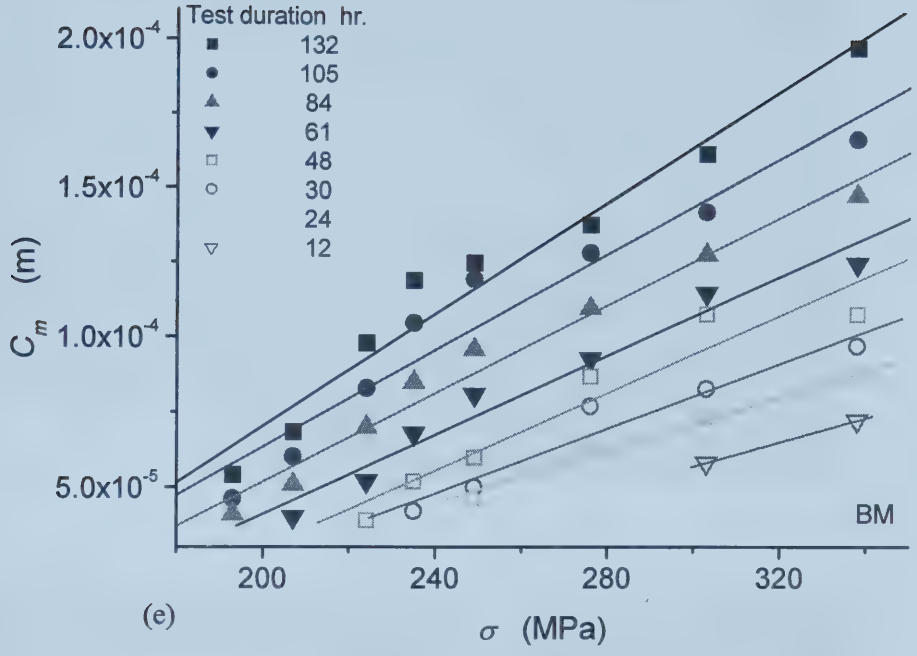

Figure 4-6 Dependence of average surface crack length on the stress level and test duration (a-b) LW (c-d) GTAW (e) BM

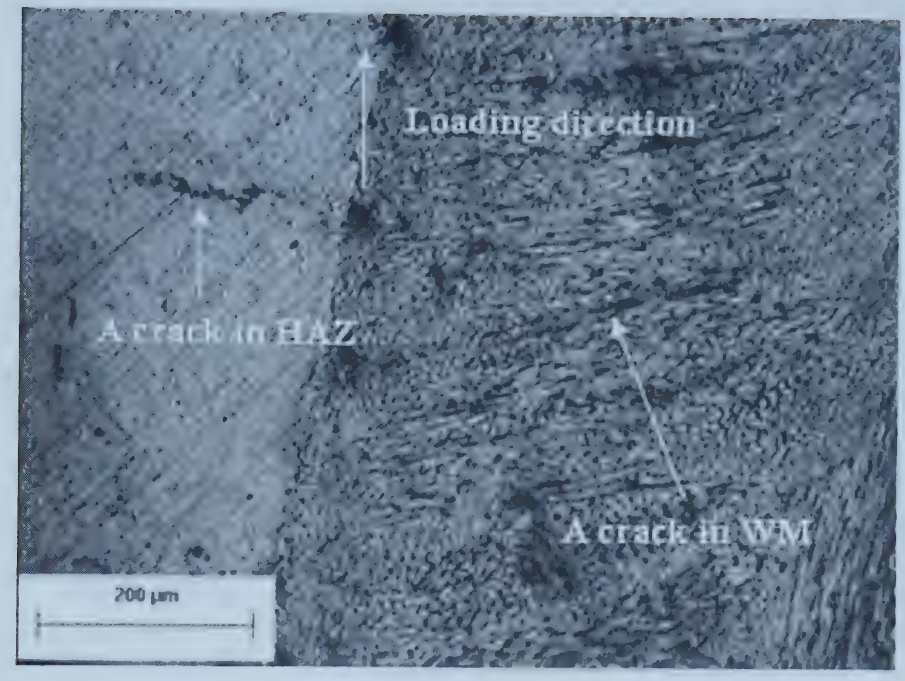

(a) Cracks in HAZ and WM after LW

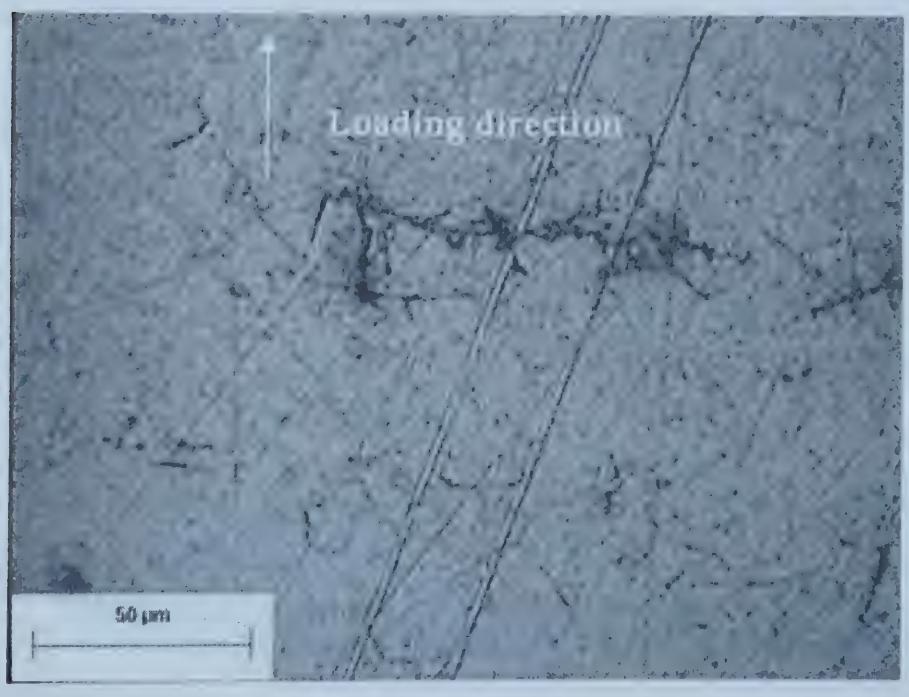

(b) A crack in BM after LW

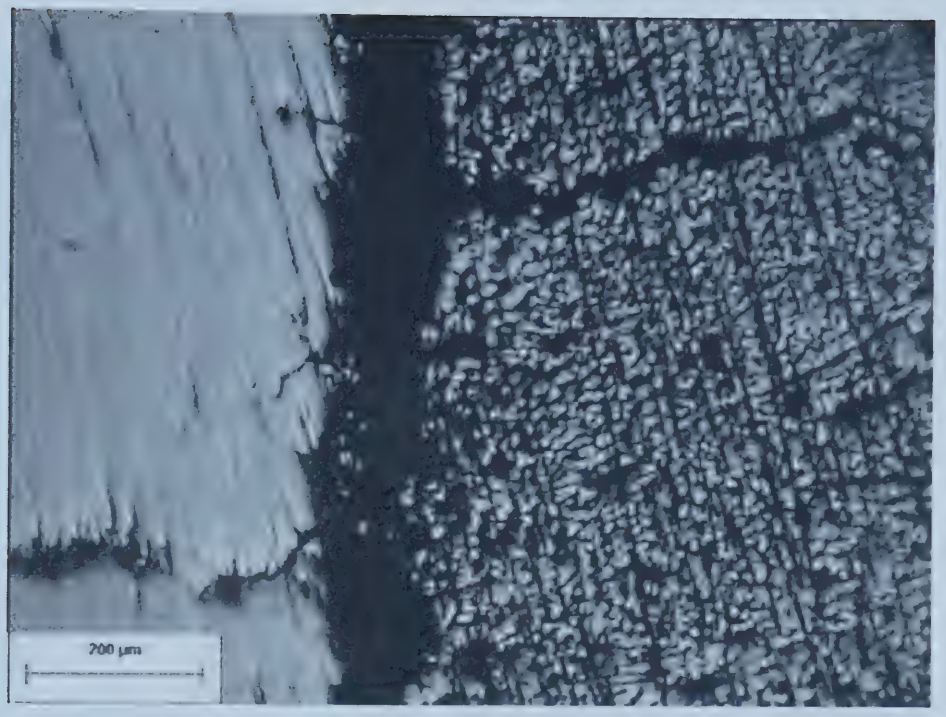

(c) Cracks in HAZ and WM after GTAW

(d) A crack in BM after GTAW

Figure 4-7 Crack morphology in various zones

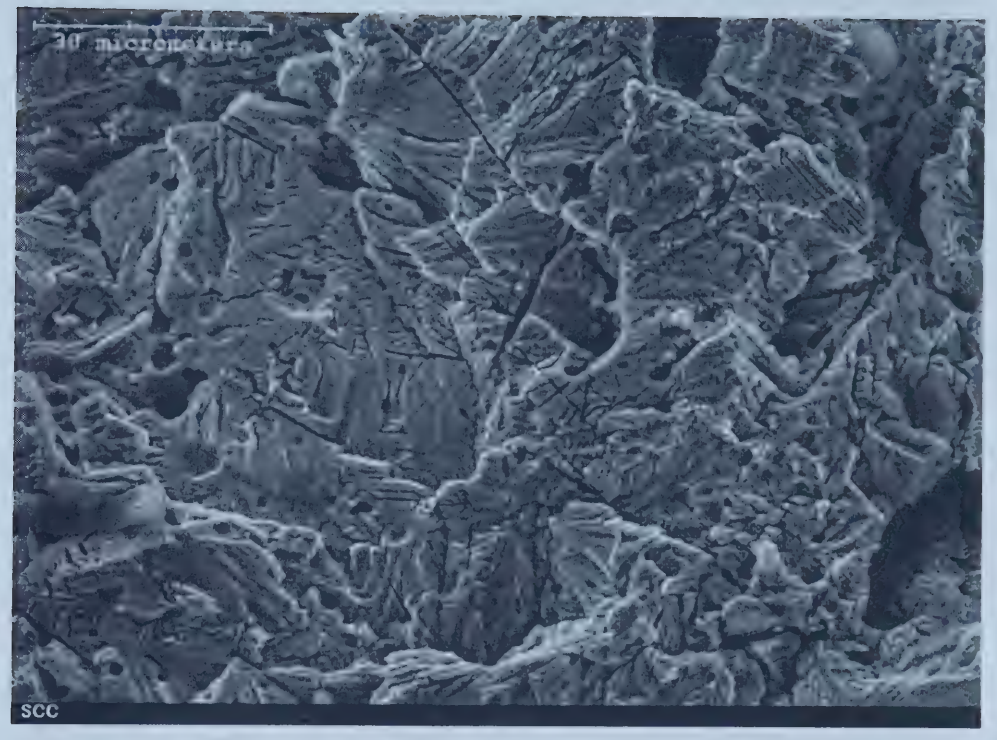

(a) Trangranular SCC

(b) Intergranular SCC

(c) Transgranular SCC

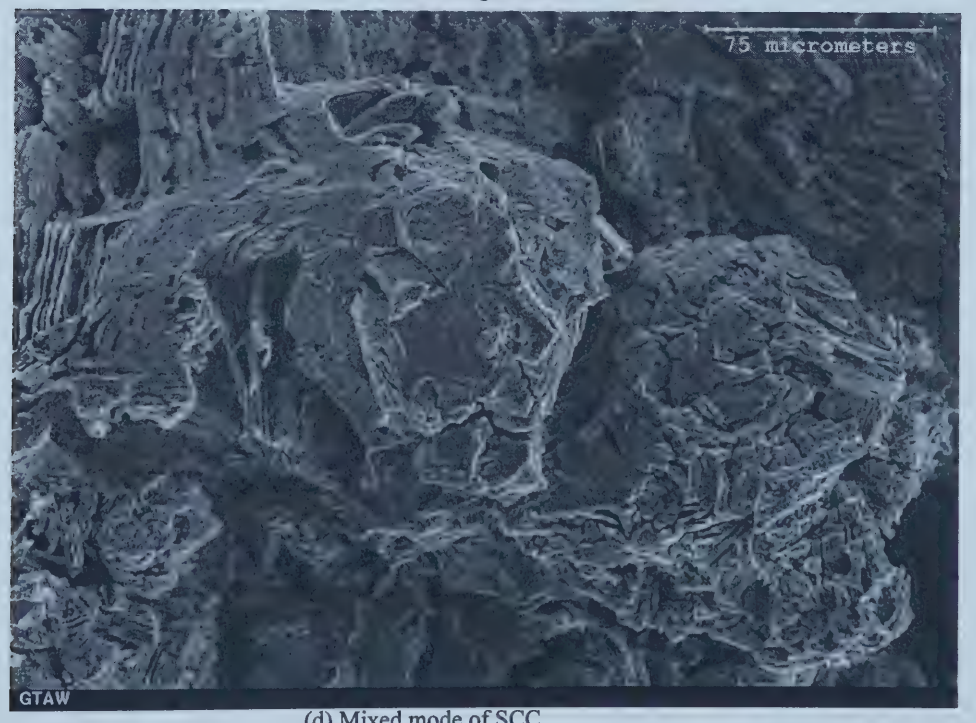

(d) Mixed mode of SCC

Figure 4-8 Factography of SCC (a-b) HAZ of LW (c-d) HAZ of GTAW

(a)

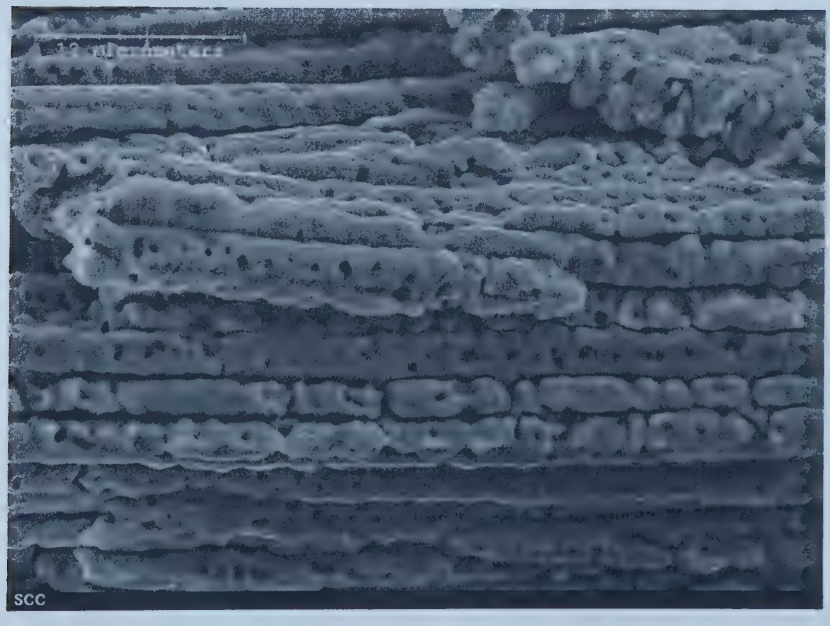

(b)

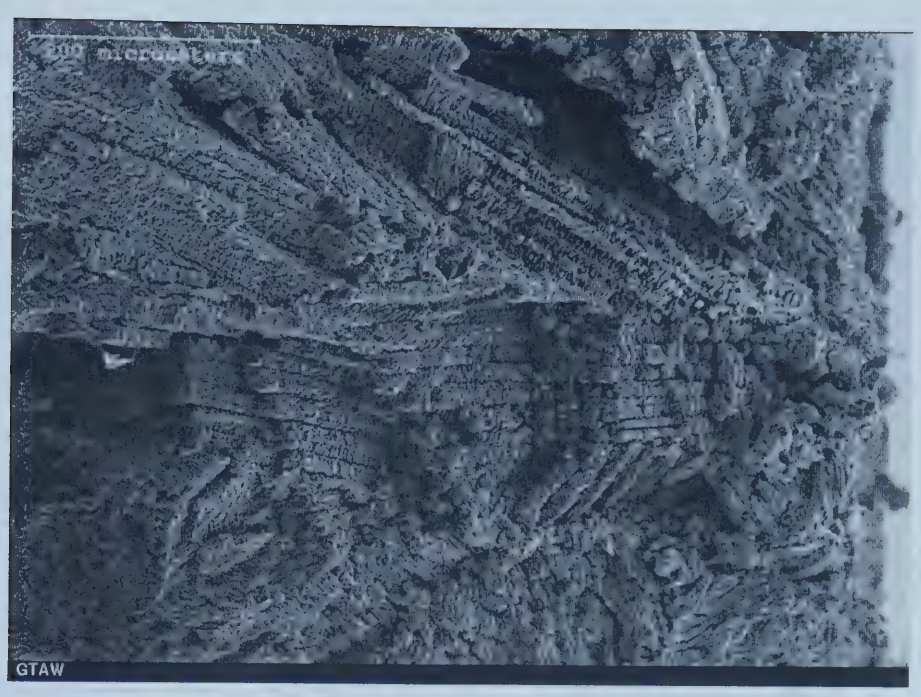

(c)

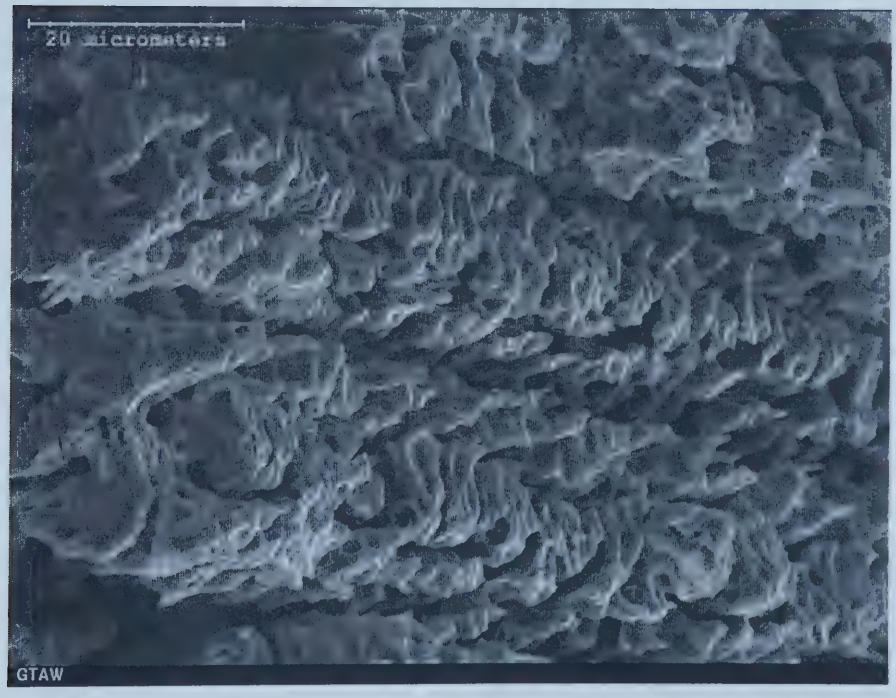

(d)

Figure 4-9 Fractography of SCC (a-b) in the WM of LW (c-d) in the WM for GTAW

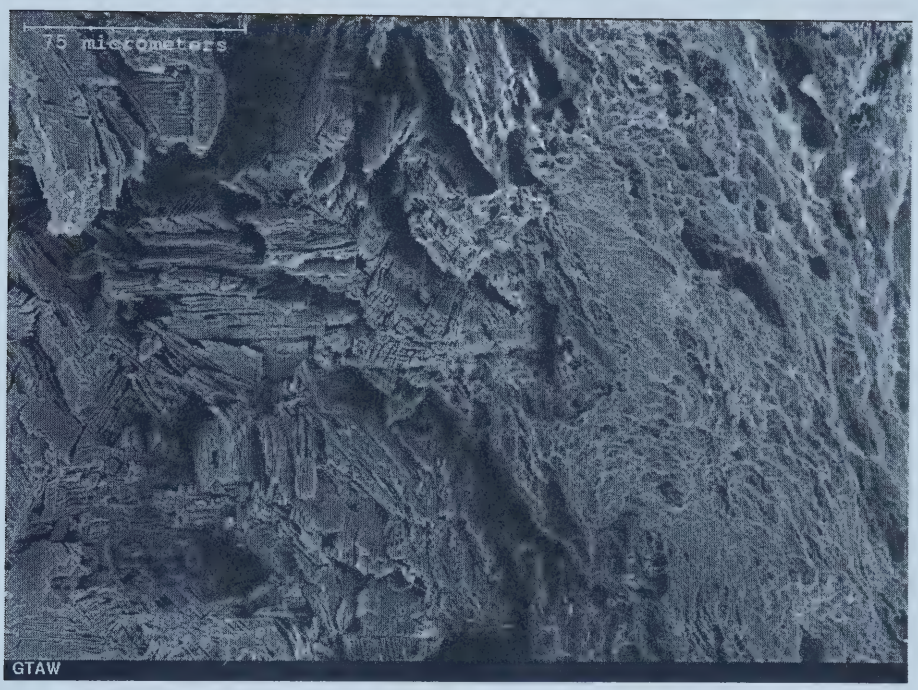

Figure 4-10 Fractography of SCC in the BM

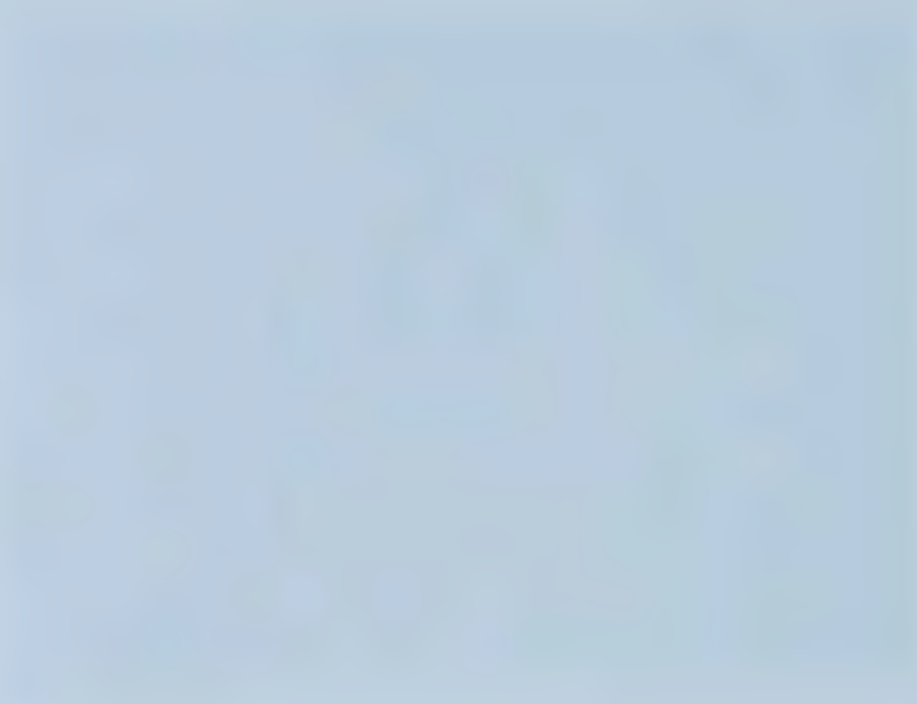

The test data in Fig.4-5 show that, for the first order of approximation, the curves of crack density vs. stress can be fitted by the linear regression method. The values of the critical stress to initiate a crack at a given time will be determined by extrapolating the lines to a crack density of zero. Following a similar procedure, the critical time to initiate SCC under a given applied stress level can also be determined from the test data in Fig.4-11. The correlation between the critical stress to initiate SCC and the critical time needed to initiate SCC under the same applied stress is given in Fig.4-13 and it is referred as the SCC initiation time curve. The results in Fig.4-13 show that the SCC initiation time of material increases with decreasing stress level. Little difference exists in the SCC initiation time of the LW specimens in various zones. On the contrary, for GTAW, the SCC initiation time in WM and HAZ is shorter than those after LW at the same stress level. Also the critical stress to initiate a crack at a given time in the WM and HAZ after GTAW is lower than after LW. The correlation between the SCC initiation lifetime, t_i, and applied stress σ is formulated by the following empirical expression:

$$t_i = A\sigma^{-n} \tag{4-2}$$

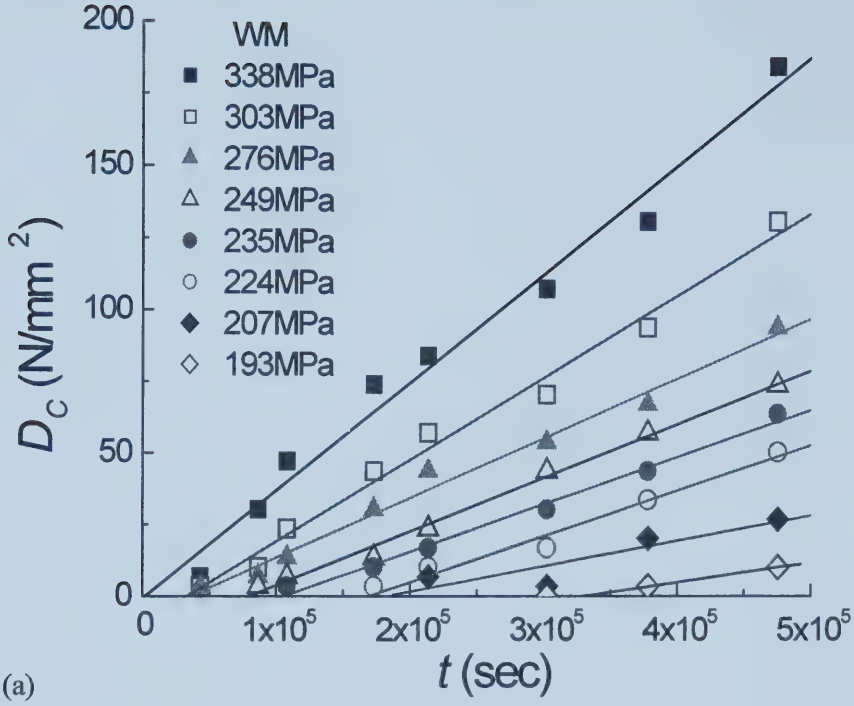
WM
338MPa
303MPa
276MPa
249MPa
235MPa
224MPa
207MPa
193MPa
D_C (N/mm^2)
t (sec)
0
50
100
150
200
1x10^5
2x10^5
3x10^5
4x10^5
5x10^5

(a)

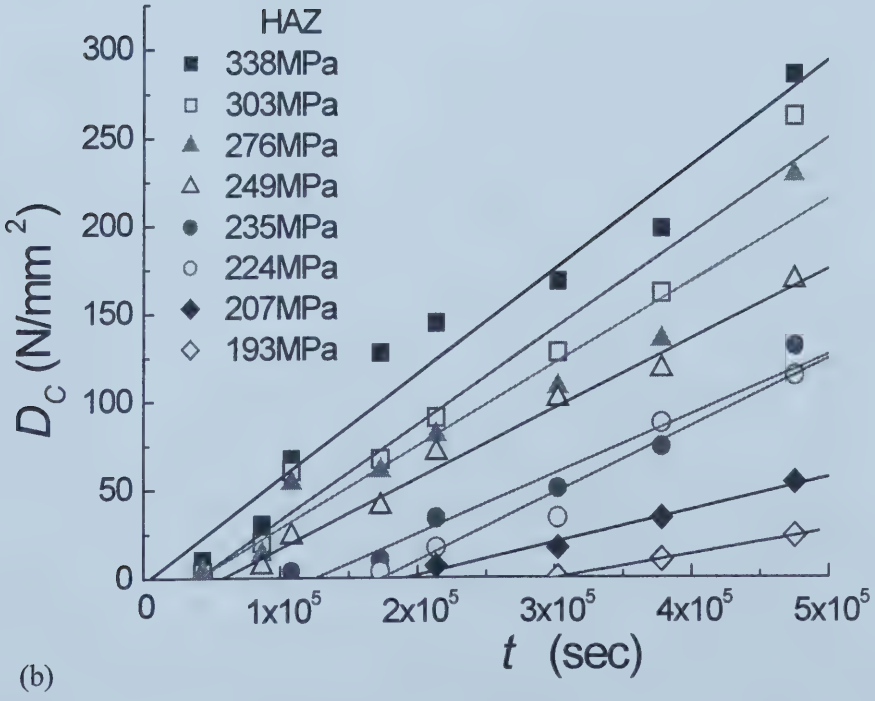
HAZ
338MPa
303MPa
276MPa
249MPa
235MPa
224MPa
207MPa
193MPa
D_C (N/mm^2)
t (sec)
0
50
100
150
200
250
300
1x10^5
2x10^5
3x10^5
4x10^5
5x10^5

(b)

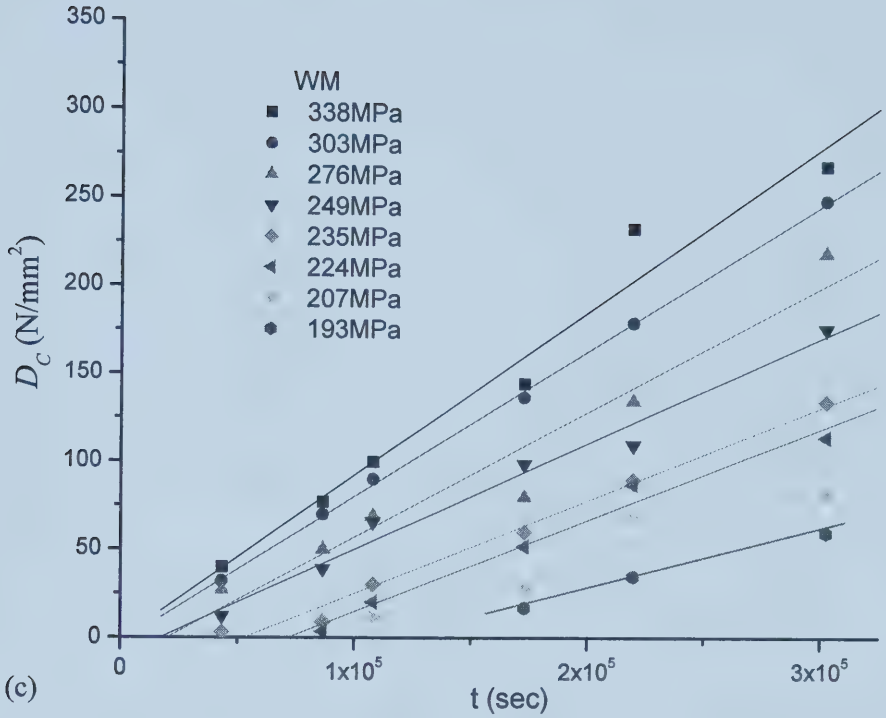
WM
338MPa
303MPa
276MPa
249MPa
235MPa
224MPa
207MPa
193MPa
D_C (N/mm^2)
t (sec)
0
50
100
150
200
250
300
350
1x10^5
2x10^5
3x10^5

(c)

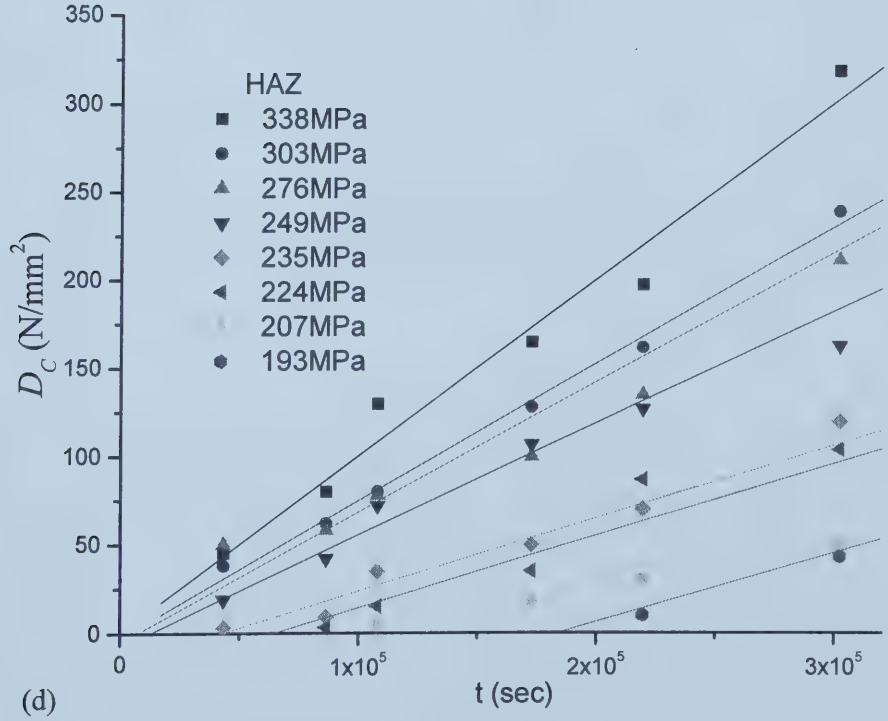
HAZ
338MPa
303MPa
276MPa
249MPa
235MPa
224MPa
207MPa
193MPa
D_C (N/mm^2)
t (sec)
0
50
100
150
200
250
300
350
1x10^5
2x10^5
3x10^5

(d)

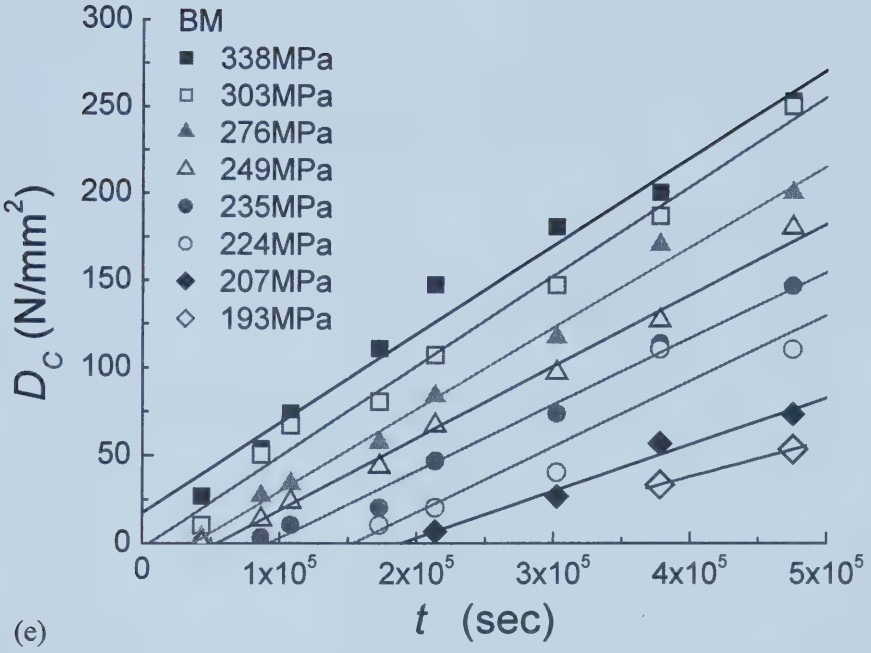

(e)

Figure 4-11 Correlation between crack densities and test duration
(a-b) LW (c-d) GTAW (e) BM

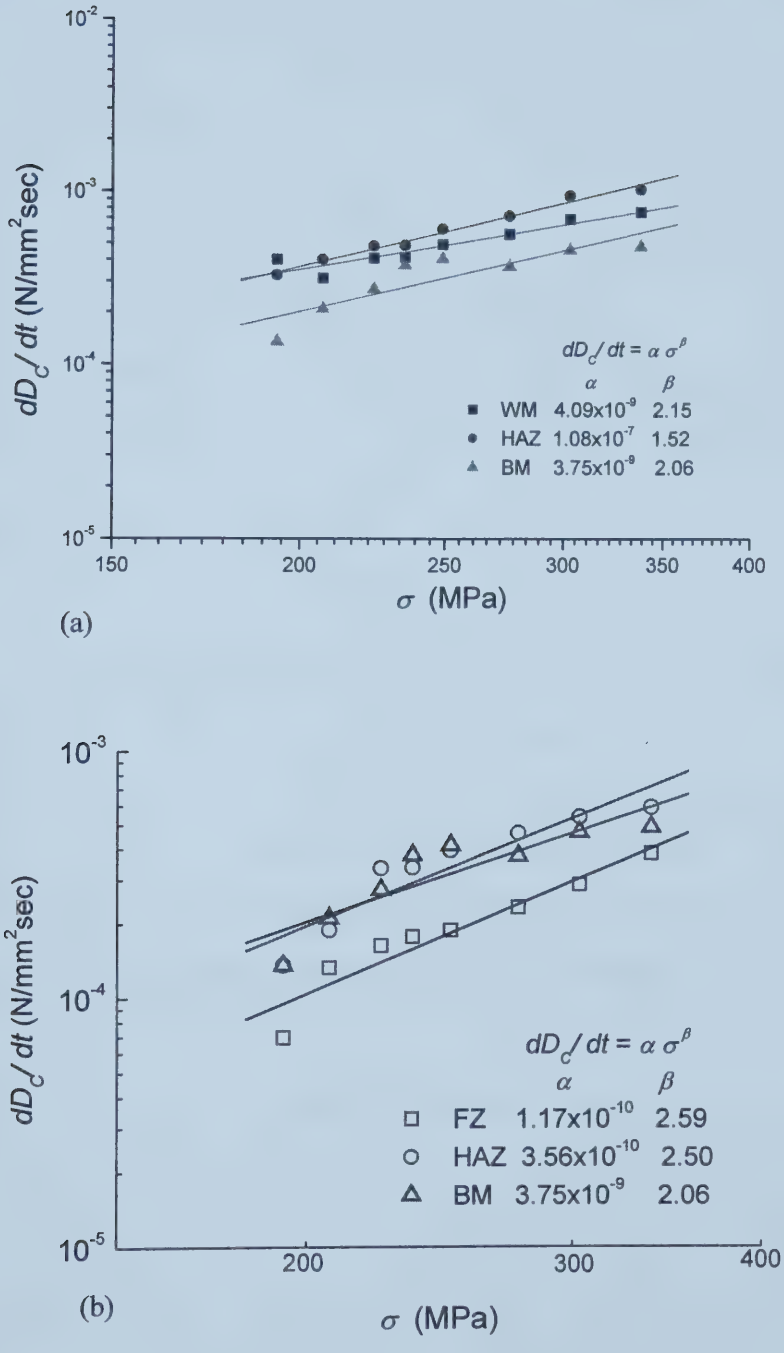

Figure 4-12 Dependence of crack initiating rates on applied stress level (a) GTAW (b) LW

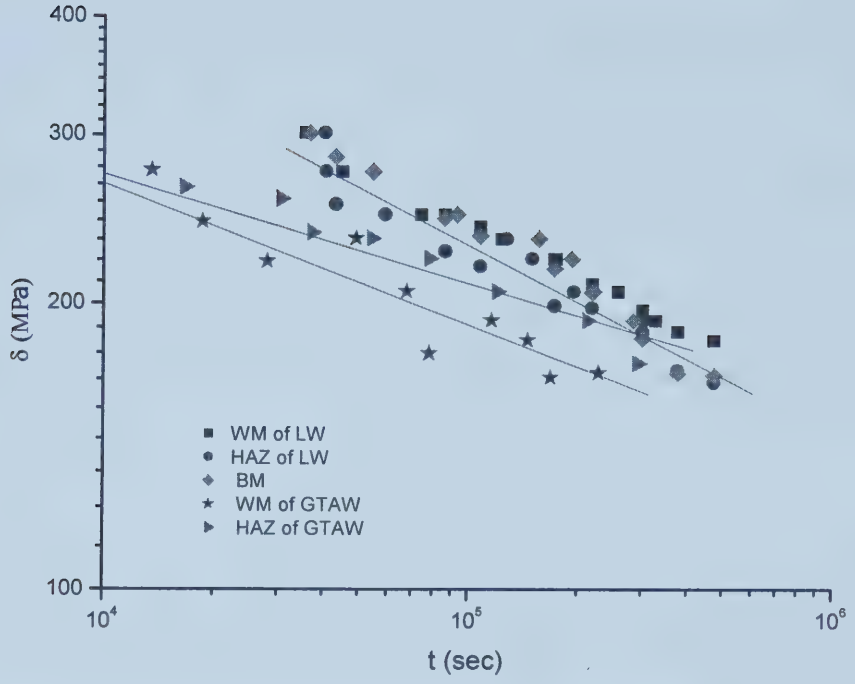

Figure 4-13 Crack initiation lifetime curves

where A and $n(>0)$ are constants depending on material and test conditions as shown in Table 4-1. For the material tested in the present investigation.

Table 4-1 Constants in equation 4-2

	A	n
HAZ of GTAW	5.0×10^{25}	8.86
WM of GTAW	4.2×10^{20}	6.85
LW	8.6×10^{16}	8.91

4.5 SCC propagation kinetics

Once cracks have initiated, they propagate as semi-elliptical cracks or a corner crack until a critical size is reached. Since many cracks initiate successively while existing cracks propagate, it is difficult to determine the growth rate of any individual crack. In order to investigate the crack growth behavior in various zones of welds, the correlation between the maximum surface length of cracks c_{max} and time was determined in Fig.4-14. For each of the curves of c_{max} vs. t, the slope is defined as the surface crack propagation rate, dc/dt.

The data in Fig.4-14 show that for each stress level the curves of c_{max} vs. t can also be fitted by the linear regression method. For LW, the best fitting lines are approximately parallel to each other except for the highest stress of 338MPa, indicating that the crack growth rates are virtually independent of stress level if the applied stress is below the yield strength of the material. The higher crack growth rate at 338MPa may be due to the occurrence of general yield of material, which would confirm that the plastic deformation under the general yielding condition will promote crack growth in corrosive environment[5]. For GTAW, a higher crack growth rate occurs above 276MPa as shown in Fig.4-14(c), which suggests that the WM after GTAW could promote crack propagation. Below 276MPa, the crack growth rates are independent of the stress level, similar to that of LW.

Since the design stress levels of engineering structures are below the yield strength of a material, the surface crack growth rates under the action of applied stresses lower than the yield strength of material are of practical significance. The experimental results listed in table 4-2 indicate that the average values of *dc/dt* in the three zones investigated are comparable, if the error in the crack size measurement is taken into account.

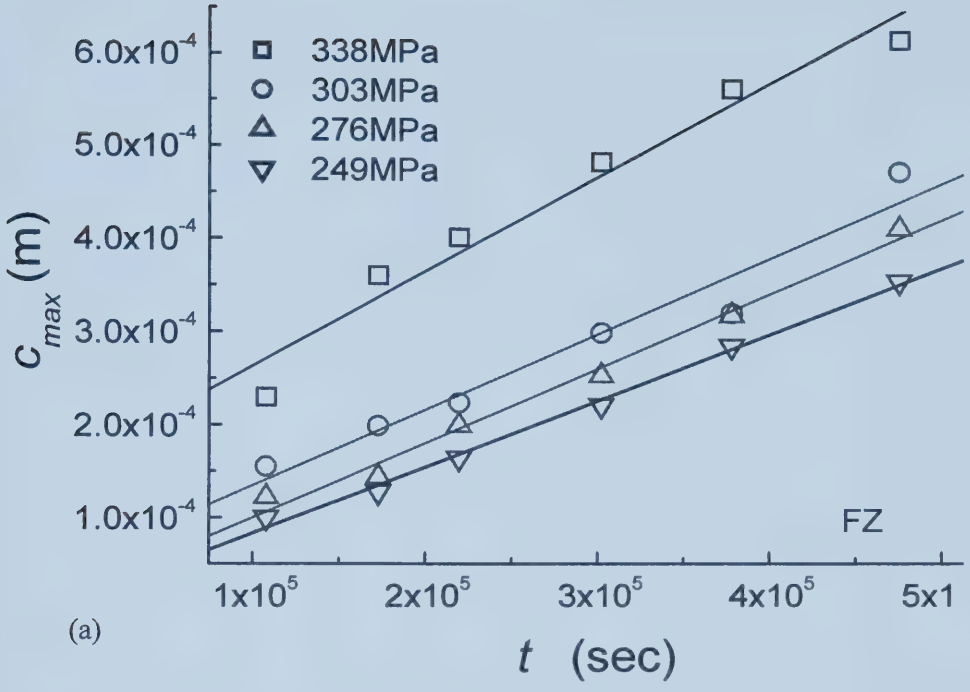
6.0x10-4
5.0x10-4
4.0x10-4
3.0x10-4
2.0x10-4
1.0x10-4
c max (m)
338MPa
303MPa
276MPa
249MPa
FZ
1x10^5
2x10^5
3x10^5
4x10^5
5x1
t (sec)

(a)

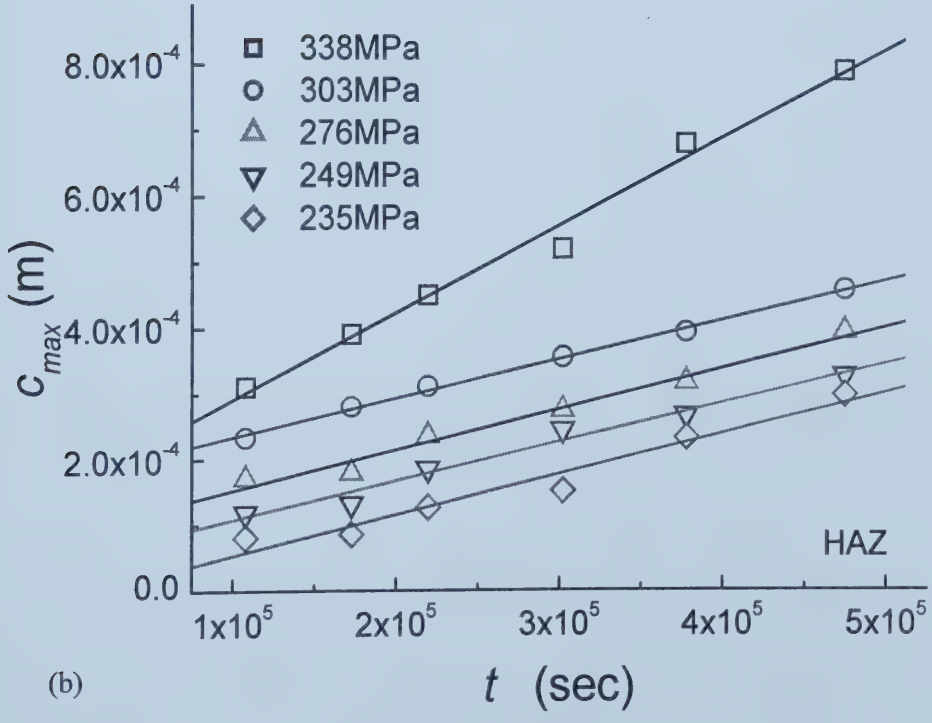
8.0x10-4
6.0x10-4
4.0x10-4
2.0x10-4
0.0
c max (m)
338MPa
303MPa
276MPa
249MPa
235MPa
HAZ
1x10^5
2x10^5
3x10^5
4x10^5
5x10^5
t (sec)

(b)

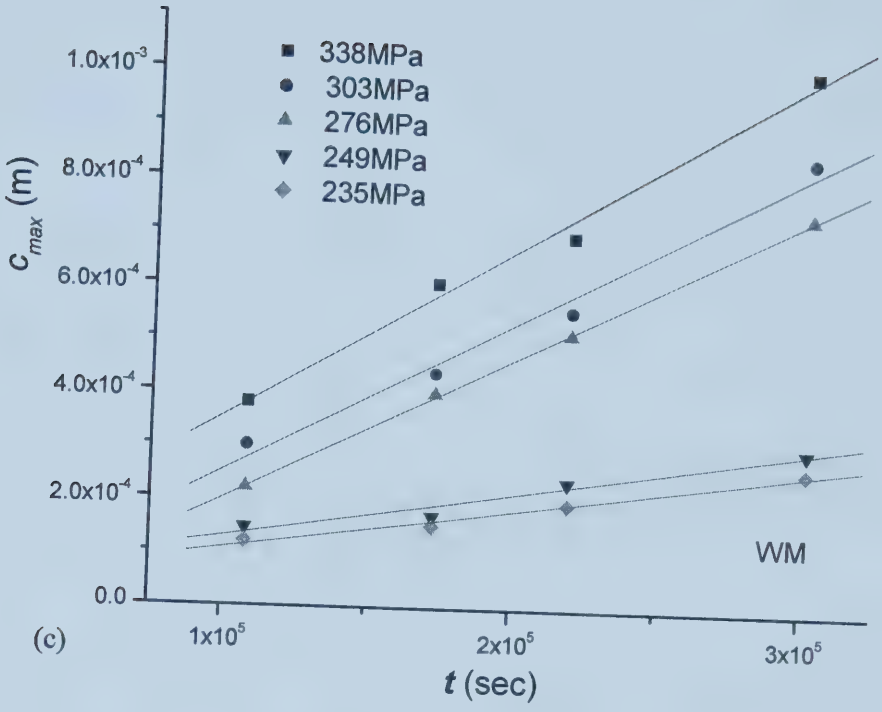
338MPa
303MPa
276MPa
249MPa
235MPa
1.0x10-3
8.0x10-4
6.0x10-4
4.0x10-4
2.0x10-4
0.0
cmax (m)
WM
1x10^5
2x10^5
3x10^5
t (sec)

(c)

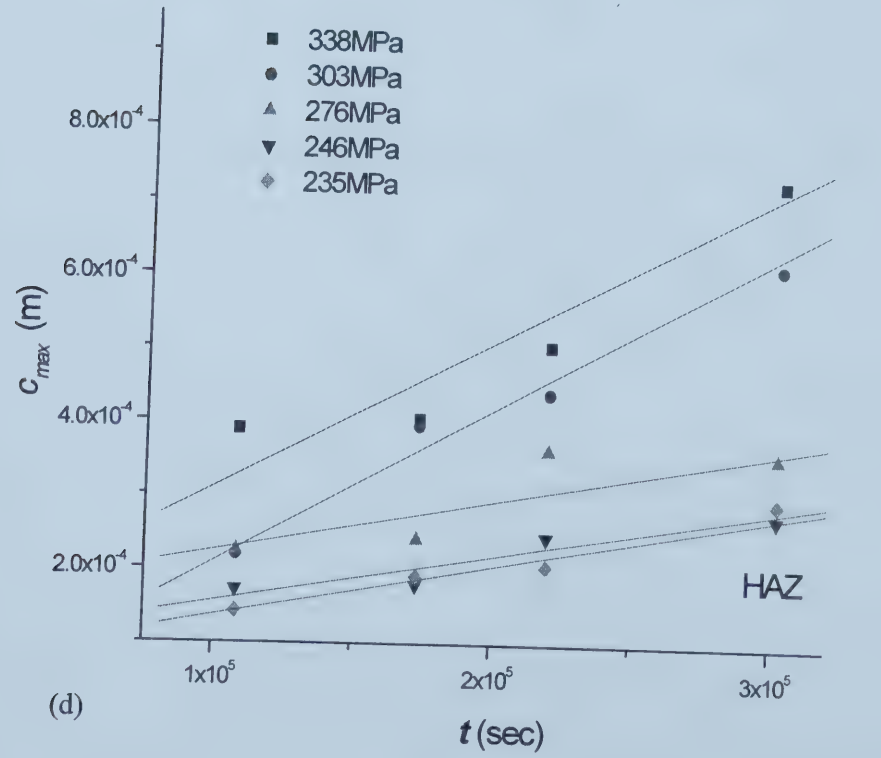
338MPa
303MPa
276MPa
246MPa
235MPa
8.0x10-4
6.0x10-4
4.0x10-4
2.0x10-4
cmax (m)
HAZ
1x10^5
2x10^5
3x10^5
t (sec)

(d)

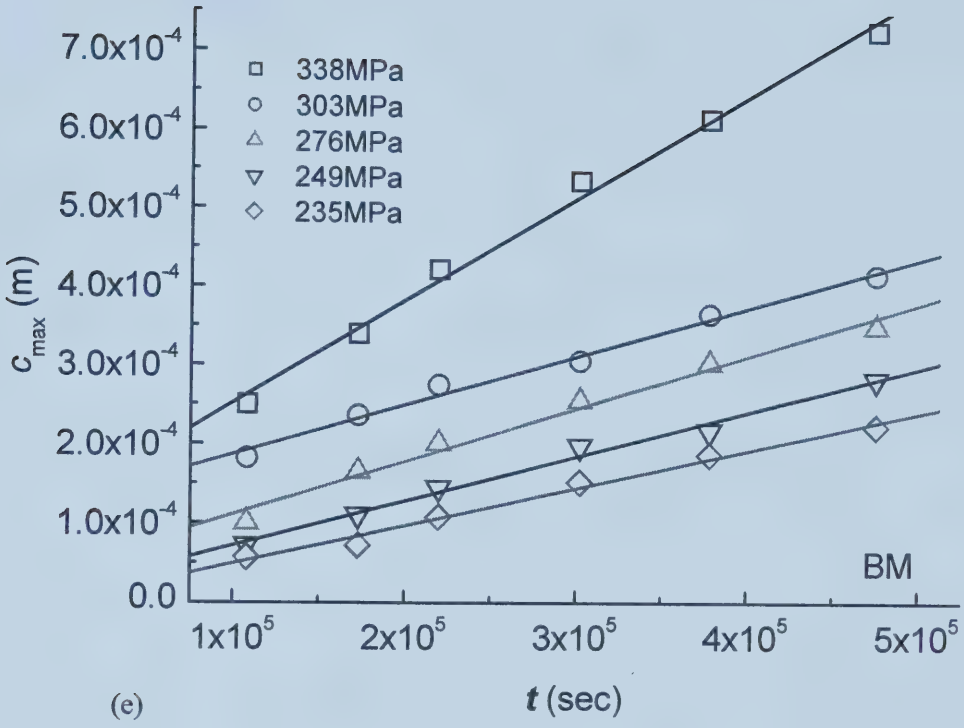

Figure 4-14 Correlation between the maximum surface crack length and test duration (a-b) LW (c-d) GTAW (e) BM

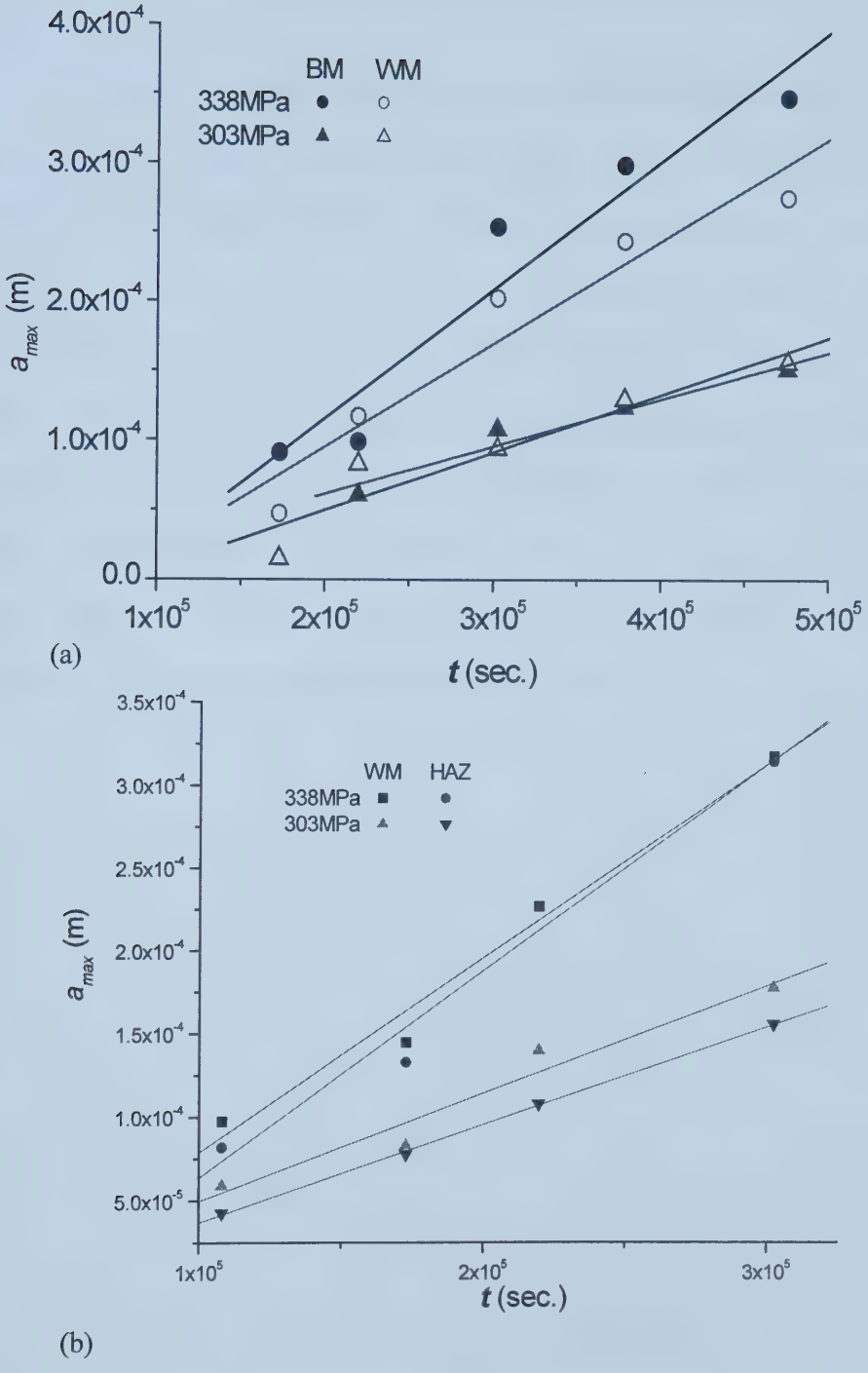

Figure 4-15 Correlation between the crack depth and test duration (a) Maximum crack depth a_{max} in BM and WM after LW (b) Maximum crack depth a_{max} in BM and WM after GTAW

Obviously, the leakage of pipes depends on the crack growth rates in the through thickness direction, *da/dt*, rather than on the surface crack growth rates, *dc/dt*. In order to investigate the crack growth behavior of welds in the thickness direction, the crack depth, *a*, was measured on the cross sections in the longitudinal direction of specimens. Correlations of crack depth a_m versus t are illustrated in Fig.4-15. The values of *da/dt* listed in Table 4-2 were determined from the relationships between maximum crack depth and time in Fig. 4-15. According to the test data of crack depth *a* and surface crack length *c*, the aspect ratios of *a/c* and *da/dt* to *dc/dt* vary according to Table 4-3. These ratios roughly provide a guide to predict the crack growth rate in the through thickness direction, given the surface crack growth rate is available.

Table 4-2 Crack growth rates in different zones

Zone		*dc/dt* ($\times 10^{-10}$m/sec)		*da/dt* ($\times 10^{-10}$m/sec)	
		σ =338MPa	σ=303MPa	σ=338MPa	σ=303MPa
LW	WM	10.2	7.8	7.5	4.2
	HAZ	13.2	5.9	-	-
BM		13.0	5.8	9.4	3.4

Zone		*dc/dt* ($\times 10^{-10}$m/sec)		*da/dt* ($\times 10^{-10}$m/sec)	
		σ =338MPa	σ =303MPa	σ=338MPa	σ= 303MPa
GTAW	WM	32.4	28.8	11.7	6.4
	HAZ	19.9	20.8	12.4	5.8

Table 4-3 Aspect crack growth rate in different zones

	GTAW		LW
	WM	HAZ	WM
$\frac{a}{c}$	0.13~0.23	0.22~0.35	0.1~0.8
$\frac{da/dt}{dc/dt}$	0.2~0.32	0.25~0.57	0.5~0.7

4.6 Discussion

Both SRET and anodic polarization tests show that the WM of GTAW is less resistant to pitting corrosion than the BM, however the WM of LW higher pitting resistance than the BM. It suggests that the WM of GTAW is less corrosion resistance than that of LW.

As for the SCC susceptibility, the WM after two different welding processes exhibits the same behavior as the pitting corrosion. The results of the SCC initiation rates and initiation time obtained after different welding processes have given solid evidence. The SCC initiation rates, dD_C/dt, in the BM and HAZ after LW are the same, but higher than those in the WM, while it is higher in the WM and HAZ than in BM after GTAW. The stress dependence of SCC initiation rates can be empirically expressed as $\frac{dD_C}{dt} = \alpha\sigma^{\beta}$. At the same stress levels, the crack initiation time for both WM and HAZ after GTAW is higher than those after LW. The SCC initiation time of material tested increases with decreasing applied stress and the correlation between the SCC initiation time t_i and the applied stress σ can be formulated as $t_i = A\sigma^{-n}$. The different microstructures in various zones of LW 304 stainless steel are of little influence on the SCC initiation and propagation kinetics, whereas the changes in microstructure after GTAW have significant influence on the SCC initiation and propagation. In addition, the SCC propagation rates of the materials tested are independent of the applied stress, if the applied stress is below the yield strength of the material. Stress corrosion propagation rates increase under conditions of general yielding. For GTAW, due to its corrosion-susceptible microstructure in WM and the presence of residual stress, the WM has higher SCC propagation rates even below the general yielding strength.

The WM after LW has decreased corrosion susceptibility, which suggests that the effect of such alteration is to suppress crack initiation and thereby lower the average number of cracks in a given propagation front. The consequence of this will be less coalescence and therefore less tearing in the fracture process. For chemical reasons, it can be speculated that these changes decreasing susceptibility may reduce the transient

currents by increasing the repassivation kinetics, which, if it occurs, will also reduce the crack velocity. In turn, the absence of shearing, or reduction in the propagation by shearing, means that since a given crack front is less aided by the mechanical component it must depend most upon the chemical component of fracture. In contrast, the WM after GTAW has increased susceptibility. It gives rise to promoting crack initiation and increasing the average number of cracks. The shearing of the intermediate ligaments to fracture can be expected to produce quite large anodic dissolution rates, as originally hypothesized by Hoar and Hines[6]. This process is ancillary to the cracking process, while, in the more resistant structure of LW specimen, it is suppressed. These steels could be expected to develop lower anodic currents during cracking. As a result, it is observed that both crack velocity on the surface and in the thickness direction is lower than after GTAW.

All above indicate that the resistance of 304 stainless steel investigated to the SCC initiation has a good correlation with its pitting resistance. The material with higher pitting resistance will be more resistant to SCC. SCC is likely to initiate from pitting process. Pits can act as a stress concentrator and an occluded cell offering the local environment for the SCC initiation. The other likelihood is that the tensile stress acts as a role to open the crack and rupture the protective film at an emerging slip band. Then cracks grow by anodic dissolution of the bare metal surface at the rupture site. In this case, the repassivation kinetics of the exposed fresh surface, which relies on the stability of the passive film, still determines the crack propagation. In each case, the stability of passive films could play an essential role in initiation and propagation of SCC. Further study on the properties of passive films could discover the underlying mechanism.

The cracking mechanism of SCC in the HAZ after LW is the same as that in the BM, i.e., the cracks initiate and propagate initially in the transgranular mode and, as the crack size reaches a critical value, the cracking propagation changes into an intergranular mode. For GTAW, a mixed trans- and inter-granular mode as observed in HAZ.

4.7 Summary

Generally, the WM after GTAW shows a lower corrosion resistance than the WM after LW to both pitting corrosion and SCC. The microstructure alteration and residual stress induced after welding processes could account for the difference. As pitting corrosion and SCC are related to the break-down of the passive film, the revelation of the relationship among the microstructure, residual stress and passive films would be helpful to understand the influence of welding processes.

References

1 Shaikh, H., Khatak, H. S., Seshadri, S. K, Gnanamoorthy, J. B., and Rodriguez, P., Effect of Ferrite Transformation on the Tensile and Stress Corrosion Properties of Type 316 L Stainless Steel Weld Metal Thermally Aged at 873 K, Metallurgical and Materials Transactions A, Vol.26A(7), 1995, p1859

2 Krishnan, K. N. and Rao, K. P., Effect of Microstructure on Stress Corrosion Cracking Behaviour of Austenitic Stainless Steel Weld Metals, Materials Science and Engineering, A, Vol. A142, 1991, p79

3 Raghunatha, R. B., Prasad, R., K. and Iyer, K. J. L., Effect of Chemical Composition and Ferrite Content on Room Temperature SCC Behavior of Austenitic Weld Metals, Corrosion, Vol.49(3), 1993, p248

4 Shibata, T., Zhang, S. and Haruna, T., Statistical Approach for Evaluating SCC Initiation and Propagation Behavior of Sensitized Type 304 Stainless Steel, Journal-De-Physique, Vol.10(6), 2000, Pr6-185 - Pr6-190

5 Y. Watanabe and T. Kondo: Corrosion 2000, Vol.56(12), 2000, p1250

6 T.P. Hoar and J.G. Hines, J. Iron Steel Inst., Vol. 124, 1956, p182

Chapter 5 Mechanism Analysis

5.1 Microstructure analysis

Based on the result from the *in-situ* SRET and anodic polarization tests, the weld metals of LW and GTAW specimens seems to have a great difference in corrosion resistance, although both have the same nominal composition. The microstructures in Fig. 5-1 show a significant difference in the contents, morphology and distribution of δ-ferrites in the WMs obtained after the two different welding processes. There is much more δ-ferrite formed in the WM of laser-welded specimen than that of GTAW specimen. The content of δ-ferrite in WM of laser-welded specimens is 44.5% while, in GTAW specimens, only 11.4% δ-ferrite is found.

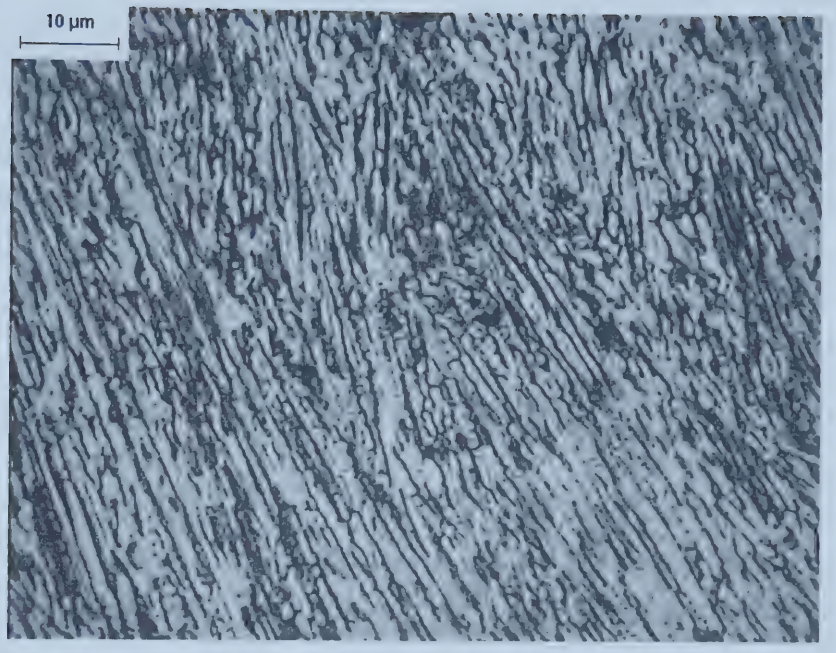

(a)

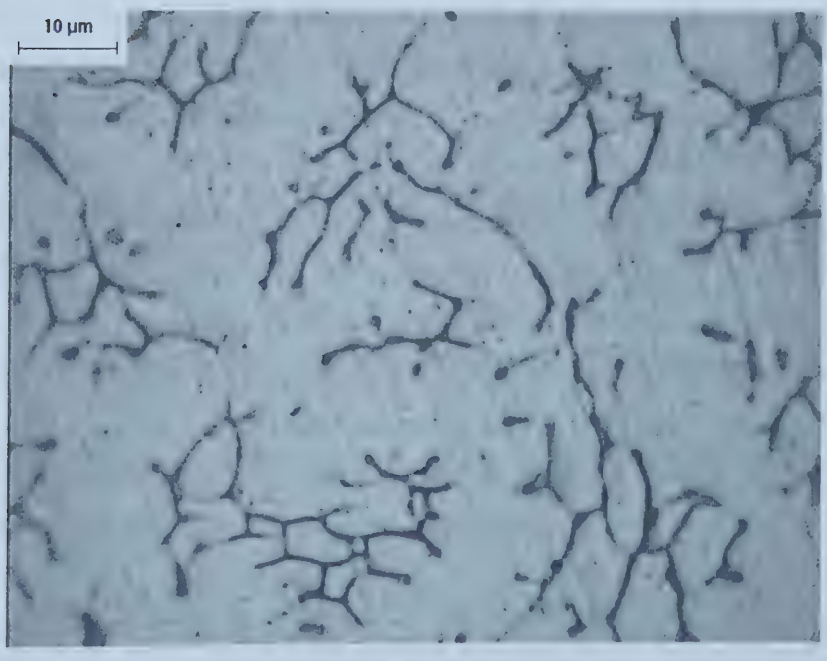

(b)

Figure 5-1 (a) The morphology and distribution of delta-ferrite in the WM after LW (b) The morphology and distribution of delta-ferrite in the WM after GTAW

The δ-ferrite content in 300 series of austenitic stainless steels under the pseudo-equilibrium condition can be estimated from the equivalent contents of Cr and Ni, which can be calculated from the composition of material using the following equations,

$$Cr_{eqv}=Cr+Mo+0.7Nb \quad (5\text{-}1)$$

$$Ni_{eqv}= Ni+35C+20N+0.25Cu \quad (5\text{-}2)$$

Substituting the values of element contents of 304SS into Eqs. (1) and (2), the equivalent contents of 18.9% and 10.7% for Cr and Ni, respectively, In line with the WRC-1992 diagram shown in Fig. 5-2[1], the ferrite content in the weld metal of 304SS under the pseudo-equilibrium condition is virtually 11.5%. This value is very close to the δ-ferrite content experimentally determined in the WM of GTAW specimens. However, the δ-ferrite content in the WM of laser welded specimen deviates greatly from the estimated value. The discrepancy is attributed to the difference in the cooling rates resulting from the difference in the heat-input of these two fusion runs. The heat-input for GTAW is about 0.2 kJ/mm, which is much higher than that of 0.04kJ/mm for LW. Upon solidification, the primary delta-ferrite (δ_p) forms in the liquid metal. During cooling process after the solidification, $\delta \rightarrow \gamma$ transformation takes place. Because of small fusion zone size and low heating input the cooling rate in LW process is much higher than that during GATW. The fast cooling during laser welding process does not offer sufficient time for a complete $\delta \rightarrow \gamma$ transformation. As a result after LW, a large portion of primary δ-ferrite remained and the incomplete transformation results in the retention of ''skeletal'' dentritic δ_p within the primary austenite.

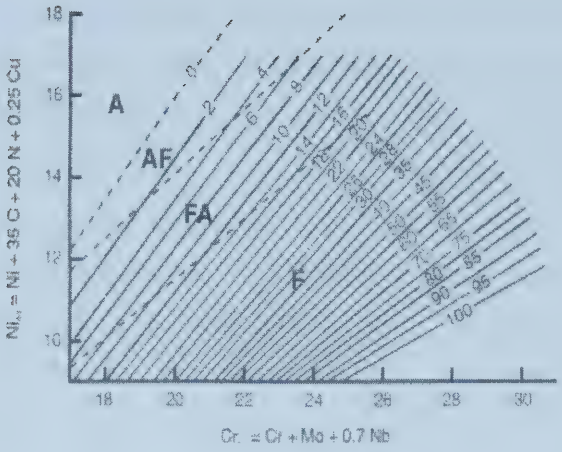

Figure 5-2 WRC-1992 Constitution diagram
for stainless steel weld metal

Considered as the favorable sites for pit initiation in austenitic stainless steel are δ-ferrite [2], the locations around inclusions such as sulfides [3], and the depleted zones of chromium and molybdenum around the precipitated carbides, sigma or chi phases [4]. The sensitization may be caused by the formation of a Cr-depleted zone resulting from the precipitation of $M_{23}C_6$ in the intergranular region during the post-welding cooling process. It is considered as one of the primary factors causing the intergranular corrosion. In the present investigation, the carbon content of the test material at 0.038% is very close to the low carbon grade. Therefore, only a very small amount of $M_{23}C_6$ precipitation, if cooling rate is relatively low, can form during the welding process [5,6]. Since the cooling rate in the laser welding process is much higher than that in the GTAW process, the precipitation of $M_{23}C_6$, if occurs, is likely to be found in the GTAW specimen. This may be one factor contributing to the corrosion resistance degradation of GTAW specimens.

The experimental evidence showed that, when present in a small amount of δ-ferrite, chromium and other ferrite-stabilizing elements enriched the δ-ferrite while nickel and austenite-stabilizing elements enriched the austenitic matrix, resulting in a poor pitting resistance [7]. Pujar et al [8] used the induction time of passive film breakdown as a parameter to represent the pitting resistance of materials; they found that the induction

time was heavily dependent on the δ-ferrite content in microstructure and the heat-inputs of welding processes. As the heat-input increased, the induction time decreased rapidly. This was attributed to the fact that the higher heat-input would result in coarser δ-ferrite grains and that the passive film on surface of coarse-grained δ-ferrite possesses low stability [8]. It should be noted that the above conclusion is valid when only a small amount of δ-ferrite exists in the austenitic matrix. When ferrite grains are present in significant quantities (as observed in duplex stainless steels), it could markedly improve the resistance to pitting corrosion [9].

5.2 The effect of the welding process on the conductivity of passive films

As shown in Fig. 5-3, the potentiodynamic scans were conducted in order to reveal the voltammetric behavior of the passive films during capacitance measurements. It shows that the current densities remain nearly zero in a wide potential range. This finding indicates that the passive film has capacitance characteristics with a negligible Faraday current. The current then becomes cathodic, arising either from film reduction or from hydrogen evolution. The capacitance measurements were performed within the potential range of about zero current so as to eliminate the Faradic processes associated with both cathodic discharge and anodic transpassive oxidization of the passive films.

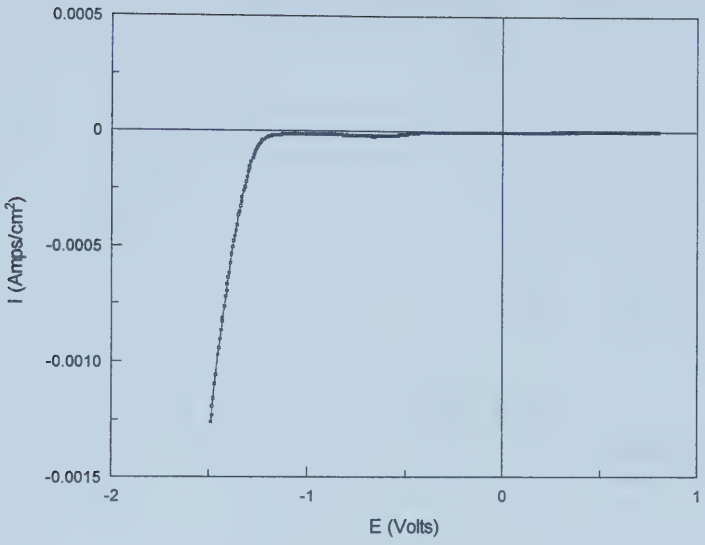

Figure 5-3 Potentiodynamic scan in cathodic direction with a rate of 50 mV s^{-1} after pre-passivated for 2 hours at 0.5 V (vs. SCE) in the borate solution of pH 9.2

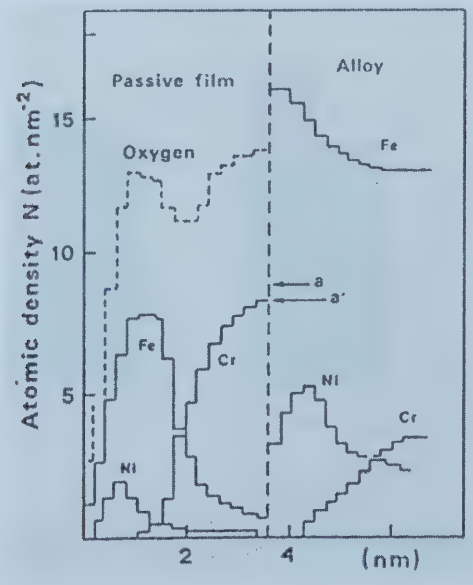

Figure 5-4 Depth composition profiles obtained by AES for the passive films formed on 304 stainless steel at 0.8 V vs. SCE [11]

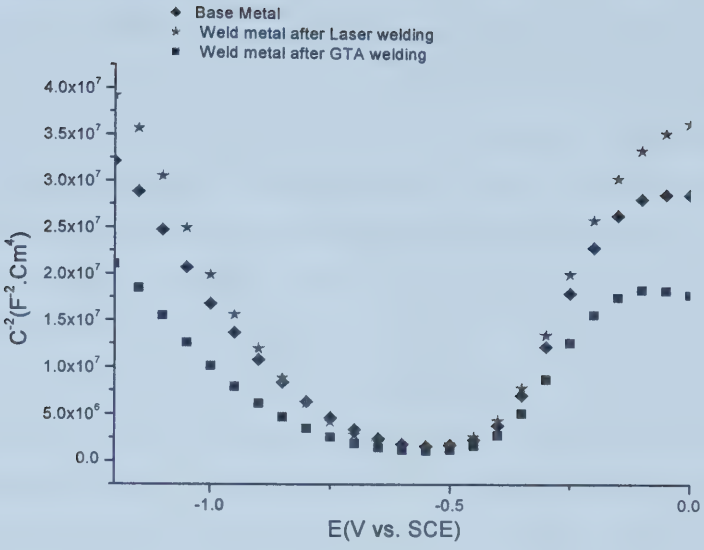

(a)

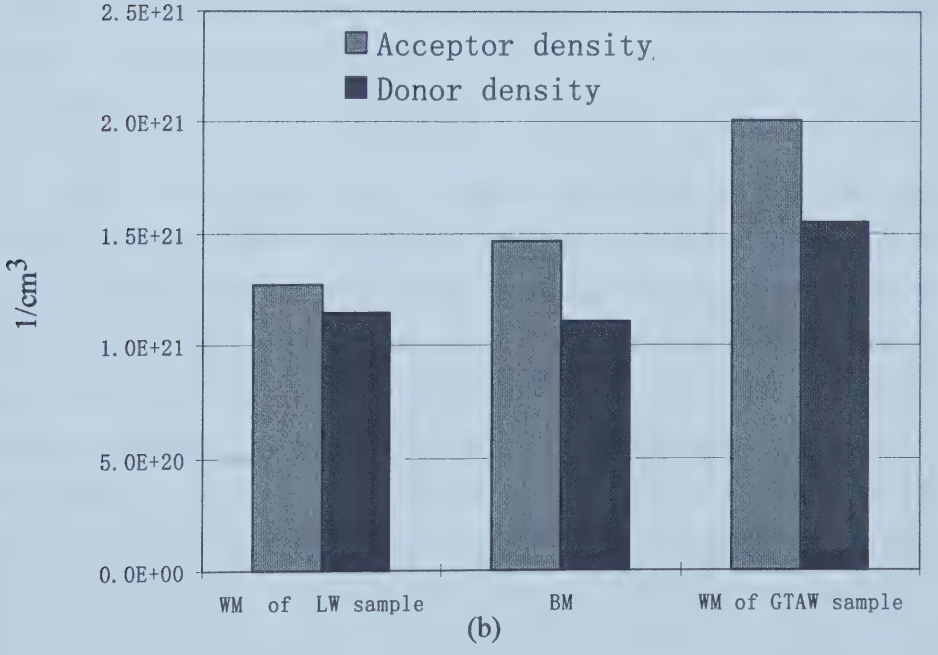

(b)

Figure 5-5 (a) The Mott–Schottky type plots in a borate solution of pH 9.2
(b) Comparison of doping densities in different zones

Mott–Schottky plots in Fig. 5-5 (a) reveals two linear zones [10]. One of them is in the cathodic region (E<-500 mV vs. SCE) and the other is in the anodic region (E>-500 mV vs. SCE). This behavior was modeled by a bi-layer structure of the passive film as shown in Fig. 5-4, which depicts the Auger depth profiles obtained by applying the sequential layer puttering model[11]. The passive film, formed on the 304 stainless steel in a borate buffer solution, has a duplex character with an inner region rich in chromium oxide and an outer region rich in iron oxide. The linear zone in the cathodic region is the capacitance response for a p-type semiconductor and it is related to the inner layer that comprises mainly the chromium oxides[12]. The linear zone in the anodic region is the capacitance response for an n-type semiconductor and it is used to characterize the outer layer that is composed mainly of iron hydroxides[12]. The concentrations of acceptors and donors in passive films can be calculated from the negative and positive slopes, respectively with Eqs. 2-3, 2-4, and the results are plotted in Figure 5-5 (b). The concentrations of the current carriers in the passive films increase with decreasing slopes of Mott-Schottky plots. Higher concentrations of the current carriers indicate the existence of more defects in the passive film and it results in a lower stability of the passive film [13].

Figure 5-5(b) clearly shows that the concentrations of both the donors and acceptors in the weld metal of GTAW specimens are higher than those in the BM, indicating that the WM has lower pitting resistance. This observation agrees with the results of SRET and potentiodynamic tests. The stability of a passive film depends mainly on the properties of the inner layer that comprises dense chromium oxides. The data also indicate that the WM of laser-welded specimens has lower acceptor concentration in the passive film than the base metal does. The observed difference explains why the WM of LW specimens is more resistant to pitting corrosion than that of GTAW specimens.

5.3 Effect of tensile stress on stability of the passive film

Effect of tensile stress on the Mott–Schottky plots (measured from the WM of GTAW samples) is depicted in Figure 5-6 (a). As summarized in Figure 5-6 (b), the

concentrations of both acceptors and donors in the passive film of the WM increase remarkably with tensile stress. This fact indicates that the stability of the passive film of the WM in GTAW is reduced when the tensile stress is present and it will give rise to an increase in localized corrosion susceptibility of the material. It is expected that the localized corrosion is more likely to initiate at the zone where tensile residual stress exists because the passive film is heavily doped.

In contrast with the sharply increased donor and acceptor densities of the passive film in the WM when increasing tensile stress, the donor and acceptor densities for the base metal is almost independent of tensile stress, even in the case when the applied stress is as high as 100% of the yield strength, as shown in Figure 5-7. A possible explanation for such a difference in the stress-response of the passive films could be related to the residual stresses and difference in microstructure produced during the welding processes. The residual stress distribution in welded zone has been well recognized[14]. For the longitudinal welded specimen, the residual stress exists in the WM is tensile and the surrounding is compressive. Therefore, when the tensile stress is applied, the actual stress level at the WM will be higher than that at the BM. In addition, the gain size in the WM is larger than that in the BM, resulting in lower yielding strength of the WM. Residual stresses at the specimen surface comprise the residual stresses due to the welding process and those produced during preparation at the test surface. Because the test surface is located in the middle part of the tensile specimen, where the tensile residual stress exists in the weld metal, it makes the actual localized stress well above the applied stress. According to the point defect model [15], more defects will be produced when the tensile stress level is higher. In addition, the WM has a lower yield strength resulting from its larger grain size and it will be more significant in the GTAW specimens because of the higher heat-input and lower cooling rate. So the plastic deformation is more likely to occur in the WM under the same stress level. The passive film will breakdown because the slip of dislocations will make the material more sensitive to the localized corrosion.

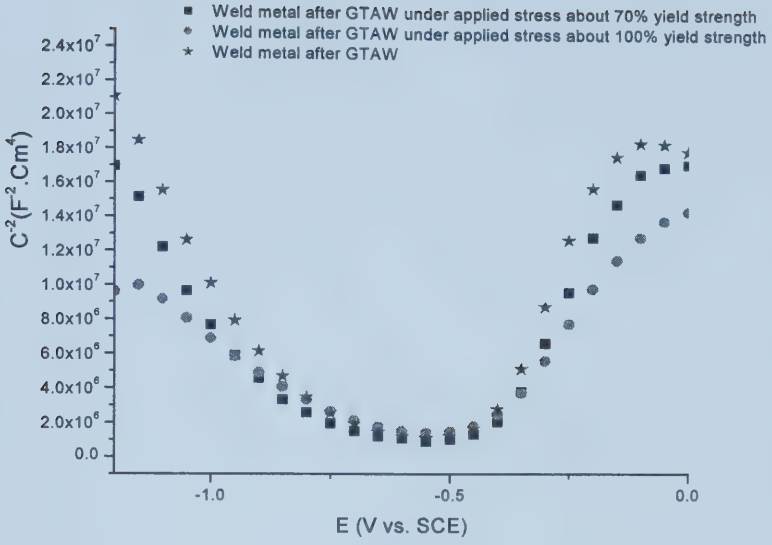

(a)

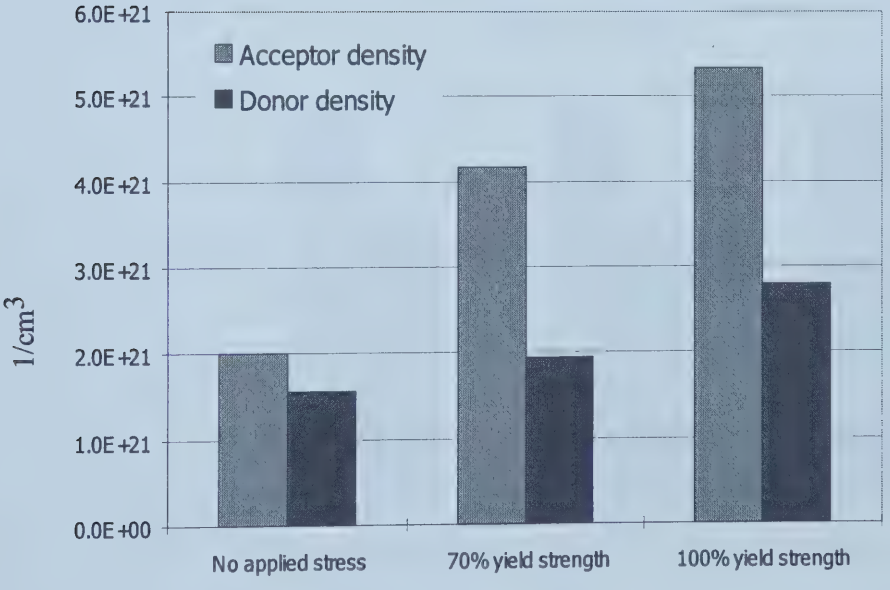

(b)

Figure 5-6 (a) The Mott–Schottky type plots of WM of GTAW specimens in a borate solution of pH 9.2 (b) Comparison of doping densities (Various stress levels in the WM)

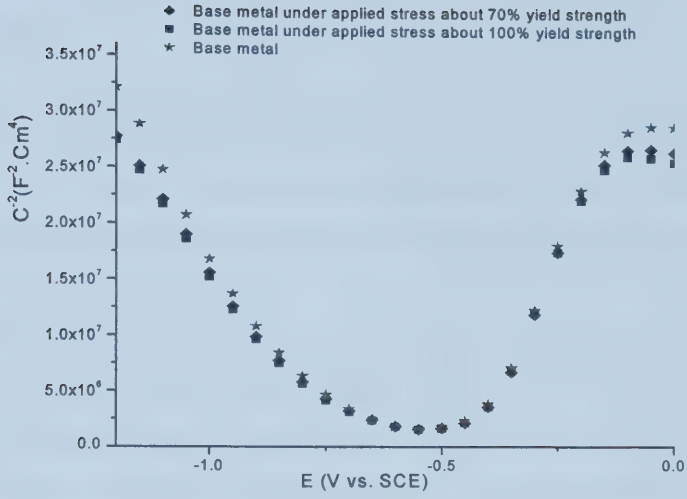

(a)

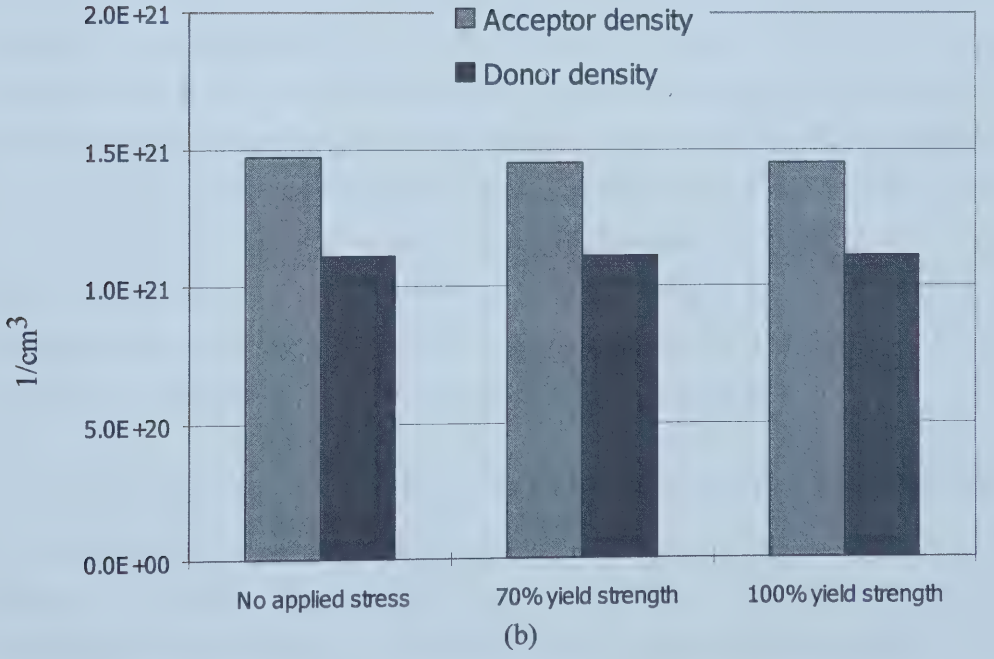

(b)

Fig 5-7 (a) The Mott–Schottky type plots of the BM in the borate solution of pH 9.2
(b) Comparison of doping densities (Various stress levels in the BM)

5.4 Relationship between properties of passive film and resistance to SCC and pitting corrosion

All above indicates that the properties of the passive film of welded 304 stainless steel have a good correlation with its pitting resistance. The WM after GTAW with higher donor and acceptor densities will be less resistant to pitting corrosion.

Similarly, the stability of the passive film could also account for the initiation of SCC. When applied stress is imposed, the passive film in the WM after GTAW seems more sensitive to these changes, compared to the WM after LW. The donor and acceptor densities are observed to increase with the applied stress, when it reaches a critical value. In the SCC behavior of the WM after GTAW, it exhibits higher initiation and propagation rates than the BM below the general yielding strength. Considering the great increase in the donor and acceptor densities in the WM after GTAW, the fast crack propagation rate is supposed to be closely related to this change in the passive film. As mentioned before, an external applied stress imposes an actual stress well above the general yielding stress in the weld metal. Because of the WM after GTAW possessing a less stable passive film under an applied stress, the break down of passive films could be more favorable, and the crack could initiate and propagate with ease. However, when increasing the stress level below general yielding strength, the SCC initiation and propagation rates have shown negligible variation in the WM after LW. SCC behavior appears to be independent of the stress levels below yielding stress in this case.

The reason may lie in the different microstructure formed after LW and GTAW. It is reasonably inferred that poor pitting corrosion and SCC resistance of WM in GTAW specimens is related to the higher heat-input and lower cooling rate because the Cr-depleted zone is more likely to form in the GTAW process, and large grain size could reduce the yield strength. LW induces a microstructure of better corrosion resistance. At the same stress levels below yielding strength, the WM after LW maintains a SCC resistance better than the BM. It is suggested that a susceptible microstructure seems to play a far more important role than the applied stress in SCC initiation and propagation

for this material, though it is worthy of further work. As a result, whether it is pitting corrosion or SCC, the initiation and propagation of localized corrosion could take advantage of the susceptibility of the WM after GTAW, which becomes noticeable if there exists an applied stress or polarization potential.

Overall, the microstructure affects the passive film and finally the SCC behavior. Regarding the relationship of microstructure and the passive film, the changes in the microstructure of various zones of LW 304 stainless steel have little effect on the SCC initiation and propagation kinetics, whereas the changes in microstructure after GTAW have significant influence on the SCC initiation and propagation. These distinctions between LW and GTAW may be largely attributed to the combined effect of the noteworthy difference in the stability of passive film formed on the surface and the residual stresses after two dissimilar welding processes. With respect to the stability of passive film discussed before, a quite stable passive film is formed on the surface of the WM after LW, which is more stable than the BM. However after GTAW, the stability of the passive film in the WM is worse than the BM. Therefore, under the same environment, the WM after GTAW exhibits susceptibility to corrosion. It promotes the initiation and propagation of localized corrosion, such as pitting and SCC.

5.4 Summary

The δ-ferrite content in WM of GTAW specimens is 11.4% while that of LW specimens is about 44.1%. This difference in microstructure is produced by different cooling rates after these two welding processes. With regard to the microstructure difference, it indicates that the WM with a small amount of δ-ferrite in microstructure is more susceptible to pitting corrosion than the WM with a duplex microstructure. Mott-Schottky analysis has demonstrated that the pitting resistance of welded 304SS in different zones is mainly related to the concentration of acceptor concentration in the passive film. A high concentration of acceptors and donors results in low pitting resistance. When a tensile stress is applied, it tends to reduce the stability of the passive film and degrades the localized corrosion resistance in the WM after GTAW, but has little influence on BM.

References

1 Erich Folkhard, Welding metallurgy of stainless steel, 1988, p199

2 H.J. Dundas and A.P. Bond, "Effects of Delta Ferrite and Nitrogen Contents on the Resistance of Austenitic Stainless Steels to Pitting Corrosion," paper presented at NACE Corrosion/75, Preprint No.159, 1975

3 A.J.Sedriks, International Metals Reviews, Vol.28(5), 1983, p295

4 A.J.Sedriks, International Metals Reviews, Vol.27(6), 1982, p321

5 B. Weiss and R. Stickler, Metallurgical Transactions, Vol.3, 1972, p851

6 Erich Folkhard, Welding metallurgy of stainless steel, 1988, p104

7 A. John Sedriks, Corrosion of Stainless steels, 1996, p131

8 M.G. Pujar, R.k. Dayal, T.p.S.Gill, S.N. Malhotra, Role of delta-ferrite in the dissolution of passive films on the austenitic stainless steel weld metals. Journal of Materials Science Letters, Vol.18, 1999, p823

9 A. John Sedriks, Corrosion of Stainless steels, 1996, p16

10 N.E. Hakiki, S. Boudin, B. Rondot and M. DaCunha Belo Corros. Sci., Vol.37, 1995, p1809

11 G. Lorang, J.L. Xu, J.P. Langeron, Surf. Interface Anal., Vol.19, 1992, p60

12 F. Gaben, R. Oltra, B. Vuillemin, V. Vignal, B. Baroux, J.C. Joud, in: M.B. Ives, J.L. Luo, J. Rodda (Eds.), Proceedings of the 8th International Symposium on the Passivity of Metals and Semiconductors, PV 99-42, The Electrochemical Society Proceedings Series, Pennington, NJ, 2000, p621

13 H. Bohni, P. Schmuki, J. Electrochem. Soc., p1908, 1992, Vol.139

14 Storesund, J. and Tu, S.-T., Geometrical effects on creep in cross-weld specimens, Int. J. Pres. Ves. & Piping, Vol. 62, 1995, p179

15 D.D. MacDonald, J. Electrochem. Soc., Vol.137 , 1990, p2395

Chapter 6 Summaries and Recommendations

6.1 Main conclusions

In this thesis, the pitting corrosion and SCC behavior of longitudinally welded 304 stainless steel and the effects of microstructure changes and residual stresses induced by two different welding processes, namely, the LW and the GTAW, were experimentally investigated.

The pitting resistance of materials was evaluated with anodic polarization measurements and the pitting activity of the material was monitored *in situ* with the SRET to understand the influence of the microstructure changes induced by the welding processes. The difference in the pitting resistance due to the influence of microstructure changes and the residual stresses was related to the concentrations of donors and acceptors in the passive films on the weldments.

The crack initiation times and the crack propagation rates of welded 304 stainless steels during SCC were experimentally measured and the microstructural effect on the both SCC kinetics and mechanism was investigated. The empirical expressions were proposed to formulate the correlations between the crack initiation time/the crack initiation rate and applied stress. Also an attempt was made to find the relationship between the resistance of materials to pitting corrosion and chloride SCC.

The following conclusions are drawn from the present work:

1) The δ-ferrite in microstructure possesses an important influence on the resistance of welded 304 austenitic stainless steel to pitting corrosion and chloride SCC. The effect of δ-ferrite depends on its amount, composition and morphology, which are controlled by the welding processes. The weld metal with a duplex γ+δ structure formed during rapid cooling process, like that of LW specimen, displays a good

resistance to both pitting corrosion and chloride SCC, however the weld metal with the structure of dendrite austenite and a small amount of grain boundary δ phase formed in the slow cooling process, such as that obtained after GTAW process, has high susceptibility to both pitting and chloride SCC.

2) The resistance of welded 304 stainless steel to the chloride SCC initiation is closely related to its pitting susceptibility. The material with low pitting susceptibility is more resistant to chloride SCC.

3) The influence of microstructure on the pitting corrosion resistance and chloride SCC of welded 304 stainless steel is related to the concentration of donors and acceptors in the passive film. The material with lower acceptor and donor concentration in the passive film possesses higher corrosion resistance.

6.2 Recommendations for future work

1) In industrial practice, welding processes that could induce a duplex γ+δ structure in the weld metal of 304 stainless steels are helpful for reducing the likelihood of pitting corrosion and chloride SCC.

2) The content of ferrite in the austenite matrix appears to play a major role in determining the corrosion resistance. Evident improvement in corrosion resistance was found with a large increase in ferrite. Attempts should be made to find quantitative relationship between the proportion of ferrite and corrosion resistance.

3) Although tensile stress has a negative influence on the stability of passive films, quantitative measurement of residual stress will yield more useful information concerning the relationship between the stability of a passive film and actual stress.

4) SRET proved to be an effective method to monitor the initiation and propagation of pitting. However, it is not so effective in detecting the occurrence of SCC. Advanced methods such as electrochemical noise technique (ENT) could be sensitive enough to detect any current or voltage fluctuations generated during localized corrosion. Efforts need to be made to distinguish the characteristic signals between pitting and crack initiation.

5) As the velocity at which cracks propagate in the through thickness direction largely determines the lifetime of the material, it would be constructive if a method could be developed to detect and monitor crack propagation in this direction.

University of Alberta Library
0 1620 1799 3195
B45841